PhD Dissertation

International Doctorate School in Information and Communication Technologies

DISI - University of Trento

Anti-Stiction And Self-Recovery Active Mechanisms For High Reliability RF-MEMS Switches

Alena Repchankova

Advisor:

Prof. Gian-Franco Dalla Betta

Università degli Studi di Trento

Co-Advisor:

Dr. Jacopo Iannacci

Fondazione Bruno Kessler

April 2010

Abstract

Reliability of RF-MEMS devices is one of the main concerns of the engineers and scientists dealing with such type of devices. In particular, there are plenty of studies and investigations devoted to protection of devices from different kind of failures related to their operating conditions. The adhesion of movable parts of switches onto the actuation electrode, also referred to as stiction, due to accumulated charge or to micro-welding phenomenon, are the most common types of RF-MEMS failures. This work presents a novel effective heat-based mechanism that enables to release a stuck component. Such mechanism can be embedded within the switches of any topology and it has no influence on the normal behavior of the device.

Keywords

RF-MEMS switch, reliability, stiction, microwelding, self-recovery mechanism

Contents

List of Tables

List of Figures

Chapter 1

Introduction

In last years, RF-MEMS (Radio Frequency MicroElectroMechnical Systems) have proved to enhance the reconfigurability as well as the performance of transceiver architectures for wireless applications. Indeed, using MEMS lumped components (e.g., variable capacitors, inductors and switches) within RF circuits enables a significant hardware redundancy reduction, while assuring the possibility of retargeting the same architecture to the requirements of different communication standards. RF-MEMS are essentially based on movable micro structures (e.g., suspended membranes and cantilevers), whose position changes on the basis of an externally applied signal. Since RF-MEMS devices involve three different physical domains (i.e., electrical, mechanical and electromagnetic), the models describing their behavior take into account the joint effect of different phenomena.

Recently, researchers have deeply studied different aspects related to operation of RF micro-switches. Some activities were concentrated on the optimization of device structure and materials for specific applications; others were instead focused on the characterization of RF-MEMS behavior in a certain physical domain. In spite of such research efforts, the reliability problems of RF-MEMS have been analyzed and addressed only partially.

On the other hand, reliability and robustness are essential requirements for the widespread employment of RF-MEMS devices in different contexts, ranging from automotive applications to space communications. This is essentially the main motivation underlying the proposed research.

The reliability of electronic devices is a crucial issue in every field of Information and Communication Technologies (ICT) because it may affect the correct operation of any kind of system. In general, reliability is an inter-disciplinary subject which involves multiple domains such as physics, electronics and statistics. The ever increasing complexity of electronic equipment makes the reliability issue more and more difficult to tackle. Typically the reliability of systems based on multiple electronic components is assessed through several empirical rules, developed on the basis of large sets of experimental data. One of the most famous standards of this type is the *Handbook for the Reliability Prediction of Electronic Equipment* released in late 1986 by the US Department of Defense and still active, after multiple integrations and revisions. Standard reliability tests were also developed for well established technologies (e.g. CMOS) and usually include such procedures like long-term tests and accelerated tests. Differently, in the MEMS/RF-MEMS field there are no such well designed sets of rules and standards in determining their reliability. This lack is due, on one side, to the fact that the field of RF-MEMS is rather novel and not completely developed yet. On the other hand, MEMS devices, for their multi-physical nature, lead to a wider concept of reliability including both electric and mechanical parameters. In this context, the research activity described in this thesis aims at developing a mechanism which improves the reliability of RF-MEMS switches and that is applicable to large part of device topologies.

1.1 Stiction Failure of RF-MEMS Switches

One of the most serious reliability problems for RF-MEMS switches is the ***stiction***. This term refers to adhesion phenomena of a movable electrode with respect of the fixed one. The mechanism which leads the devices into stiction can be manifold and generally depends on the switch morphology.

Usually, all devices belonging to the family of RF-MEMS switches can be gathered in two large groups: ***capacitive*** and ***ohmic (resistive)***. The presence of a dielectric layer separating the electrodes from one another during their contact is a common characteristic of RF-MEMS switches. The process of electrostatic polarization of the dielectric layer starts immediately at the moment of the device biasing. The amount of accumulated charge is mostly influenced by several factors like the time of device actuation, the applied bias and the environmental temperature. Therefore, the longer the device is operated, the more significant the amount of charge accumulated in the dielectric layer becomes. The failure of an RF-MEMS device due to stiction happens when the movable electrode does not go back to its rest position when the bias is removed, due to the electrostatic attractive force generated by the accumulated electric charge. In fact, the release time of the stuck movable part depends on the amount of accumulated charge and it can last from some seconds up to several hours, which obviously cannot be tolerated.

Ohmic RF-MEMS switches also present metal-to-metal ohmic contacts to establish a low-impedance path between the input and output parts leading to a further failure mode. High temperature gradients induced by large electric current, rough surfaces and friction, enable metals to form micro-welding points. The ability of a switch to self-release, depends on the overall area of welded joints and on the restoring force. In such case, the self-release of a movable electrode could be impossible to occur without any external loading. Indeed, while accumulated charge tends to escape over time leading after a certain period to the device restoring, micro-welding joints could not break by themselves.

1.2 Active Heat-Based Recovery Mechanism

In order to counteract stiction failure an active recovery mechanism is proposed. This mechanism exploits the thermo-electro-mechanical properties of different materials in order to release the stuck part of the device. The proposed mechanism is based on a highly resistive polysilicon serpentine which may be placed either underneath the anchoring areas of a suspended electrode or in the surrounding area of the fixed lower electrode. As soon as the electrical current is driven through the serpentine, the temperature of its material (e.g. polysilicon) increases due to the Joule heating effect. The induced heat speeds-up the charge dispersion and at the same time introduces shear and restoring forces as a result of material expansion. These two processes contribute to release of the stuck device.

To our knowledge the mechanism exploiting thermal properties of materials has never been used before in improving reliability issue of RF-MEMS devices. Current work appears to be one of the first attempts of implementing such an approach in the mentioned context. The main advantage of the proposed solution is its applicability to RF micro-switches of any topology by means of minor changes in the original structure design. The mechanism can be activated only in the case of failures, and it does not affect the normal operation and the behavior of the device.

1.3 Structure of the Thesis

This thesis is arranged as follows. ***Chapter 2*** provides an overview on the structure and the principle of operations of different types of RF-MEMS devices and on the State of the Art in such a field. ***Chapter 3*** contains an overview of recently developed techniques for preventing the adhesion of movable components and to release the stuck suspended parts of MEMS devices. The effectiveness and drawbacks of such approaches will be also commented. ***Chapter 4*** is dedicated to a comprehensive analysis of the causes of stiction and micro-welding phenomena in RF-MEMS switches. This section considers also the relation between the type of switches and their failure mode. The proposed heat-based self-recovery mechanism to counteract stiction and micro-welding failures in RF-MEMS switches is described in ***Chapter 5***. It discusses both the mechanical aspects and the thermo-electrical characteristics of the underlying mechanism. ***Chapter 6*** provides the details about some design simulations and experiments. The simulations have been performed by means of the ANSYS tool and compared against analytical calculations and experimental results. Conclusions are drawn in the last chapter of the thesis. Some appendices will eventually report the tables of physical properties of materials used in the simulations as well as the most important analytical calculations.

Chapter 2

State of the Art

The term MicroElectroMechanical Systems (or MEMS) addresses a wide class of Microsystems characterized by micro moveable and deformable parts that can be integrated with signal-processing electronics on a single chip. The field of MEMS has emerged about 40 years ago, in parallel with the progress and improvement of integrated circuits (ICs) fabrication technology platforms. Moreover, a significant contribution has been given by comprehensive studies of mechanical, physical and chemical properties of the materials involved in semiconductor manufacturing [1]. Such efforts resulted in appearance of the first microsystems that were designed to provide either sensing function (sensors) or perform a mechanical motion (actuators). The experimental activities, made on the earliest prototypes, have demonstrated a great advantage of MEMS devices over their standard counterparts, mainly in terms of low fabrication cost, high sensitivity and low noise. Since then the field of MEMS has been experiencing rapid growth.

2.1 MEMS Sensors and Actuators

The main function of MEMS ***sensors*** is in transduction of the mechanical displacement of their movable components into electrical signal. For instance, one of the first developed pressure micro-sensors exploits piezoresistive properties of doped silicon [1]. The sensing element is incorporated into the thin silicon membrane; when membrane experiences mechanical strain, deformation or bending, the resistance of the sensing element changes. The difference in the resistance value is tracked by integrated read-out electronics. Alternatively, another pressure sensor was realized by the group of Chavan et al [2]. In this case the membrane is designed as a movable electrode suspended over the fixed one that is housed in the substrate. The membrane is realized by means of two layers of different materials: the layer of conductive metal (Au and Cr) deposited on top of silicon oxide. Two electrodes, insulated by semiconductor, define a variable capacitor, the capacitance value of which depends on the distance between those electrodes. Obviously, the membrane position is influenced by pressure; thus, for sensing the pressure value, the signal processing unit is designed to detect variations in capacitance of the described varactor (i.e. variable capacitor). Of course, the variety of pressure sensors are not limited by the two designs discussed above. There are many other methods to sense this physical value including, for example, exploitation of piezoelectric materials [3], electronic resonance [4] or optical detection techniques [5].

MEMS technologies enable many other sensors for detecting a wide variety of physical phenomena. Among them there are accelerometers and gyroscopes [6], thermometers [7], strain gauges [8], microphones [9, 10], and magnetic field sensors [11], micromirrors for optical applications [12], ink-jet printer heads [13, 14] etc. Moreover, MEMS sensors can be designed to detect DNA, chemical concentration or pH of certain solutions. For this purpose the sensing element of MEMS device should be “functionalized”, i.e. covered by special material that are able to absorb or bind with certain molecules. The attached molecules change the properties of the movable component, such as resistance or resonant frequency that again are detectable by integrated electronics. Such type of sensors is widely used in biological and medical applications.

MEMS ***actuators*** are designed to generate the mechanical motion starting from other energy sources. The actuation methods include electrostatic, magnetic, thermal expansion [15], piezoelectric, pneumatic [16, 17], electrochemical reactions [18] etc. Figure 2.1 demonstrates an example of lateral thermal actuator designed by Mankame [19]. It consists of two arms of the same length, but different width. Under the same current the thin arm reaches higher temperature T1, which causes its greater expansion and deflection of the whole structure towards the thicker beam.

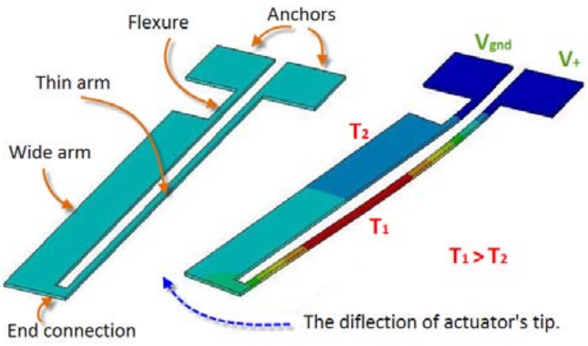

Figure 2.1: Lateral thermal actuator.

Recently, a novel class of MEMS devices has emerged. The so called energy scavengers are intended to capture energy from the environment and convert it into electric power. One of the main drivers in pushing forward the development of such devices is represented by the recent fast growth of wireless devices. The main power source for mobile phones, Personal Digital Assistants (PDA's), Radio-Frequency Identification microchips (RFID-tags), cardiac pacemakers etc., is a battery. In many cases the battery has relatively short lifetime compared to the application needs; another drawback is that the battery should be replaced after the discharge, that is impractical or even hardly feasible (as for example for medical microchips incorporated in human bodies or for space applications devices). Although autonomy of such devices can be enhanced by decreasing their power consumption, the improvement of battery lifetime is still the main way to make wireless electronic components more efficient. The development of energy scavengers has become one of the promising solutions for extending the wireless power supplies operation time. They can be employed either in combination with the batteries or as unique power supply, depending on the specific application. The sources of environmental energy and the mechanisms for its conversion into electric power are similar to the already described concepts for conventional MEMS sensors. Vibrations, mechanical stress and environmental impact (such as solar radiation, temperature) induce the piezoelectric [20, 21, 22], electromagnetic [23], electrostatic [24], thermoelectric [25, 26, 27] effects and result in generation of electric current. An interesting example of energy scavenger application reported recently in the literature is illustrated in Figure 2.2. Potkay and his colleagues [28] have developed a piezoelectric based micro-dimensional power source that captures the energy generated by periodic artery contractions. This device is intended to support implanted Microsystems and offers rather long life-time without any need of replacement.

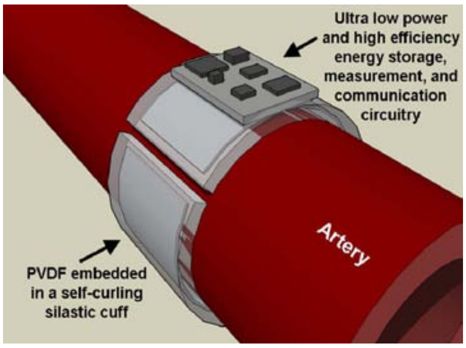

Figure 2.2: The figure shows an implanted arterial cuff power source (energy scavenger) integrated into a self-powered blood pressure sensing system.

2.2 Fabrication of MEMS Devices

The basic microfabrication process for semiconductor devices (i.e. ICs - Integrated Circuits) is a sequence of steps during which a device is manufactured layer-by-layer on a wafer made of certain material. The most frequently used material for wafers is highly pure single-crystal silicon. Such choice could be explained by several reasons: firstly, because silicon is widespread in nature, and thus it is relatively inexpensive; secondly, the seeds of amorphous silicon could be rather easily processed, purified and grown into single-crystal ingots (boules) by using Czochralski technique [29]. Depending on technology requirements the diameter of ingots may vary from 24.5 mm to 300 mm. The boule then is sliced into thin disks of several microns each and polished to obtain the ready-to-use wafers (Figure 2.3). Another popular material for wafers is gallium arsenide, but usually it is considered only for specific applications, because of its characteristics and higher cost compared to silicon.

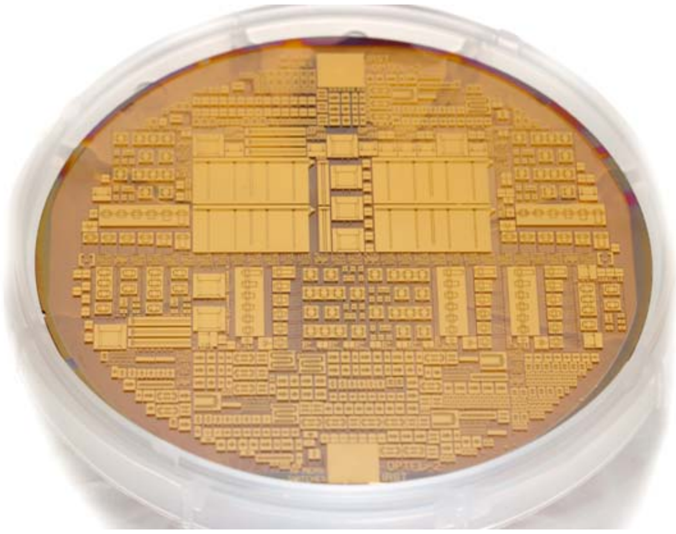

Figure 2.3: MEMS 4 inches quartz wafer in FBK technology.

As it was mentioned above the IC fabrication process involves many technology steps, but all of them aim at the patterning, deposition or removal of different materials from the wafer surface. Among the technology steps to deposit a layer of a certain material, commonly used techniques are the Physical Vapor Deposition (PVD), Chemical Vapor Deposition (CVD) and Electrochemical Deposition (ECD) [30]. The main concept of PVD is to deposit a desired material in the form of vapor onto wafer surface where it cools down to the condensation point, transits to the liquid phase and forms a thin film. The CVD process involves covering the wafer with special chemical solutions; the growth of a new layer is based on chemical reactions on the wafer surface turning the gas molecules into solid matter. In the ECD method the biased substrate is immersed into a bath containing charged metal ions. The layer of material is formed by means of electrochemical reaction.

Both Wet and Dry Etching processes were developed for the purpose of removing certain material from selected areas on a wafer. During the wet etching, a wafer is put into solution (etcher), which modifies or eliminates the unwanted material by means of chemical reaction. As an example, silicon oxide is usually etched by hydrofluoric acid. Alternatively, a wafer could be exposed to the bombardment of plasma ions. The collision between the ions and the material molecules results in the removal of the latter ones.

Finally, patterning is usually performed by means of photolithography process. This method allows removing certain parts of material from a wafer resulting in the desired topology of devices. For this purpose the wafer is covered by a layer of photoresist. The photoresist is a special kind of polymer that changes its properties under exposition to UV (UltraViolet) light. This material can be of two types: positive and negative. Under the radiation, UV or X-rays the polymer chains of positive resist break down, whereas the negative resist become tighter. Depending on the type of photoresist, the mask for photolithography is designed either to keep in shadow a certain area or vice versa (Figure. 2.4, [30]). However, after the light exposure, the weak part of material can be removed by immersing the wafer into a solution also known as developer.

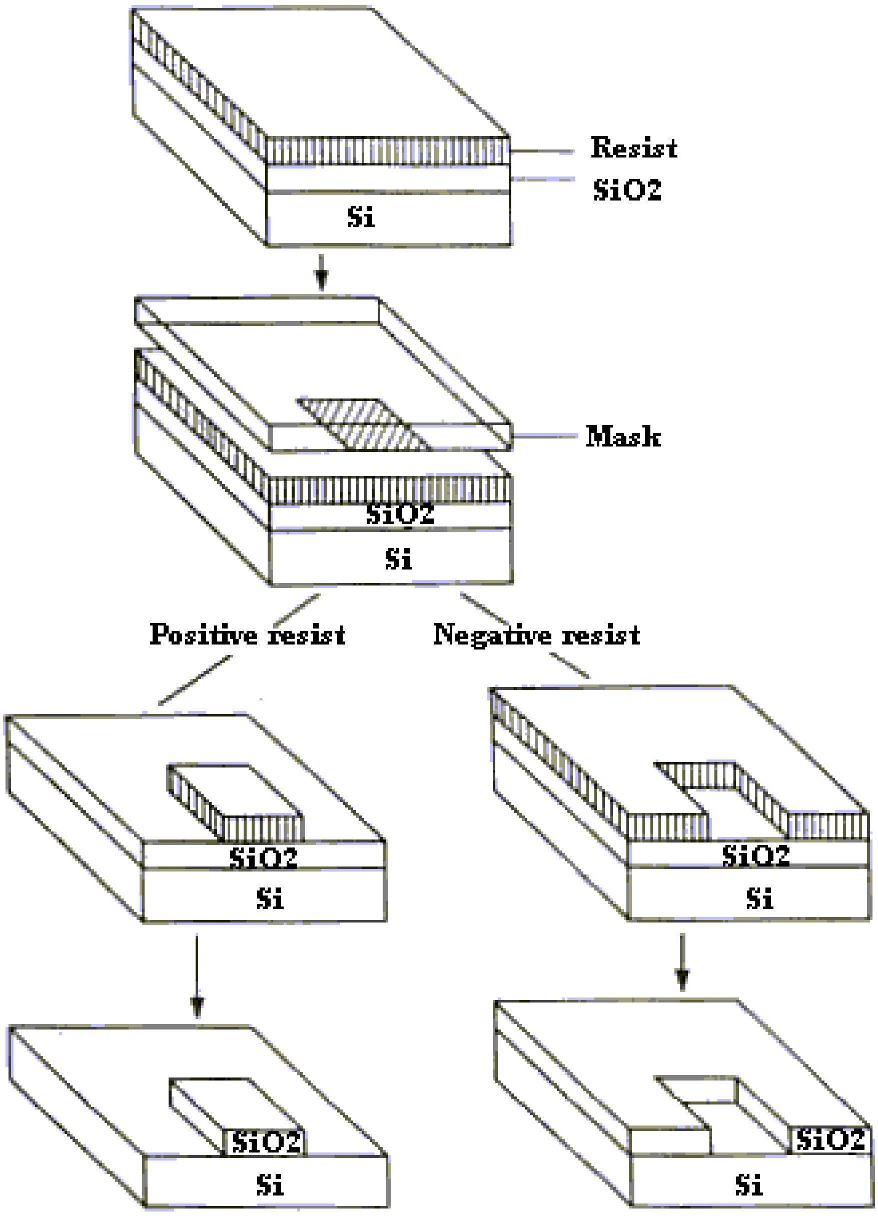

Figure 2.4: The difference of photolithography processes with positive and negative photoresists.

The very first attempts to manufacture MEMS structures were made on the basis of well developed technology processes for microelectronics industry. Usually Microsystems are manufactured by means of Bulk or Surface Micromachining fabrication technologies. During the bulk micromachining process a part of material is removed from the substrate in order to form movable mechanical parts of MEMS devices. Whereas, surface micromachining involves the growth and selective removal of layer on top of a silicon substrate.

One of the first pressure sensors [1] has been made using a fabrication process based on bulk micromachining technique. Figure 2.5 provides some details regarding the manufacturing of this device [1]. The first step here is “growing”an oxide layer (SiO_2, silica) on the surfaces of the silicon wafer. For this purpose the wafer is placed into a furnace at very high temperature. Moreover, the concentration of oxygen in the gas inside the furnace is also rather high. These conditions are appropriate to stimulate an oxidation of silicon, and thus the layer of SiO_2 starts generating at all the edges of the wafer (Figure 2.5b). It should be mentioned that SiO_2 is a good thermal and electrical insulator, and so it serves as substrate protection during the subsequent fabrication steps. In the next step a layer of photo resist is deposited (Figure 2.5c). The photolithography mask is designed to open a “window”in this layer (Figure 2.5d). When the wafer then is immersed into a bath with hydrofluoric acid, the layer of photoresist, in its turn, serves as a mask for silicon dioxide; so, the acid etches SiO_2 only at the window region (Figure 2.5e). Acetone is used in the following step to remove the photoresist (Figure 2.5f). After that, the wafer again passes through etching process. This time, the etchant is aggressive for silicon and has almost negligible effect on SiO_2. Again, only the material at the window region will be removed (Figure 2.5g). In the next step another wafer is bonded on top of the basic one (Figure 2.5h). The top wafer is mechanically polished (thinned) or etched until its thickness will reach the desired value for the suspended membrane (Figure 2.5i). Finally, the piezoresistive sensors are made on the top of the membrane (Figure 2.5j). These sensors change their resistivity depending on the membrane bending (e.g. mechanical stress) and the resistance variation is handled by designed on-purpose read-out electronics.

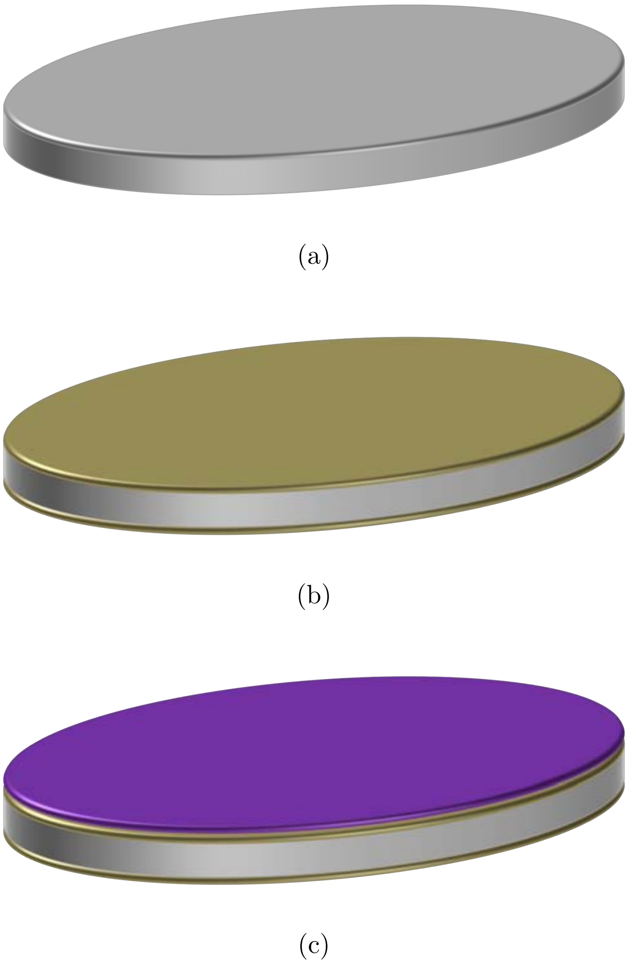

(a)

(b)

(c)

Figure 2.5: The sequence of technological steps in bulk micromachining process. (a) initial silicon wafer; (b) generation of SiO_2 layer on the edges of the wafer; (c) deposition of photoresist.

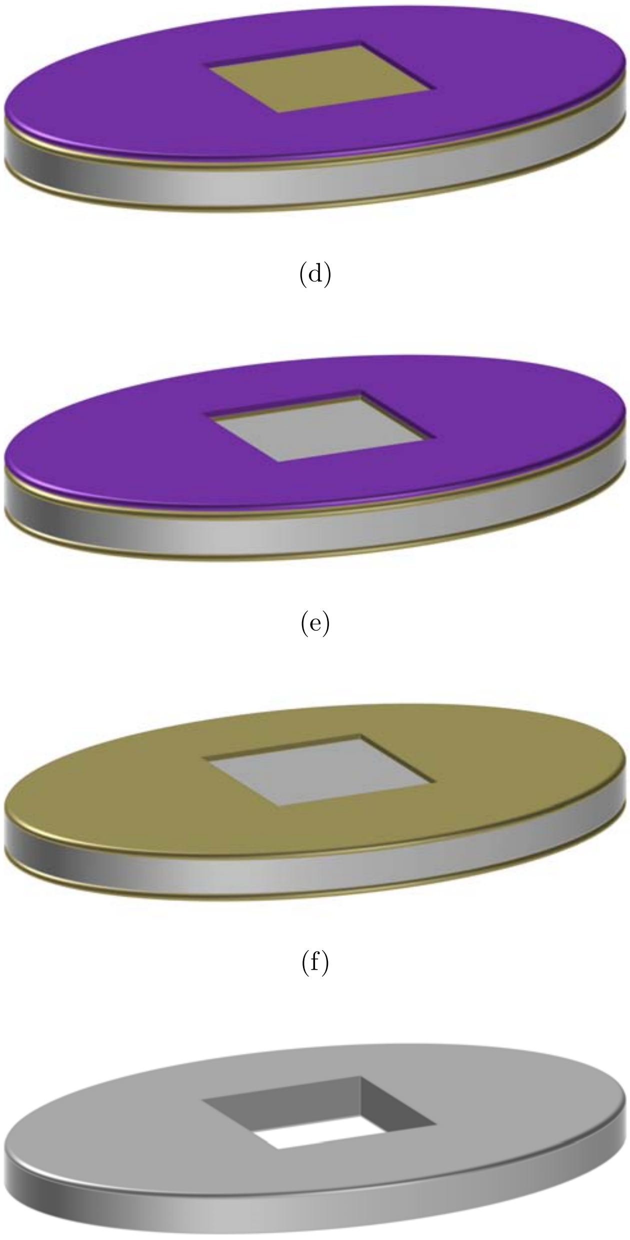

(d)

(e)

(f)

(g)

Figure 2.5: The sequence of technological steps in bulk micromachining process. (d) definition of openings in the photoresist layer by means of photolithography; (e) etching of SiO_2; (f) removing of photoresist; (g) again etching of SiO_2.

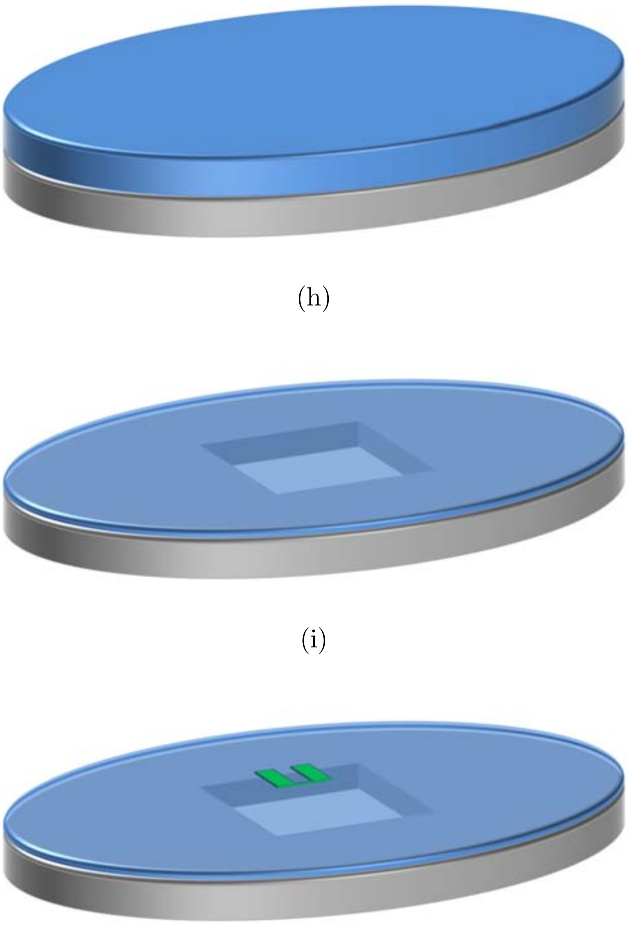

(h)

(i)

(j)

Figure 2.5: The sequence of technological steps in bulk micromachining process. (h) bonding another wafer on the top of the basic one; (i) polishing of the bonded wafer; (j) definition of piezoresistive sensors.

A typical surface micromachining process is depicted in Figure 2.6. In this case the so called sacrificial layer is deposited first on the top of the wafer (Figure 2.6a). This layer temporarily fills-in a gap between the substrate and the suspended MEMS cantilever (still to be processed). Just after the patterning of sacrificial layer, the layer of structural material is deposited on top of it (Figure 2.6b). When the shape of the component is defined (Figures 2.6c– 2.6e), the sacrificial layer can be etched enabling this component to move as it is shown in Figures 2.6f– 2.6g (i.e. release).

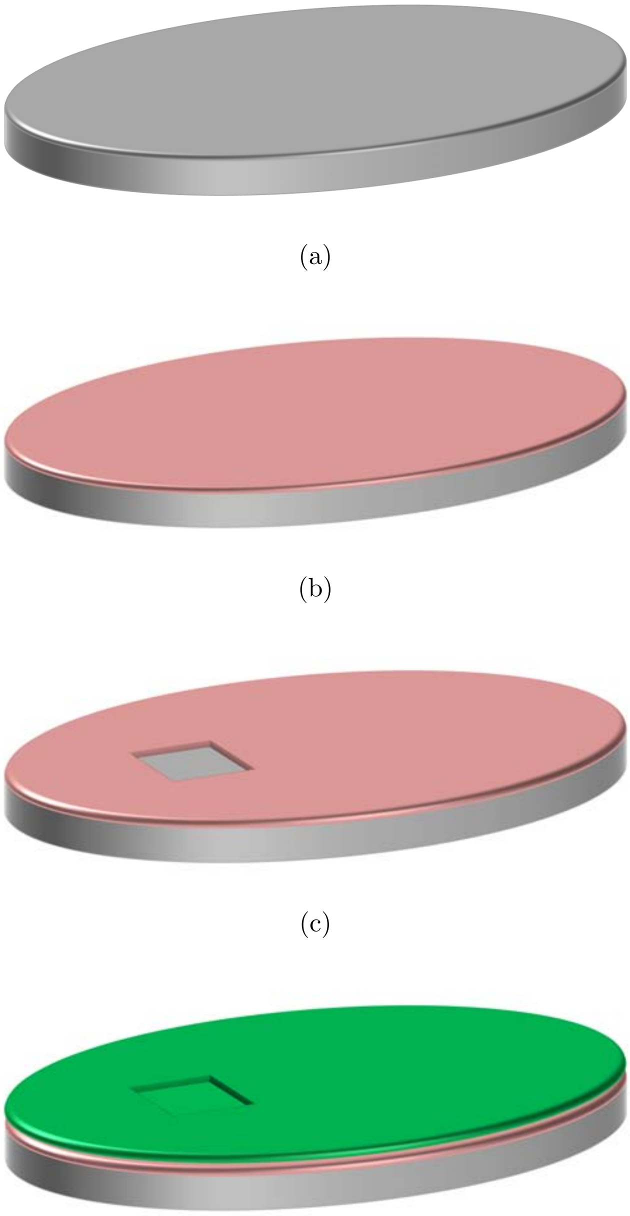
(a)
(b)
(c)
(d)

Figure 2.6: The sequence of technological steps in surface micromachining process. (a) initial silicon wafer; (b) deposition of the sacrificial layer; (c) patterning of the sacrificial layer; (d) definition of structural layer;

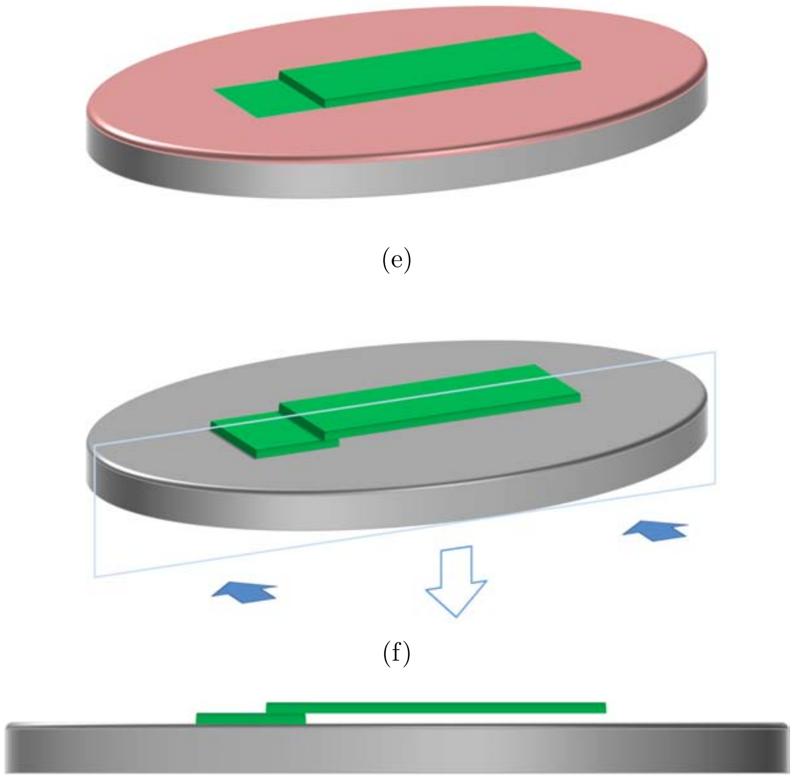

(e)

(f)

(g)

Figure 2.6: The sequence of technological steps in surface micromachining process. (e) patterning of the structural layer; (f) isometric view and (g) front view of the device after removing of the sacrificial layer.

Thus, both techniques allow the manufacturing of a variety of three-dimensional elements, including mechanical structures such as cantilever beams, bridges or membranes, widely used in design of Microsystems-based sensors, actuators and networks.

In the last years the technologies for MEMS fabrication have been supplemented by employment of new materials and development of new processes. The main reasons have to be found in the need for materials with different characteristics (mechanical, electrical and so on) compared to Silicon. For instance, polymers (parylene, polyimide, SU-8 etc) are an alternative to the single-crystal silicon. These are low-cost materials and can also enable the easier packaging and integration of Microsystems. Unlike silicon, polymers also offer additional properties such as biocompatibility, biodegradability, transparency, mechanical shock tolerance, durability, chemical stability and so on. The main obstacle preventing the use of polymers is their quite low melting point and related mechanical instability. In the short temperature range the properties of polymers change drastically, so that material starts to exhibit viscous deformations. Thus there are a few application areas where polymers are employed so far.

2.3 RF-MEMS Devices

One of the various application fields of MEMS that has emerged in the past decade is the class of devices specifically designed for Radio Frequency applications (RF-MEMS). These devices have recently found a number of application areas, starting from modern wireless communication networks, global positioning systems (GPS), radars, mobile phones, automotive sensors, robotics, military and consumer electronics. The growing interest in RF-MEMS devices is fed by their advantages in comparison to their conventional semiconductor counterparts, such as low-cost, high performance, large reconfigurability, low insertion loss, good linearity, high quality factor and low power consumption. The most significant developments of the RF-MEMS devices and their examples and application areas, will be discussed in the next paragraphs.

The industry of cellular phones is perhaps the most promising application area for RF-MEMS switches. The modern cellular network is a rather complicated system which allows broadcasting an audio signal via wireless communication equipment. Nowadays there is no single standard for cellular network architectures among mobile operators in different Countries. New generations of wireless telephone technology emerge roughly every

10 years, but this time slot is insufficient for complete reconfiguration of the networks from one standard to another. Therefore along with the most popular at the moment 2G (the second generation) GSM standard, it is still possible to find the 1G analogue standard NMT as well as 3G standards GSM EDGE, UMTS, CDMA2000 etc. Apart from a number of differences at technology level, each standard works in different frequency bands [31]. For example, the operation frequency range of mentioned GSM standard varies from 450 MHz to 1900 MHz.

In order to assure compatibility, the manufacturers of mobile phones have to design the transceiver platforms which are able to support as many different standards and their frequency bands as possible. Nowadays such flexibility is achieved by using the combination of duplexers, transmit/receive (T/R) switches and band switches [31]. Each of the mentioned devices is intended to support a certain frequency range typical for one of the existing standards, thus the combination of these devices integrated in the cellular phones architecture could provide a partial or complete coverage within the existent cellular networks.

The antenna switches can be at least of four different types, depending on the technology used for realization of these devices (SOI, CMOS, compound semiconductors or PIN diode). All of them can achieve the frequency up to 5GHz and at the same time consume just 15μW, demonstrate low insertion loss (about 0.8dB) and good isolation (up to 35dB). Even though the conventional switches have indisputable advantages, there are several technology limitations restricting further improvements of their performance.

The alternative solution could be provided by RF-MEMS switches, which have the considerable advantages such as low power consumption, lower insertion loss, higher isolation, and good linearity in comparison to the conventional solid-state switches (Figure 2.7, [31]). But there are several issues that prevent the RF-MEMS switches to be integrated into the modern telecommunication systems. Among them are the lack of performance stability, relatively short lifetime due to mechanical and electrical failures, low process reproducibility, packaging and integration with standard technology. All this issues will be discussed later in this Chapter.

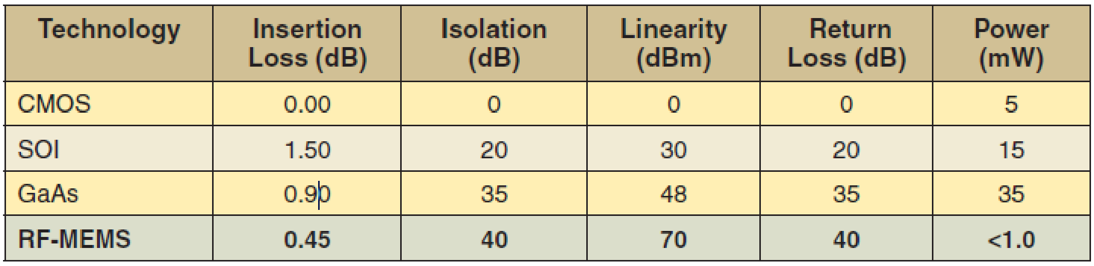

Technology	Insertion Loss (dB)	Isolation (dB)	Linearity (dBm)	Return Loss (dB)	Power (mW)
CMOS	0.00	0	0	0	5
SOI	1.50	20	30	20	15
GaAs	0.90	35	48	35	35
RF-MEMS	**0.45**	**40**	**70**	**40**	**<1.0**

Figure 2.7: Typical specifications for a single-pole, double-throw RF switch at 6 GHz compared with conventional IC counterparts.

2.3.1 RF-MEMS Switches

Switches are the most mature and comprehensively studied components among all RF-MEMS devices developed so far. As it was mentioned before the main functionality provided by switches is the isolation or connection of two lines (input-output), carrying a certain electrical signal. In the topology of any MEMS-based RF switch this function is realized by means of mechanically movable components usually in the form of membranes or beams clamped at one (cantilever) or both ends (clamped-clamped beam) and made of conducting material like gold, aluminium or nickel. In the neutral (i.e. rest) position this component is suspended over the fixed electrode; if the switch is electrostatically actuated, the central plate (or cantilever) experiences bending (or displacement) towards the specified direction. When the controlling voltage is large enough (i.e. pull-in), the plate reaches a contact with the underneath or lateral structure and, depending on the design, closes or opens the circuit transmitting or blocking an electrical signal (series or shunt switch respectively).

There are several properties on the basis of which the RF switches can be classified. The most significant of them are actuation techniques, the shape and displacement direction of the movable component, and so on.

Up to now, the literature contains description of four actuation mechanisms: electrostatic [32], electromagnetic [33], piezoelectric [34] and thermal [35]. The prevailing one is the electrostatic method, which offers low power consumption (virtually zero power consumption) and short actuation time (the time required for the switch to change its state). Many designs integrate a combination of actuation mechanisms [36, 37, 38], for example, in the thermally actuated switch, electrostatic forces could be used to hold the plate in the pulled-in state. Such technique results in extremely low power consumption once the switch has been actuated.

As it was already mentioned, the shape of the mechanical component could be done in the form of diaphragm, plate, supported by different number of suspensions, cantilever or membrane and can move either vertically or laterally.

Another important aspect of RF-MEMS switches is the type of contact between the suspended movable part and the underneath electrodes. There are two main classes of switches: capacitive and ohmic. In the ***capacitive switch*** (Figure 2.8) the two electrodes (i.e. the suspended movable plate and the underneath fixed electrode) are electrically separated by means of a dielectric layer. In the neutral position, the central membrane of this device implements the low capacitance to ground (closed switch), whereas in the pulled-in state the capacitance can increase up to a few orders of magnitude (high capacitance) and short to ground the RF signal (open switch).

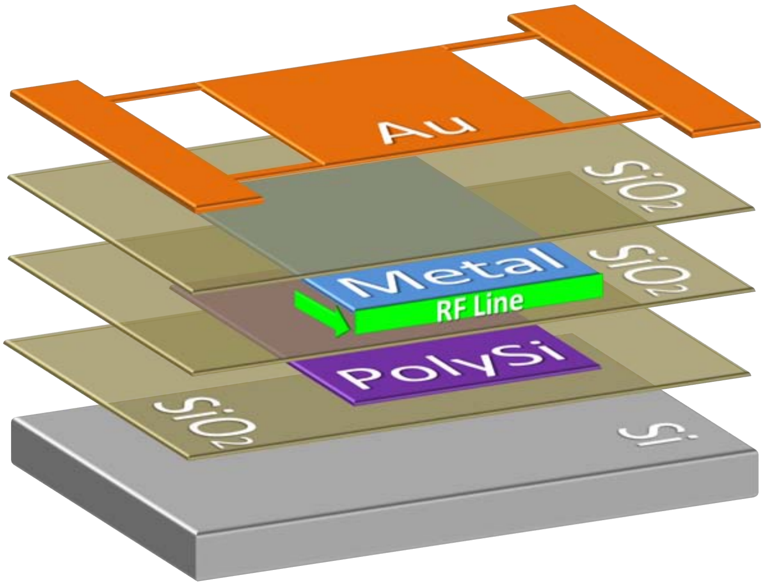

Figure 2.8: Typical cross-section of the capacitive switch.

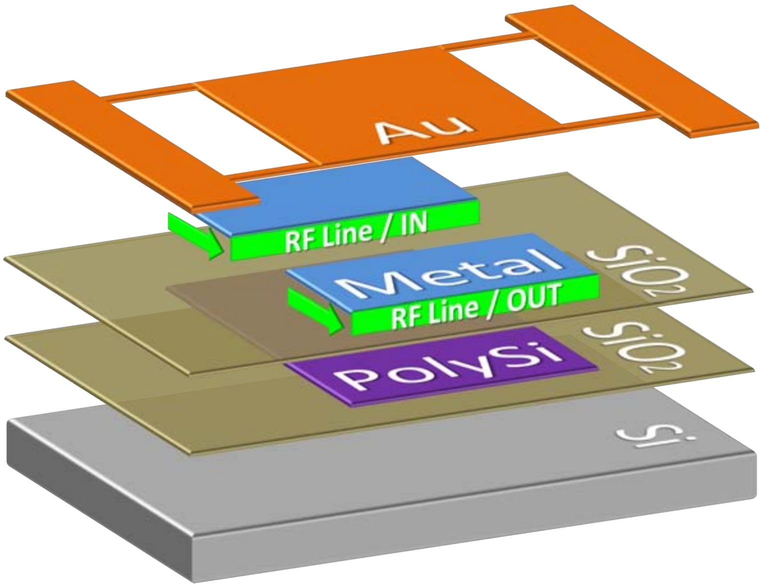

Figure 2.9: Typical cross-section of the ohmic switch.

These switches may also act as an RF-MEMS variable capacitor when the actuation voltage is so that the overall displacement of the movable component from the neutral position, down to the actuation electrode does not exceed 1/3 of the length of the gap. This type of capacitor has limited tuning range (i.e. variation of the capacitance value).

On the contrary in the ***Ohmic switches*** there is no any intermediate layers between the movable and the fixed electrodes. When the central plate of ohmic switch is in the pulled-in state, it closes the circuit through which the RF signal is passing (Figure 2.9); whereas the neutral position of the central plate corresponds to the open switch mode.

2.3.2 RF-MEMS Inductors

Another promising application of RF-MEMS technology is the implementation of ***inductors*** (passive electronic components that store magnetic energy). An inductor is simply a loop or a coil of conducting wires, but in spite of apparent simplicity, the implementation of these devices by means of conventional IC technologies is rather challenging task. Associated fabrication processes allow realization of inductors on CMOS or SiGe substrates in the form of metallic spiral as it is demonstrated on Figure 2.10, [39].

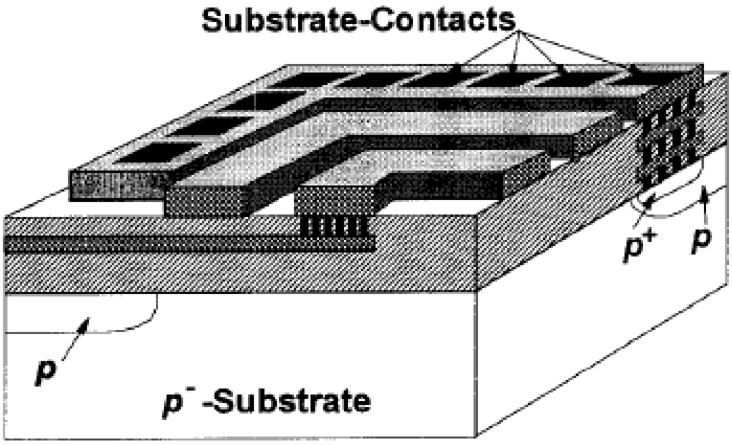

Figure 2.10: Schematics of a spiral inductor integrated on a silicon substrate.

Such planar design requires relatively much space on a chip and causes a lot of problems linked to parasitic capacitance between spiral turns and capacitance associated to the substrate. In addition, there are two more disadvantages: the resistance of the spiral structure and eddy currents generated in the substrate during the operation of the device. All these peculiarities limit the Q-factor (quality factor) of the inductor. Nowadays the performance of planar inductors can be improved with the help of software dedicated to electromagnetic simulations; it allows the engineers to perform optimizations of the design in order to achieve higher inductance with the lowest possible series resistance associated to this component. Moreover, the employment of alternative substrates (as, for example, ceramic, Figure 2.11, [40]) with rather high resistivity enables the reduction of eddy currents and related parasitic capacitance and losses. Thus, the Q-factor of the device from the Figure 2.11 is around 30, which is 7 times higher than the Q-factor of the samples realized on silicon substrate.

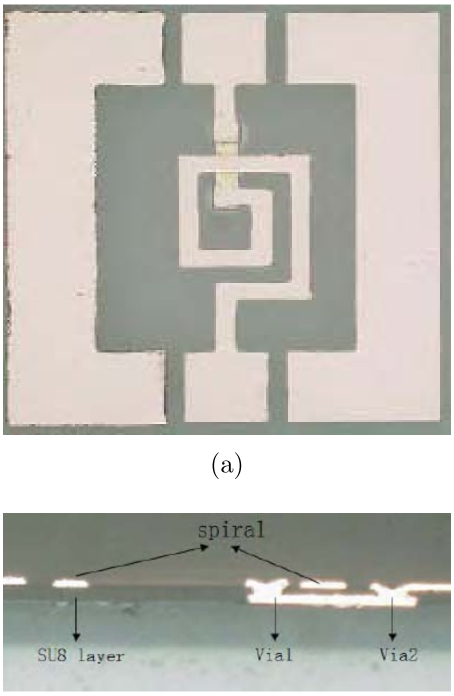

(a)

(b)

Figure 2.11: Example of the integrated plane inductor for RF application. (a) The photo of inductor realized on the ceramic substrate; (b) the cross-section view of the same device.

The inductors implemented by means of RF-MEMS technology are characterized by very high Q-factor. Such performance is the result of using micromachining techniques in order to develop the spiral structures suspended over the substrate, and thus eliminate the just discussed limitations of the inductors performance. There are several approaches to the realization of this class of three-dimensional components; each of them has different influence on the operating characteristics of the final device. The first one simply involves the fabrication process, either surface or bulk micromachining step, in order to separate the metal layer that shapes the spiral from the substrate by small air gap (Figure 2.12). This measure results in improvement of inductors performance, but does not eliminate completely the parasitic capacitance. To address this issue, the loops of conductor can be placed perpendicularly to the substrate (Figure 2.13). The structures shaped in this way are referred to as solenoid inductor. The 2.67 nH inductor shown on the Figure 2.13 has been reported to have the Q-factor around 16.7 at 2.4 GHz. Another mentioned advantage of solenoid inductors in comparison to the spiral ones is that they demonstrate a linear relationship between the inductance and the number of turns.

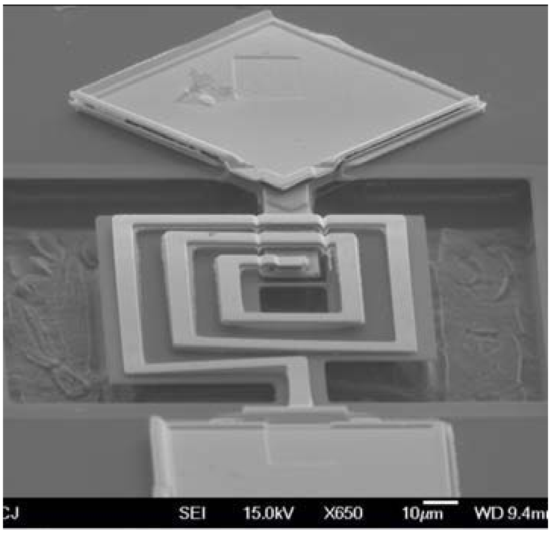

Figure 2.12: An example of the inductor suspended over the substrate.

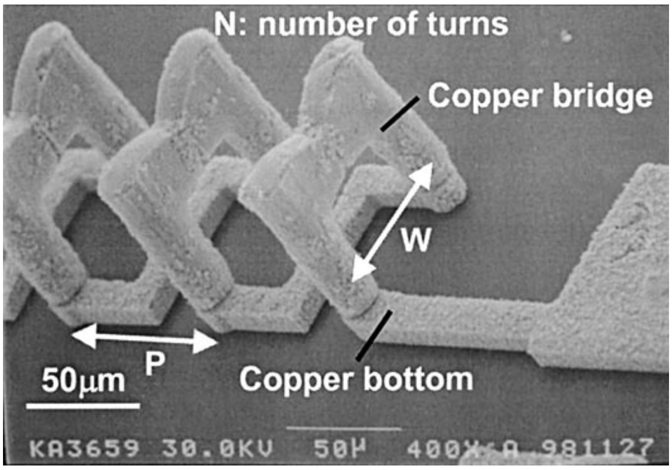

Figure 2.13: An example of the inductor in which the loops are placed perpendicularly to the substrate in order to eliminate parasitic capacitance.

The inductors with high Q-Factor are, together with variable capacitors, basic elements for many different passive and active circuits and can substantially reduce the phase noise or power consumption of oscillators and amplifiers. Also, they are widely used in low-loss impedance matching networks and filters.

2.3.3 Complex Networks

The previously discussed RF-MEMS devices can be successfully used in building up the complex functional blocks and networks that are widely spread in the telecommunication field. The main functionality of these components is in transmitting either RF or Microwave signals. As it was mentioned in [41], depending on the specific application, the set of RF-MEMS components may form different type of complex networks. Thus, they enable realization of phase shifters [42, 43] and True Time Delay lines (TTD-lines) [44] for antennas and radars, reconfigurable impedance matching networks [45] and switching matrices for the channels selection in satellites [46]. There are two main advantages in realization of complex blocks with the help of RF-MEMS components. First of all, the performances of such systems are reported to be rather high. At the same time these blocks can be easily reconfigured, so their capabilities are much more extended in comparison to conventional counterparts.

2.3.4 Packaging and Integration of RF-MEMS

Most part of applications, that involve discussed RF-MEMS devices, are potentially a subject to mechanical shock loadings. Besides, the operational conditions of such apparatus are far from ideal, therefore the components very commonly suffer from the presence of dust or other particles. Not less important is the problem of integration of MEMS devices with standard IC electronics. Thus, the successful commercial employment of these devices is strictly depends on the effectiveness of the proposed packaging and integration solutions.

There is no universal packaging technique, which may address the protection issue of all MEMS based components. Basically, the developing of the protective cap strongly relies on the requirements, the type of application [47] and the operational conditions [47] of the future devices.

Generally, the most common materials used in realization of packages are silicon, glass and ceramic [48]. The choice of material plays an important role in the further integration of the device in a certain functional block. In particular, the capping material would define the strategy for realization of the scheme of electrical signals interconnection and also the space, which should be allocated on the wafer for the devices to be packaged

The packaging solution for Radio Frequency MEMS devices, which is based on glass substrate has been proposed in [49]. The sandblasting technique is used in order to open the vertical vias in the cap. Subsequently the vias are filled in with gold, which enables to transmit the electrical signals from the device to the external outputs. An alternative approach to package the RF-MEMS devices (in particular switches) has been suggested in [50]. This technique requires the definition of BenzoCycloButene (BCB) rings around the device. The layer forming the rings is thick enough to assure the sufficient protection of the device from the harmful environmental impacts. The Coplanar Wave Guides (CPW), that transmit the electrical signals, are realized on the top of the device wafer, but pass underneath the BCB rings.

Another interesting solution was discussed in the work of A. Margomenos et Al. [51]. The proposed idea is to extend the fabrication process flow by several preliminary steps. These steps (based on the etching) are required in order to form in the silicon substrate the vertical vias and thus allow the access to the electrical signals of the device from the bottom side of the wafer.

Being a part of the certain complex functional block the RF-MEMS devices should enable a rather easy integration and interfacing to the other parts of this system. So, an additional requirement to the packaging is to provide the ability of simple final mounting of a chip including MEMS devices onto a board. To specify this issue, the definitions of first-level and zero-level packaging have been introduced [52]. The first level refers to a packaging solution performed on a device chip.

The electrical interconnect scheme is made available for the final mount of the MEMS chip. This is based for instance on Ball Grid Array (BGA), Dual in-line Package (DiP), Pin Grid Array (PGA) or Leadless Chip Carrier [53]. On the other hand, the zero-level packaging is commonly addressed also as Wafer-Level Packaging (WLP). This means that an entire device wafer has to be bonded to the package. The wafer-to-wafer bonding can be performed for instance by means of solder reflow, anodic bonding [53] or via the use of adhesive materials like SU-8 [54]. After the bonding step, the capped wafer must be singulated, which means to saw it in dies of smaller size (e.g. 1x1cm^2). Finally, the single die must be made ready for the final on board mounting, for instance by wire-bonding it to a carrier chip provided with leads for DiP or solder balls for Flip-Chip mounting [53]. In other words, a zero-level solution is an intermediate packaging stage which requires additional steps to get a chip ready for standard Surface Mount Technologies (SMT) like the ones mentioned above. This is necessary when dealing with MEMS devices as they need to be protected right after fabrication (for instance during the wafer handling and singulation).

Moreover, from the integration of RF-MEMS devices point of view it is rather important to find out the additional functionalities that may be permitted by certain package. Among the most promising solutions is the establishment of the interface between the CMOS circuitry and the passive RF-MEMS part of the functional block. Such interface should be realized directly on-chip through the exploitation of the package components. From one side the cap should provide the proper housing for the CMOS chip and from another side should also house the interconnect scheme for the signals interfacing. This allows getting a complete functional block (for instance an oscillator based on a MEMS resonator and a CMOS sustaining circuitry) packaged and ready for SMT. Because the RF-MEMS and CMOS part are obtained via different incompatible technologies, this solution is called Hybrid-Packaging [55].

The package enables another important feature. This is the hermeticity and the vacuum sealing; these features are available only in the particular packaging solution that has been chosen for the bonding of the package to the MEMS device. In the work of Nguyen [56] it has been demonstrated that a Q-Factor (Quality Factor) of a MEMS lateral comb-drive resonator is around 27 if the device is operated in air. The Q-Factor for the same device rises to about 50000 when it is operated in a vacuum environment. In general, it is rather difficult to maintain the vacuum condition within the package for a long period of time. Firstly, because there is a risk of the air leakages through the sealing, the other potential problem is an outgassing phenomena of the materials within the chamber (e.g. the sealing material or the MEMS device itself). This leads to a drift (i.e. degradation) over time of the capped MEMS devices performance. A remarkable solution which eliminates the described problem is offered by the use of the so called getters [57]. The getters are referred to as the materials, which exhibit very selective absorption properties with respect to certain species that commonly make a harmful influence on the hermetic vacuum of the package. Getter materials are usually arranged in thin films so that they can be easily accommodated within the cavity in which the vacuum condition must be enhanced and maintained. Getters are obtained by sinterisation of different materials to achieve the desired sensitivity to the gaseous species that must be trapped [58]. The effectiveness of getters has been demonstrated by D. Sparks et Al. showing that the Q-Factor of a MEMS resonator operated in vacuum condition is largely more stable over time when a getter layer is added within the chamber [59].

The sequence related to Wafer-Level Packaging will be discussed now in order to provide an additional information concerning the packaging and integration steps. Apart from the devices wafer (on the top of which the RF-MEMS devices are manufactured and allocated within dies distributed onto the wafer area), it is required to have second wafer that will serve as a package. On the second wafer it is necessary to realize vertical interconnects that have to be distributed in correspondence with the signal pads on the dies of the device substrate. A schematic view of both the RF-MEMS device and capping wafers is shown in Figure 2.14, [41].

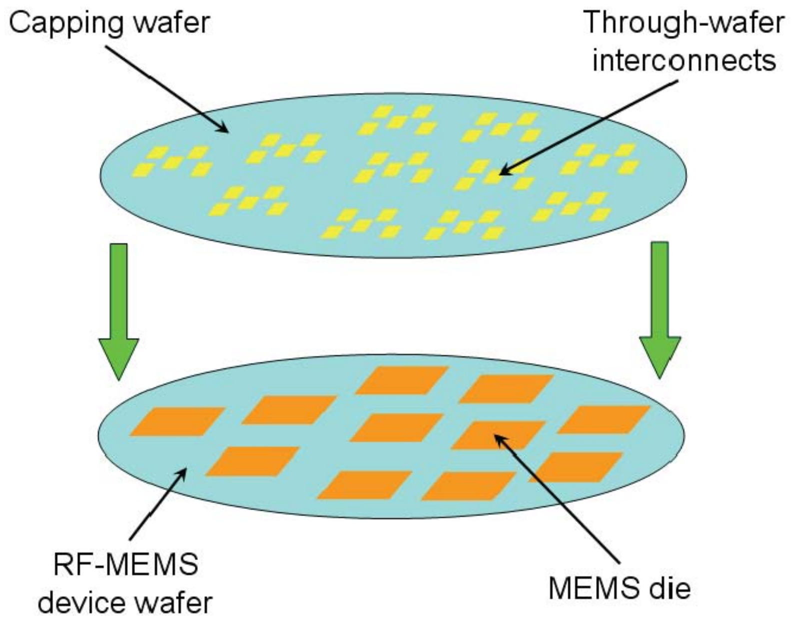

Figure 2.14: In wafer-level packaging a capping wafer with the interconnects scheme compatible with the distribution of electrical signal pads onto the RFMEMS device substrate is necessary.

When the second wafer is aligned with the wafer housing the MEMS devices, both of them must be brought in contact. After the wafer-to-wafer bonding, the capped RF-MEMS wafer is ready for subsequent singulation as it is shown in Figure 2.15. As a result the packaged RF-MEMS dies are ready for the flip-chip on board mount by means of solder balls reflow as it is shown in Figure 2.16.

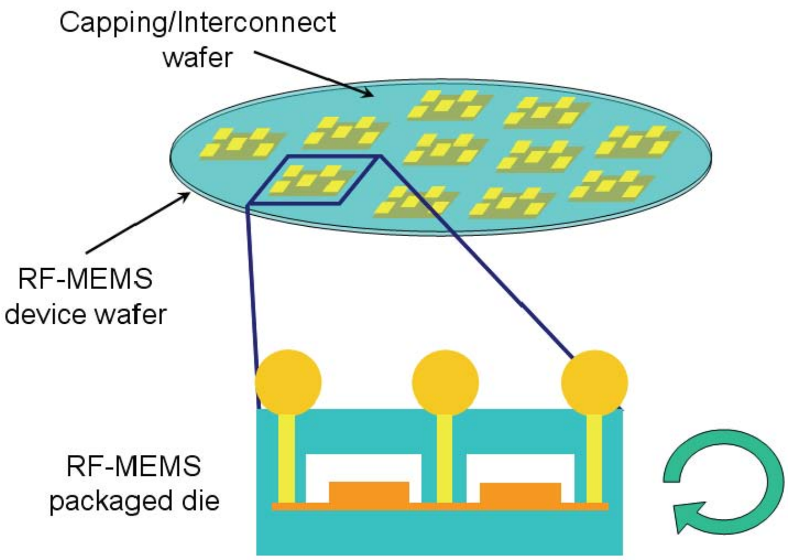

Figure 2.15: After the alignment of the capping part to the MEMS substrate the wafer-to-wafer bonding is performed. After the subsequent singulation the packaged RF-MEMS dies are available for SMT (see Figure 2.16).

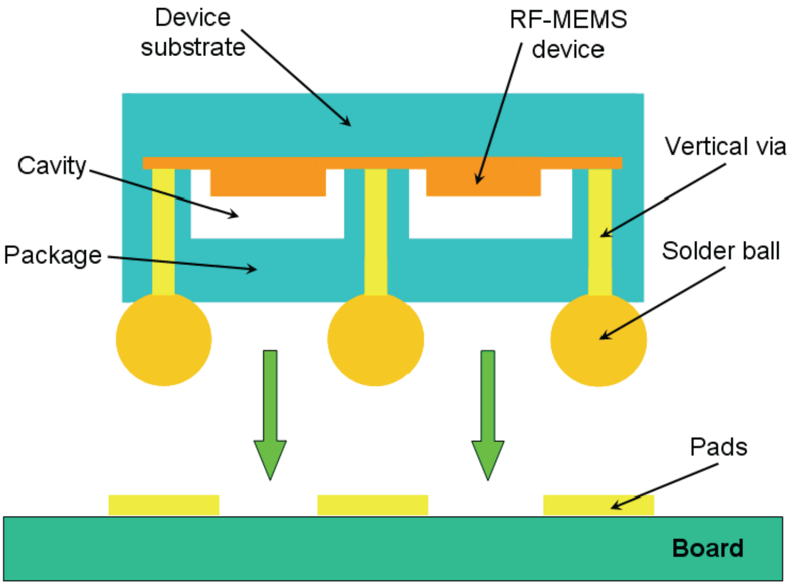

Figure 2.16: The final step is to flip the packaged MEMS die over the board performing the bonding by solder balls reflow.

2.4 State-of-the-Art in Reliability of MEMS and RF-MEMS Devices

In spite of the significant boost RF-MEMS-based devices and functional blocks would give to commercial RF and transceiver platforms and applications, their penetration into the market is still limited. The main reason to motivate the latter statement has to be sought in the relatively poor reliability that implementations based on RF-MEMS technology are still exhibiting. However, reliability of MEMS is a rather complicated topic revealing a consistent number of intricacies. On one side, the sources of malfunctioning of MEMS/RF-MEMS devices are multiple, and are linked both to environmental factors, like moisture, dust particles, mechanical shocks etc., as well as to causes linked to the normal operation of such devices, like aging, wearing, mechanical fatigue and so on [60]. On the other hand, procedures for the assessment of RF-MEMS reliability, like accelerated life-tests, are not so well established as in standard technology, e.g. CMOS. Given these considerations, it is clear that the efforts of the Research Community to address the reliability of MEMS have to be spent considering different points of view. This section includes the discussion about the most significant failure mechanisms, the proposed important findings and solutions for improving reliability aspect of RF-MEMS devices.

Generally any failure of RF-MEMS device can be classified as one of four principal causes - mechanical or electrical instability, improper packaging and damage effect causing by external environment.

- ***Fractures*** in the mechanical part of RF-MEMS devices represent the first considered reason from the class of mechanical degradations. Both impact forces and/or long cyclicling may lead to the moving device failure especially at the concentration points of bending stresses.

Typically the failures referred to short overload of the system is more inherent for brittle materials (silicon, silicon nitride); on the contrary, the cyclic loading may be destructive for the elements of structures made of metals such as aluminum or gold. Experimental measurements performed by the research groups of Muhlstain et al [61], Sharpe et al [62] and Chan et al [63] are significant in the described context. According to their findings, the single-crystal silicon specimen lives ranged from 10^6 to 10^{11} cycles, while for the polysilicon the number of cycles is in the order of 10^{11}. Concerning the robustness of the entire devices this characteristic would strongly depend on the topologic peculiarities of the samples. For instance, recently suggested designs of RF-MEMS switches have been reported to perform 10^{12} cycles if the movable part is realized as metal cantilever beam [64] and around 2×10^9 cycles for the aluminum nitride central plate shape [65].

- ***Creep*** (tendency of material to slowly move or deform permanently to relieve stresses) again is a material related issue, specific for metal-based devices. This effect was observed in steel held for long periods at high temperature. Bulk counterparts are less susceptible to creep, but this phenomenon is significant at a micro scale and may be present even at room temperature. Using the pure aluminum as a material for the movable beams could also cause the reduction of the device lifetime and this is one of the main reasons for which metals with higher melting point (like gold) are often preferred in the manufacturing of RF-MEMS devices.

- ***Delamination***. The multilayer cantilever beams, bridges or membranes may experience an internal stress even when they are at room temperature and with zero external loads. The origin mechanism of such stress-strain conditions is the difference in thermal expansion of materials. It results in ***delamination*** of structural part of MEMS device. The approach adopted for decreasing the impact of such an issue is using chemically and mechanically compatible materials, or multiple-layered structures to compensate for stress-induced bending, or polymers which have negligibly small intrinsic stress [66].

- ***Electromigration*** occurs under high current densities: atoms of conductive material are lifted by the current leading to open circuit failures. The phenomenon is material dependent and involves only conductors. It was reported that the critical DC current density above which electromigration effect happens, is about J_{max},DC=10 GA/m^2 in gold [67]. So, the design rules for RF switches should include the calculations of this limiting factor as well.

- ***Electrostatic discharge (ESD)***, is the instantaneous current flowing between two points with different electrical potentials and separated by an insulating layer (i.e. breaking of insulator). Antistatic coatings are used in standard IC to protect a device, but MEMS technology typically does not allow implementing such method. For this reason, the reliability vs. ESD must be considered starting from the design phase [68], [69].

- ***Degradation of dielectric***. Widespread MEMS problem is the charging that may occur in the dielectric layer. ***Degradation of dielectric*** limits the lifetime of electrostatically operated RF-MEMS devices. These phenomena are the consequence of the dielectric charging which occurs during the operating phase of the switch. This effect is triggered by the actuation voltage [70]. There are several strategies to mitigate the charge accumulation problem, like, for example, concerning the intensity of electric field in correspondence to the insulating layer, or the use of trap-free dielectrics.

- ***Stiction***. Small dimensions and light weight of RF-MEMS structures lead to considerable decreasing of the rate of restoring force and considerable domination of surface forces in the whole system. The most significant of them are the capillary forces, the molecular van der Waals force and the spurious electrostatic force, generated by the just mentioned charge accumulated in the dielectric layer. These types of loading may lead to the so called ***stiction*** failure. The term stands for "static friction"and denotes an adhesion of the device contact surfaces. For RF-MEMS switches this type of failure is very common and usually results in malfunctioning of the samples. The approaches to overcome stiction are either preventive or counteractive. Among the proposed preventive solutions are the considerable reduction of the contact area [71] or covering the structures by lubricants such as fluoro- or hydrocarbon coatings [72]. The stuck components could be also released by means of various energy input forms, such as electrostatic actuation [73] or vibrations generated by laser [74]. In the first case an additional specially designed electrode should be activated in order to generate a restoring force, while in the second case the resonance effect is exploited to release the structure.

  As it was mentioned in the introductory part this thesis is devoted to one of the mechanisms specifically designed to overcome the stiction failure of the RF-MEMS switches. The detailed description of this mechanism will be provided in the next chapters. Here it should be just mentioned that the proposed approach belongs to the counteractive type of solution.

- ***Wear***. The problems of stiction and ***wear*** (the erosion of material due to interaction of structural elements surfaces) have been partially solved by providing protective interfaces, such as molecular films -

dichlorodimethylsilane [75], fluorocarbon [76], diamond like carbon (DLC) [77] or gas phase lubrication [78]. Unfortunately, molecular thin films are worn away after extended operation and the gas phase lubricant must be continuously present to replenish the contact region.

The problem of reliability is quite challenging and often cannot be solved by using approaches borrowed from standard IC techniques. Because of this motivation, advancements of research are extremely important for the further successful application of RF-MEMS technology.

Chapter 3

Stiction of RF-MEMS Switches

3.1 Reasons of Stiction

One of the critical issues of RF-MEMS switches reliability is related to the stiction phenomenon. The term stiction (sticking friction) refers to the adhesion between the suspended component of the switch and the substrate. The main reasons causing stiction as well as proposed solutions to overcome these failures are discussed in this chapter.

In electrostatically operated MEMS switches, a voltage is applied between the suspended membrane and the underlying fixed electrode. Depending on the bias level the suspended metal part moves towards the lower electrode because of attractive electrostatic force. When the pull-in voltage is reached, the suspended part collapses onto the bottom electrode, thus bringing the switch in the ON state. The presence of an insulating layer between the two electrodes is necessary in order to avoid the electrical short between them in the switch actuated position [79]. As soon as a voltage drop is applied between the two electrodes, charges are injected from the bottom actuation pad within the above oxide layer. Moreover, when the pull-in is reached, charges are injected also from the moveable membrane into the oxide as they come into contact after the collapse. Very often, the amount of entrapped charge is significant enough to generate a spurious effective bias, between the plate and the underlying electrode, larger than the release (pull-out voltage) [79], thus causing the switch to remain in the ON state even when the actual controlling voltage drops to zero (i.e. stiction). This physical phenomenon has been extensively studied by Papaioannou et Al., highlighting that the insulator charging depends on several factors, like the direct injection of charges due to the contact with polarized electrodes, and the dipoles orientation when the insulating layers in subjected to an electric field [80]. More importantly, Papaioannou has also studied the dependence of the charging/discharging mechanism on the temperature [81, 82]. In particular, the discharging time is expressed in [82] as follows:

$$t(T) = \tau_0 \, exp\left(\frac{E_A}{kT}\right) \tag{3.1}$$

where τ_0 and E_A are the characteristic time and the activation energy of the discharging process, respectively, T is the temperature and k is the Boltzmann constant. The inverse dependence of the discharging time on the temperature suggests that an increase of the insulator layer temperature would reduce the entrapped charge dispersion characteristic time, thus leading to a faster recovery of the normal MEMS switch operability. As it will be discussed more in details later, our active recovery mechanics is based upon the deployment of a high-resistivity serpentine underneath the insulating layer, acting as a heater when a current flows through it.

An additional source of stiction is the surface tension force generated by the liquid trapped underneath the movable component. Liquid accumulation usually takes place in either one of two cases: the samples were not properly dried after the fabrication process or poorly packaged device (i.e. not hermetic) operates in humid environment, indeed leading the contaminants flowing from the outside environment within the capped housing. The drops of condensate that are located under the cantilever (or bridge) may not only damp out the movement of this component, but also prevent any movement of the movable component.

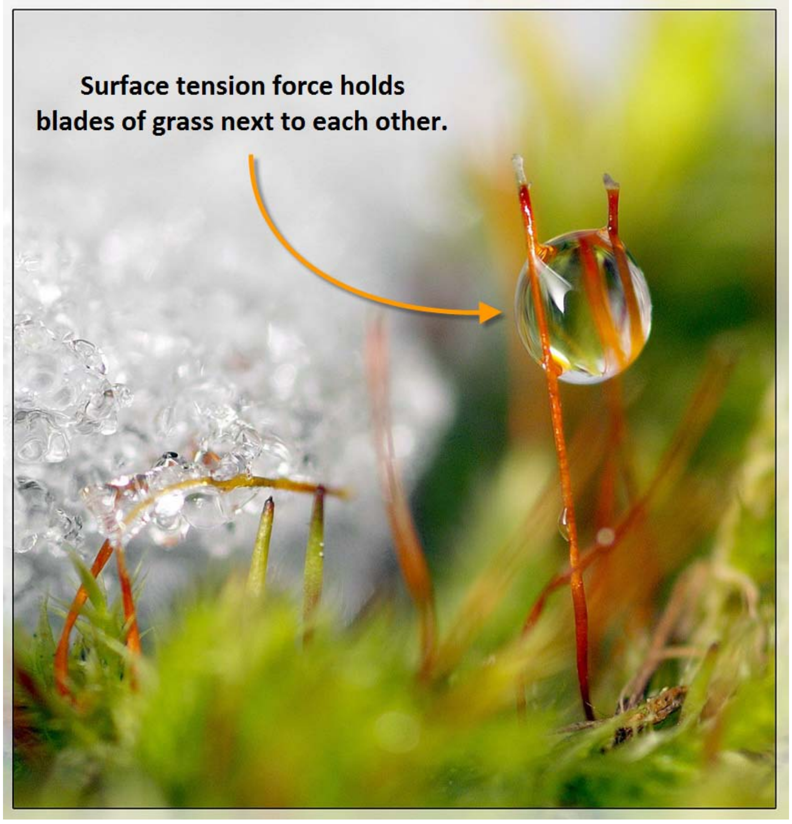

Figure 3.1: Surface tension force. Photographer Kovalevich A. From http://macroclub.ru.

The third source of adhesion is the van der Waals force. This force arises from the phenomenon of charge separation in the molecule. Such process starts only when two particles are in close proximity to each other. The separated charges in the molecule form a dipole (Figure 3.2a). The opposite charges of two dipoles are attracted towards each other forming thereby an attractive force between molecules (Figure 3.2b–3.2c).

The van der Waals force is very intense only in the very short distances between particles. The intensity of this force is proportional to the $1/\mathrm{r}^6$ [83], where r is the distance between the molecules.

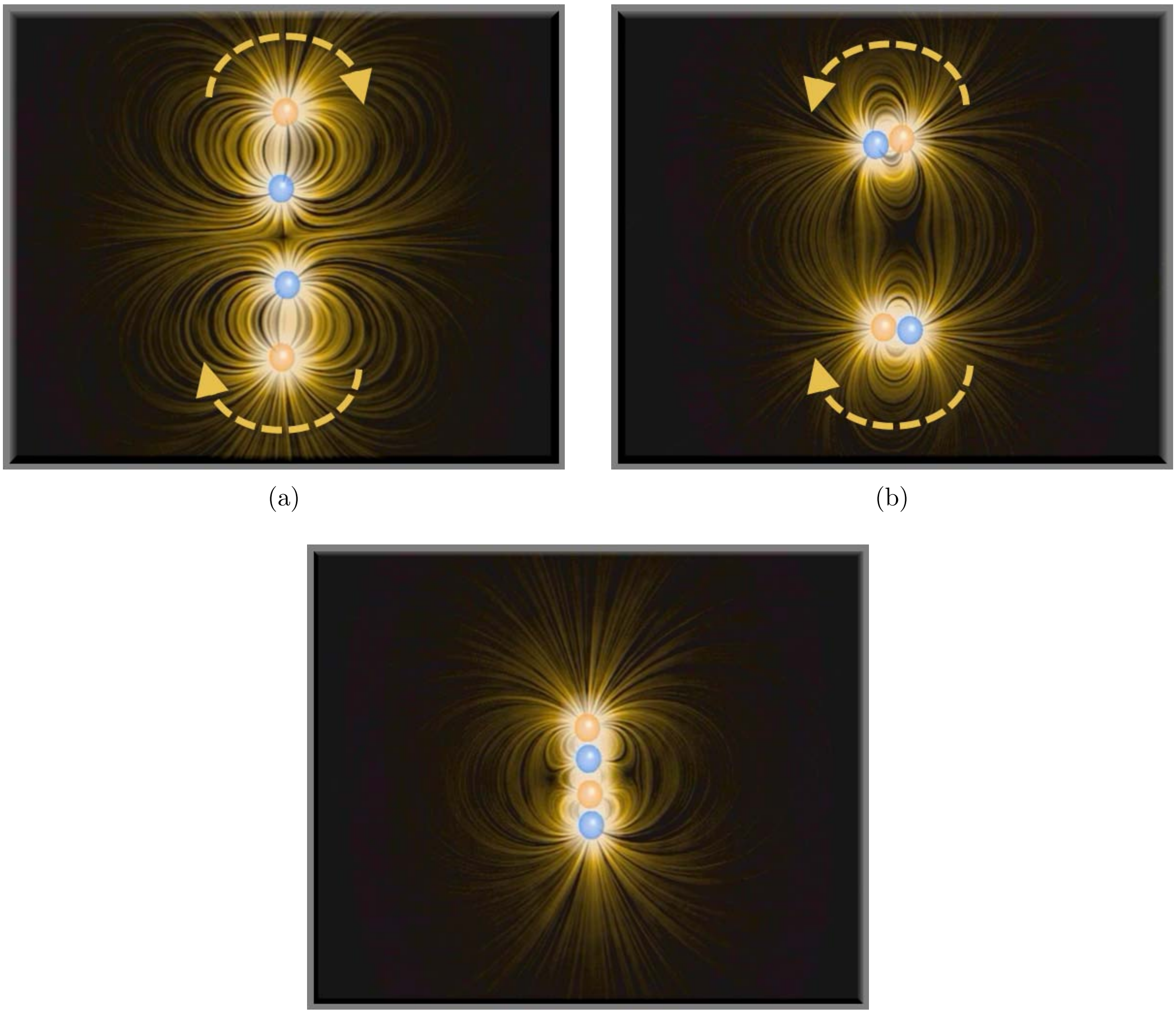

(a) (b) (c)

Figure 3.2: Formation of the adhesion between two molecules due to Van der Waals force. The pictures are taken from the lecture on Electrostatics at the site of MIT Department of Physics. `http://thebrain.mcgill.ca/flash/a/a_02/a_02_cr/a_02_cr_vis/a_02_cr_vis_3c.jpg`

Another important issue leading to stiction is the formation of micro-welding. This type of malfunctioning happens in ohmic MEMS switches when a low resistivity path between the input and the output is established in the device ON state (i.e. switch closed) [84]. The input/output signal, both in the RF and DC/AC domains, generates an electrical current flowing between the two ports of the micro-device. Because of the asperities of the surfaces where the ohmic contact is formed (in the ON state), the current concentrates in the spots where the peaks on the surfaces touch each other. This leads to large current densities, especially when the power of the signal is not small, causing the formation of micro-welding points between the metal of the suspended MEMS switch and of the fixed ohmic contacts [85]. Differently from the charge accumulation, that after a relatively long time leads again to the operability of the MEMS device, micro-welding points very likely lead to a fatal failure of the switch functioning, unless an active restoring mechanism is available to this purpose.

3.2 Main Approaches to Counteract Stiction in RF-MEMS Devices

The stiction countermeasures fall into two main categories: the first one includes the solutions that are intended to prevent stiction of movable components of the device (passive solutions), while the second group consists of mechanisms specially designed to release the stuck mechanical parts (active solutions).

The preventive measures related to the first category can be taken for example at the design stage. Generally, the restoring force is proportional to the flexural stiffness of the structure. The flexural stiffness is defined by the dimensions of the considered component and the shape of its cross-section. For a clamped-clamped beam, which is the one of the most common representation of the movable component for MEMS (Figure 3.3), such relation is given by the formulas (3.2) and (3.3) [79]:

$$F = k(g_0 - g)^3 \tag{3.2}$$

with

$$k = \frac{32Ewt^3}{l^3} \tag{3.3}$$

where g_0 is the gap between the substrate and the suspended beam in the neutral position; g is the current gap; E is the Young's modulus of the beam material; t, w, l are thickness, width and length of the beam correspondingly.

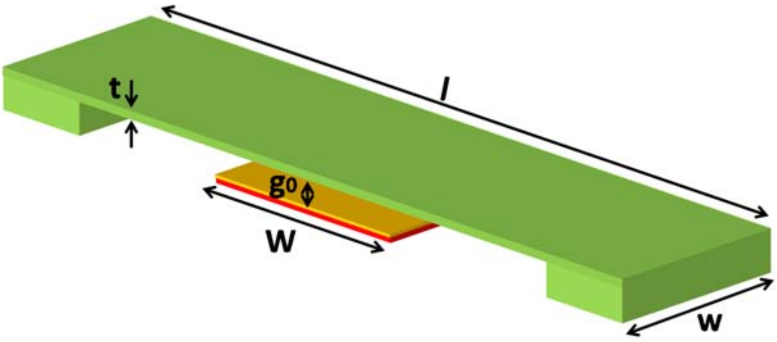

Figure 3.3: Example of a clamped-clamped beam.

From (3.2) and (3.3) it is evident that the restoring force of the beam can be increased by means of changing the geometrical parameters or selection the proper material for this component. Ideally, the shorter, the wider and the thicker is the beam, the larger is the restoring force. But such beam cannot be implemented. The problem is that very stiff structures require significant actuation voltage in order to be bent and controlled. This aspect is clear looking at the pull-in formula expressed as follows:

$$V_{\text{pull-in}} = \sqrt{\frac{8k{g_0}^3}{27\varepsilon_0 W w}} \tag{3.4}$$

where k is the spring constant of the beam, W and w is the thickness of the beam and the electrode, g_0 is the initial gap between the electrode and the beam.

Considering, for example, a beam with dimensions $100 \times 50 \times 10$ μm made of gold. By decreasing the length on just 1 μm and keeping all other parameters the same as original, the restoring force will be increased by 3%, whereas the actuation voltage will also increase by 1%. Thus, changes of geometry should be done carefully in order to keep a reasonable value for the actuation voltage.

Such consideration suggests the presence of several trade-offs in trying to match different requirements, like large restoring force, low actuation voltage, switching time and so on.

The forces responsible for adhesion are also proportional to the overall contact area between the movable component and the fixed structure. Basing on this concept, the probability of stiction failure can be decreased by reducing the contact area between two surfaces [71]. One of the suggested designs is shown in Figure 3.4. The substrate is realized in such a way that the overall contact area is the half in comparison to the original dimensions of the plate.

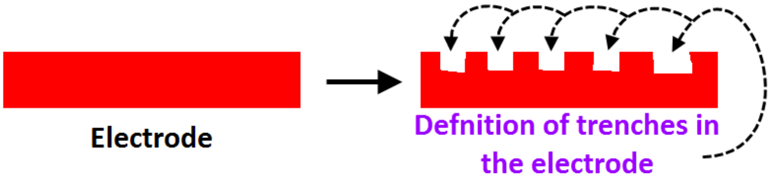

Figure 3.4: The reduction of the contact surface area that is achieved by means of definition the trenches in the layer forming the electrode.

Alternatively, the contact surface could be reduced by means of definition the openings in the central plate as it schematically shown on the Figure 3.5.

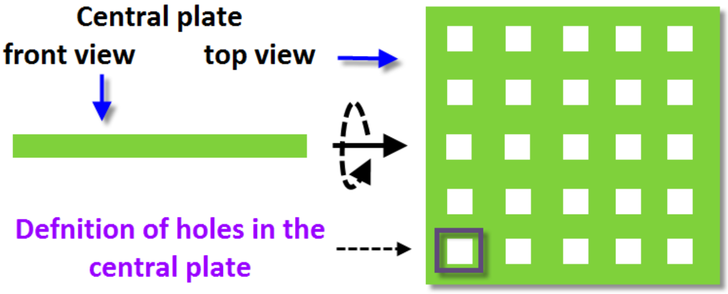

Figure 3.5: Another approach to reduce the contact surface area is in making opening in the central plate.

Apart from the optimization of geometrical parameters the engineers tried to investigate the adhesive properties of materials that are most commonly used in the manufacturing of movable component of MEMS structures. One of the early works has been done by Joachim Schimkat [86]. He compared the adhesive properties of gold (Au), gold-nickel alloy ($AuNi_5$) and rhodium (Rh). The experimental results have demonstrated that pure gold is not very suitable as a contact material for MEMS due to its high adhesion force.

One of the latest designs [87] suggests eliminating completely the contact between the suspended structure and the substrate (Figure 3.6). For this purpose the switch is designed as a comb drive with lateral direction of actuation. The switch is actuated when the plate and the electrode are on a very short distance from each other. In this case the capacitance value is vary high an the signal passing through the RF lines is isolated. The drawback of such kind of switch is that it requires considerable space on wafer and in the case of integration with other IC components, such peculiarity will enlarge the area required for the final chip.

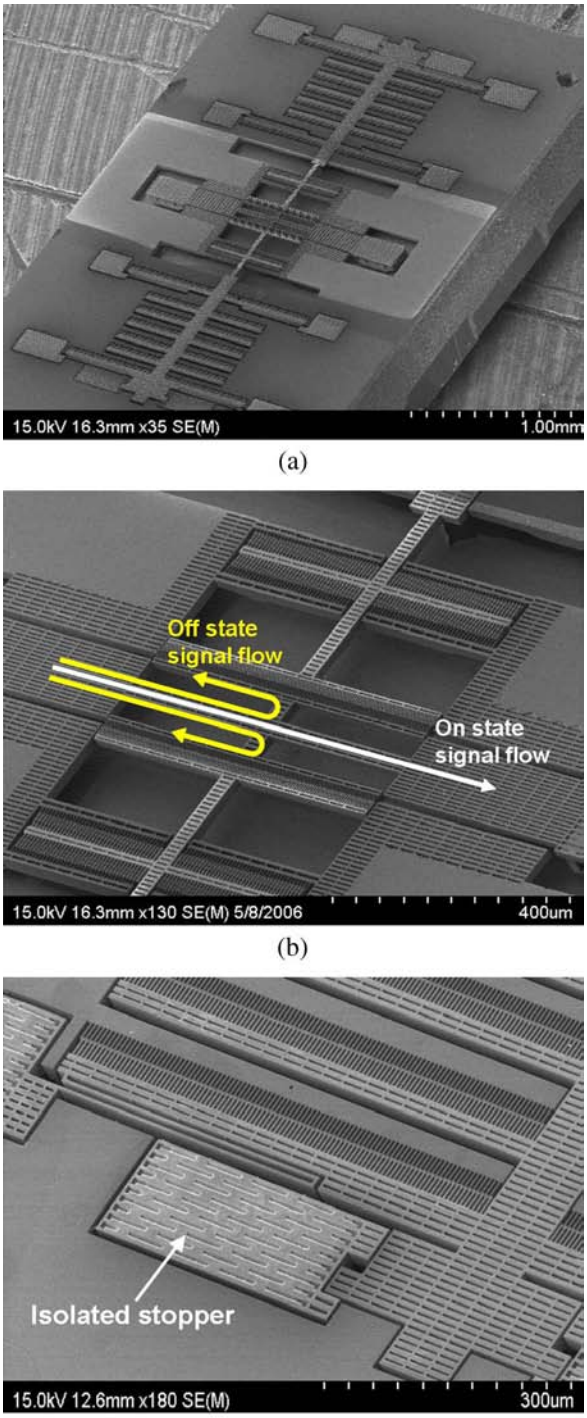

(a)

(b)

(c)

Figure 3.6: The non-contact type of switch proposed by Park et Al. for radar application.

One of the most efficient mechanisms invented to release the stuck membrane is the switch designed as so called toggle switch [73]. The design peculiarity of this type of switches is that along with actuation electrodes they also have the pull-out electrodes (Figure 3.7). Those additional electrodes when actuated, forces the plate to bend in the opposite direction (Figure 3.7c).

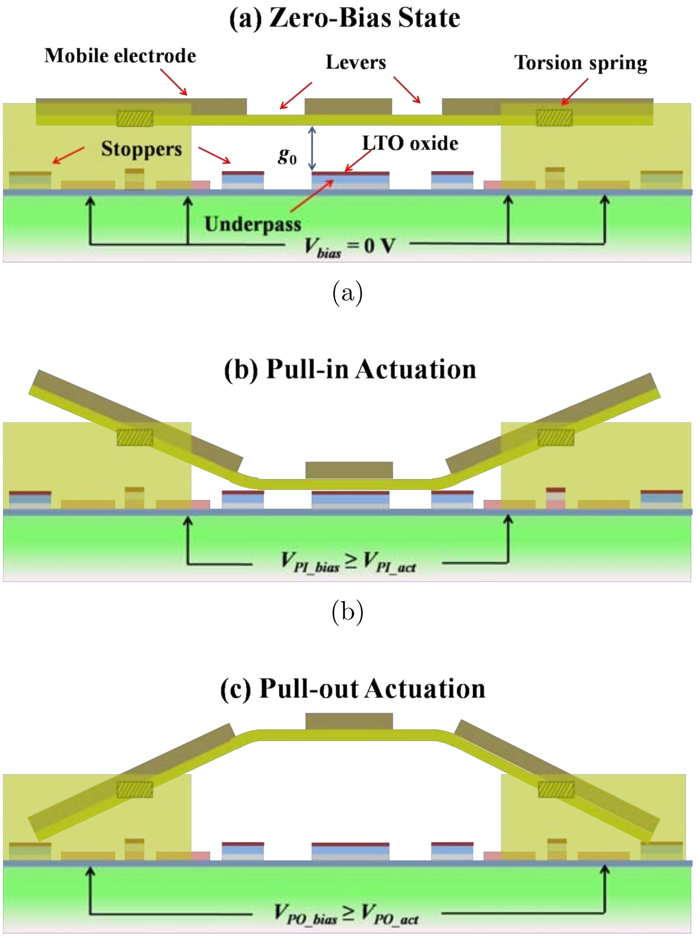

(a)

(b)

(c)

Figure 3.7: The illustration of the cross section of the toggle switch (a) in neutral (rest) position; (b) in pull-in state, when the actuation voltage is applied to the internal electrodes; and (c) the release of central plate, when the actuation voltage is applied to the external electrodes.

Another approach to minimize stiction effect has been suggested by H. Yamazaki et Al. [88]. The proposed to flip the bias voltage polarity depending on the amount of the pull-out voltage shift induced by the entrapped charge. By reversing the polarity of the applied bias, the entrapped charge is compensated by the injection of charge with the opposite polarity. If the pull-out voltage V_{PO} is larger than a given threshold value V_{th}, the polarity of the following actuation voltage will be reversed (Figure 3.8). This approach requires a rather complex measurement setup to be implemented within a laboratory. On the other hand, implementation of such an approach in a way that can be integrated with the MEMS devices themselves, would require the development of on-purpose control circuitry (e.g. ASIC and FPGA).

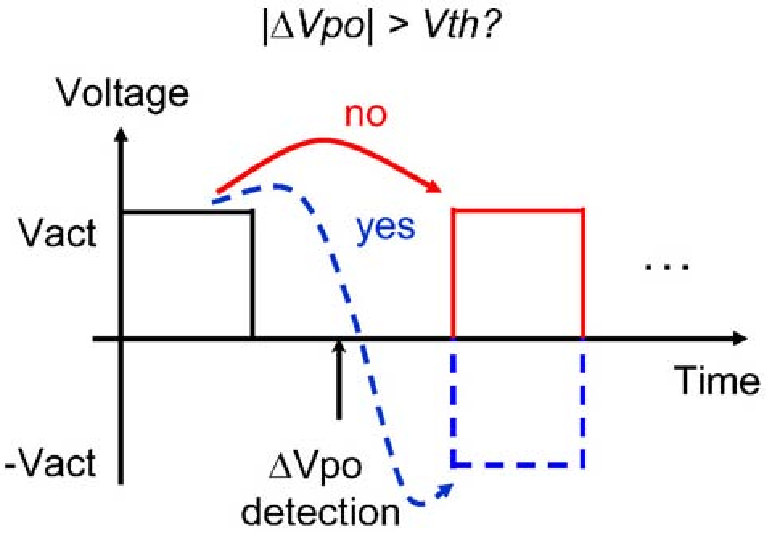

Figure 3.8: The actuation voltage waveform proposed in the work of Yamazaki et Al.

One more technique available only in the laboratory has been developed by Gupta et Al. [74] (Figure 3.9). In this approach, the back side of the wafer, which contains the samples of stuck cantilevers, was is exposed to a short time (order of nanosecond) laser pulse. The laser pulse generates mechanical vibrations that propagate through the wafer and provide to the stiction-failed cantilevers an additional mechanical energy large enough to release.

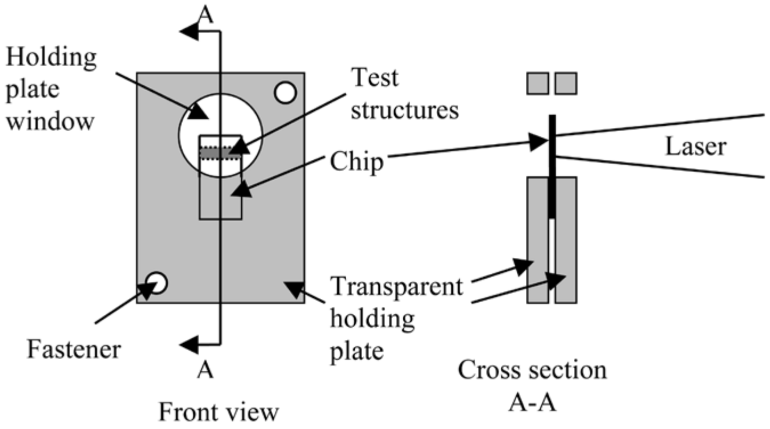

Figure 3.9: The schematics of the setup that has been used to release stuck cantilevers in the work of Gupta et Al.

Chapter 4

Heating Mechanism Theory

4.1 Heating Mechanism Description

Figure 4.1 shows a 3D schematic of the variable capacitor proposed in this work. This schematic has been generated starting from the 2D GDSII layout exploiting the 3D tool available within MEMSPRO™.

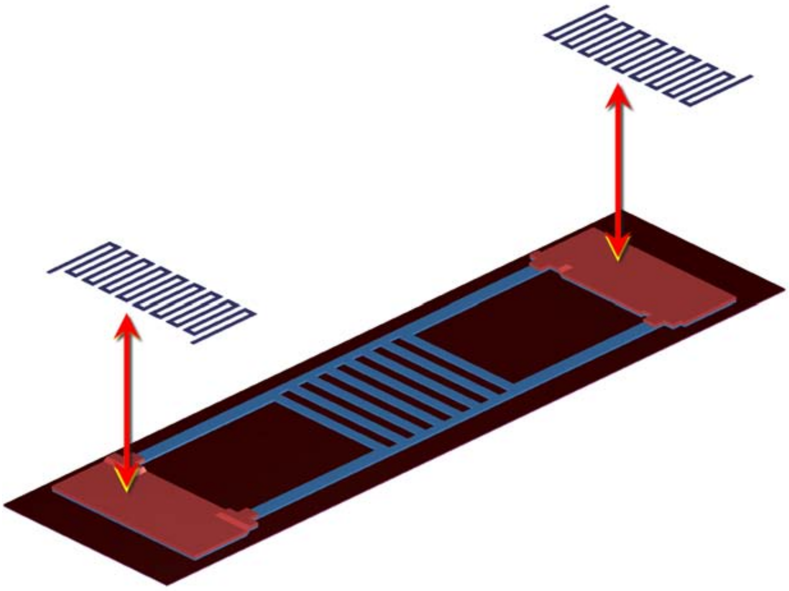

Figure 4.1: 3D schematic image of the RF-MEMS variable capacitor proposed in this work. The polysilicon serpentines, housed underneath the gold anchors,are shown in an exploded view.

The structure implements a variable capacitor based on a suspended gold membrane. Four straight flexible beams keep the central membrane suspended above the underlying electrode. When a bias is applied between the suspended and the underneath electrodes, the attractive force deforms the plate till reaching collapse (pull-in) onto the substrate. In the latter case the maximum capacitance value is reached. As it was mentioned before, stiction occurs when the electrostatic or molecular bonding forces, which attract the moving component of the switch to the electrode, exceed the restoring forces generated due to bending of supporting cantilevers. The active recovery mechanism is based on two highly resistive polysilicon serpentines (about 1500 Ω/sq) housed underneath the gold anchoring areas, where the straight suspensions are hinged, and electrically separated from the above gold by means of a silicon dioxide layer (Figure 4.1). Due to Joule heating effect the temperature of polysilicon would increase as a consequence of the current passing through it. At the same time, the layer of gold, deployed onto both heat sources, will raise its temperature and thereby it will expand in all directions, increasing the stress distributed within the device. Depending on the distribution of attractive forces, this stress would provide either shear or compressive force applied along the length of suspending beams. Moreover, the restoring force of bent cantilevers will also increase because of induced thermal stresses. As a result the bridge will be released and will turn back to its rest non-deformed position (Figure 4.2). The proposed recovery mechanism will be discussed more in details in the following sections and chapters, both concerning analytical and FEM modelling approaches.

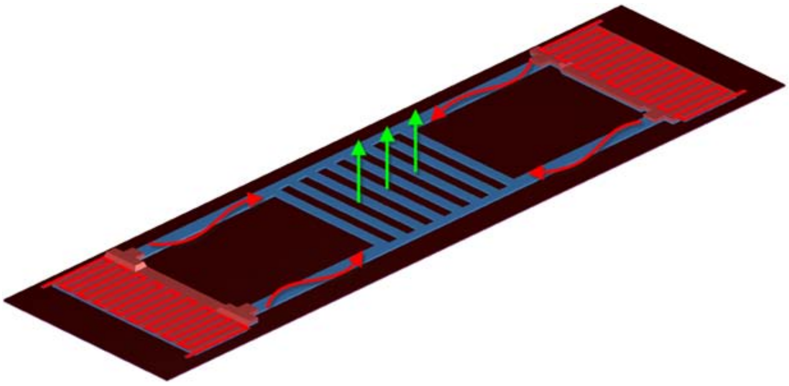

Figure 4.2: Recovery mechanism operating scheme. Expansion of beams is shown as well as the vertical restoring force acting on the central plate.

4.2 Mechanics

First of all, let us consider the stiffness of MEMS devices based on double-hinged suspended membranes (i.e. clamped-clamped). Typically electrostatic force, which is the main driving force in such devices, is evenly distributed on the electrodes surface. The main contribution of stiffness concerning the suspending beams is given by their bending along vertical direction. In this case the spring constant of one flexible beam is given by [79]:

$$k_{clamped-clamped\,beam} = \frac{32E\omega h^3}{L^3} \tag{4.1}$$

with

$$I = \frac{\omega h^3}{12} \tag{4.2}$$

where E is the Young's modulus, L, h and ω are the length, height and width of the suspension, and finally I is the moment of inertia for the beam (with a rectangular cross-section). By assuming a constant thickness of the suspension, fixed by technology constraints, the available DOF's (degrees of freedom) in order to modify its elastic behavior are L and ω. Given a certain longitudinal compressive force, if it exceeds a critical magnitude F_{crit}, the structure will start to bend. The bending will occur in the region where the cross-section is “weaker”, i.e. where it exhibits the minimum width and height across the length of the beam. In our mechanism the compression forces are represented by restoring forces of suspending beams. Due to the fact that beams are fixed on one end by the anchoring structure and on the other end by the stuck bridge, their bending radius will increase as response to the heat generated by the serpentine. The type of contribution (in-plane compressive or out-of-plane i.e. bending) induced by the expansion of these components depends on the position of an action line of their restoring force, or more precisely on the angle α between this line and the X axis, which is parallel to the substrate. This concept is schematically described in Figure 4.3 (bottom).

Prediction of α is not necessary in this application and, in addition, is quite problematic to be carried out as the angle may be defined only with a known distribution of the stiction forces across the central plate, residual stresses stored in suspended structures and non-idealities of suspended bridge geometrical parameters. If the along-X component of the total restoring force in larger than the Y one ($\alpha < 45°$) the central plate will experience compression Figure 4.4 (a), otherwise it will be deformed upward by suspensions Figure 4.4 (b).

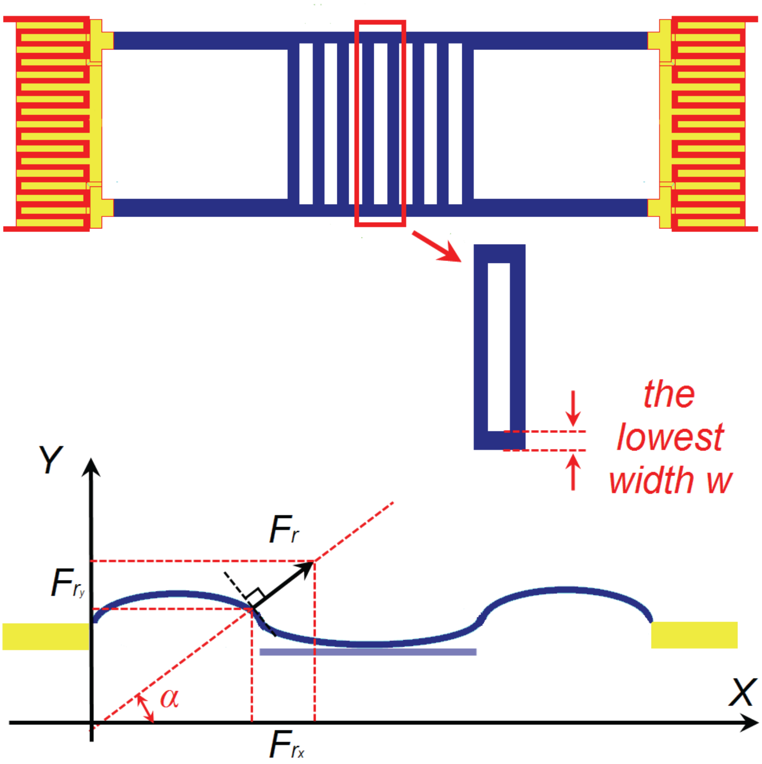

Figure 4.3: *Top*: Schematic top-view of the proposed device. Straight beam suspensions, central plate as well as polysilicon serpentines are visible. *Bottom*: Schematic cross-section of the variable capacitor in a possible deformed configuration after serpentines heating up.

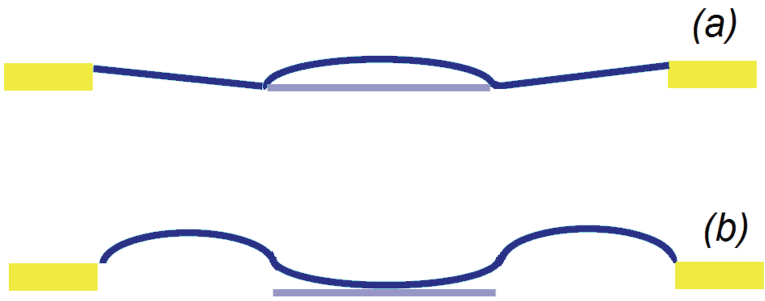

Figure 4.4: Two possible operation schemes for the active restoring mechanism proposed in this paper. (a): Straight beams compression induced by their heating leads to the arching of the central plate inducing a restoring force. (b): In case beams tend to bend upward, they will anyway induce a vertical force on the central (stuck) membrane.

In order to make the bridge more sensitive to the compressive loading and to minimize the area of possible stiction, the openings in the central plate (for sacrificial layer removal) have been designed as stripes instead of small holes. All of them are identical and uniformly distributed along the bridge length. Let us focus now on F_{crit}, which is the minimum compressive force that has to be applied to both sides (shear force) of the plate in order to bend it. Definition of its analytical expression requires quite complicated calculations because of the presence of empty regions. It is easier to approximate F_{crit} with a force for the solid plate with a larger value that may be found by means of formula (4.3), [89]:

$$F = 8.17\frac{\pi^2 D}{b} \tag{4.3}$$

with

$$D = \frac{Eh^3}{12(1-\mu^2)} \tag{4.4}$$

where b and h are the plate width and thickness respectively, while μ is the Poisson's ratio. Hence, if the bridge width is 150μm and its thickness is 1.8μm, as in our case, the required critical force is 8 mN, which can be reached by determining the proper temperature reached by heating serpentines (i.e. driving the correct amount of current through them).

Finally, we found the magnitude of restoring force, which also prevents or counteracts stiction. Its expression is the following one:

$$P = \frac{3EI}{L^3}\omega \tag{4.5}$$

where E is the gold Young's modulus, I the moment of inertia and is the required deflection of the structure. In this case, the latter one is equal to 3μm and represents the distance between the suspended bridge bottom face and the underlying surface (i.e. bottom electrode). The obtained result is varying from 0.5 to 0.75 μN (depending on the geometry of the plate). This formula also suggests keeping suspensions length as short as possible in order to achieve a larger restoring force. Nevertheless, it should be noted that this mechanical property strongly influences also the electrical and thermoelastic characteristics of the system, which will be discussed later. Finally, it is also possible estimating the magnitude of stiction force. Its minimum value should be large enough to keep the bridge stuck onto the underlying contact surface even when no bias voltage is applied. In other words, the numerical value of this force may be considered as the force applied on the central membrane to keep it down, consequently counteracting the restoring force of the flexible suspensions (which means larger or at least equal), which is equals to the sum of the restoring forces of each cantilever, i.e. 4 P.

4.3 Thermoelasticity

As it is known, the current passing through a resistive material causes its heating, which can be calculated as follows:

$$Q = I^2 Rt \tag{4.6}$$

where Q is the amount of released heat, I is the current driven through a resistance R for a certain amount of time t. In other words, in order to increase the temperature of the 1.5 kΩ/sq polysilicon serpentine up to 100°C for 1 sec, it is necessary to apply a current of 1.3 μA. The generated heat will quickly diffuse through the above gold layer due to its high coefficient of thermal conductivity. Thermal field will not be uniform because, as the heat diffuses through the gold, part of it will be lost in the exchange with the surrounding cooler air.

The Hooke's law accounting for thermal stresses is given by the following expressions:

$$\varepsilon_x = \frac{1}{E}[\sigma_x - \nu(\sigma_y + \sigma_z)] + \alpha T \tag{4.7a}$$

$$\varepsilon_y = \frac{1}{E}[\sigma_y - \nu(\sigma_x + \sigma_z)] + \alpha T \tag{4.7b}$$

$$\varepsilon_z = \frac{1}{E}[\sigma_z - \nu(\sigma_x + \sigma_y)] + \alpha T \tag{4.7c}$$

$$\gamma_{xy} = \frac{2(1+\nu)}{E}\tau_{xy} \tag{4.7d}$$

$$\gamma_{xz} = \frac{2(1+\nu)}{E}\tau_{xz} \tag{4.7e}$$

$$\gamma_{yz} = \frac{2(1+\nu)}{E}\tau_{yz} \tag{4.7f}$$

where ε_x, ε_y, ε_z, σ_{xy} , σ_{xz}, σ_{yz} are the normal and γ_{xy}, γ_{xz}, γ_{yz}, τ_{xy}, τ_{xz}, τ_{yz} are the shear components of strains and stresses respectively.

This means that thermal stresses increase normal strain components of the structure. The suspended part of the device, i.e. the bridge and supporting beams, has a length of 350μm. Ideally, with uniform heating of the structure, each variation of 100°C should result in enlarging of approximately 0.5μm in length. This value may be easily obtained from the thermal terms in (4.8), which defines the linear expansion coefficient β for any material:

$$\beta = \frac{\Delta L/L}{\Delta T} \tag{4.8}$$

where β is equal to 14,2$\times 10^{-6}$ K^{-1} for gold, L is the length of suspended structure (350 μm), the variation of temperature (in this case 100°C) and finally is the elongation. We did not consider any energy loss due to environment factors such as heat emission into the air.

4.4 Electrical Properties

The main effect in electrostatic transduction of MEMS devices is the pull-in. When a voltage is applied between the suspended membrane and the substrate, the attractive force starts bending the first one downward. For a critical voltage value the pull-in occurs, i.e. the collapse of the suspended part onto the substrate takes place. Its expression follows:

$$V_{\text{pull-in}} = \sqrt{\frac{8kg^3}{27\varepsilon_{air}WL}} \tag{4.9}$$

where g is the distance between the suspended plate and the underlying electrode, ε_{air} is the permittivity of air and W and L are the parallel plate transducer dimensions along X- and Y-axes. Equation (4.9) highlights a further constraint to be taken into account in designing of suspensions. Indeed, the shorter the beams are, the higher the pull-in voltage is, while it would be desirable to minimize it. This consideration shows the existence of a trade-off with the requirement of short beams discussed above in order to maximize the restoring force to recover stuck switches. This aspect should be carefully taken into account during the design phase. With the suspended part dimensions discussed here the pull-in voltage is around 25V.

Chapter 5

Fabrication and Devices Layout

5.1 Technology

The RF-MEMS technology available at Fondazione Bruno Kessler (FBK) relies on a surface micromachining process based on gold. High resistivity silicon wafers are employed as substrate and are covered by 1 μm thick field oxide. High resistivity polysilicon and TiN/Ti/Al/TiN/Ti multilayer are exploited for the DC biasing of suspended membranes and RF signal lines respectively (see Figure 5.1). An additional mask on the polysilicon layer enables the implantation of two dopant doses, leading to different sheet resistances for the same layer. Typically, a reduced dose is implanted on the polysilicon of the DC bias electrodes and lines (1500 Ω/sq) in order to reduce leakage currents and coupling with RF signals.

Differently, highly doped poly-silicon (30-300 Ω/sq) is used to obtain calibrated resistors. Both conductive layers (poly-silicon and multi-metal) are covered by silicon oxide, enabling the realization of metal insulator metal (MIM) capacitors as well as ohmic contact where vias are defined. The surface metallization consists of a 1.8 μm electroplated gold layer and the air-gaps are obtained wherever such a metal is deposited over a 3 μm sacrificial photoresist. In order to get stiffer gold membranes, for instance in correspondence with anchors, and suspended membranes that are meant not to deform, a second gold metallization (about 3 μm thick) is electroplated over the first one mentioned above. Wherever vias to the multi-metal are opened, a thin metal layer (150 nm of gold) is evaporated in order to get a gold to gold contact when the suspended membranes are actuated. Figure 5.1 reports a schematic cross section of the FBK technology taking as example a cantilever switch.

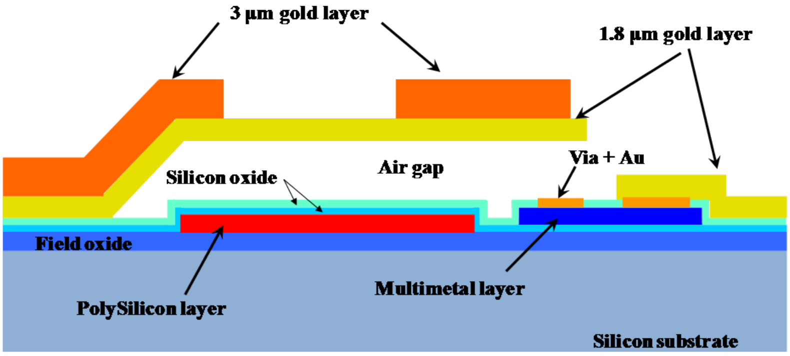

Figure 5.1: Schematic cross section of the FBK RF MEMS technology. A cantilever based suspended structure realizes an ohmic micro switch. Poly-silicon and multi-metal layers are visible together with the two gold metallisations (1.8 μm and 3 μm) for the suspended structure.

5.2 Devices Layout (Suspensions Heating)

The heating mechanism discussed in this thesis has been embedded in a few RF-MEMS switches geometries, both ohmic and capacitive. In this section, details about their layout and working principle are reported. The first layout we report on is an ohmic-series switch, and its layout is reported in Figure 5.2-left. It is based on a CPW (Coplanar WaveGuide) configuration. A central gold membrane is kept suspended by four flexible straight beams, over a poly-silicon actuation electrode, and over the input/output RF interrupted branches. Consequently, when the gold membrane is in its rest position, the switch is open (OFF state). The suspended gold membrane has to be DC grounded. When a bias is applied to the actuation pad, i.e. to the poly-silicon line and electrode, the electrostatic attractive force starts to move the suspended gold closer to the underlying electrode. When the bias reaches the pull-in value, the switch collapses onto the lower surface, indeed shorting the RF input to the output (switch ON). In Figure 5.2-right the gold layers have been removed in order to make visible the input/output RF branches as well as the poly-silicon. It shows also the poly-silicon serpentine-shaped heaters, that are placed underneath the gold anchoring areas, where the flexible beams are anchored. In each device, there are two serpentines that can be separately operated. Both the heaters and the biasing line and electrodes are made of poly-silicon. However, the heaters underwent the double Boron implantation (see the section about FBK technology), while the biasing line and electrode were masked during the second implant. As a result, the poly-silicon exploited the DC biasing of the suspended MEMS structure has a resistivity of about 1.5 kΩ/sq, indeed reducing the DC current leakage towards the silicon substrate. Moreover, being it highly-resistive, also the coupling between RF and DC signal is minimized, indeed resulting in smaller loss and impedance mismatch of the switch in the RF domain. Differently, the poly-silicon implementing the serpentines has a resistivity of 200-300 Ω/sq, suitable to obtain total a resistance in the range of 20-40 kΩ. This particular topology has an intrinsic issue that does not allow the switch to work properly in the RF domain when actuated (ON state). Indeed, the layout of Figure 5.2 derives from a capacitive shunt topology, in which the suspended membrane realizes a movable plate of the capacitor. Since the capacitance is to ground, there is a low-resistance path between the MEMS plate of the capacitor and the RF ground. Such path is realized in multi-metal and connects the gold of the suspended part to the CPW frame, and is visible nearby the serpentine. The series-ohmic version of this switch was obtained by adapting the layout of the shunt-capacitive one, i.e. interrupting the input/output RF line and opening vias in the oxide at the two branches, in order to obtain the resistive contacts. However, since by mistake the multi-metal path to ground, discussed above, was not replaced with an high-resistivity path, the RF signal founds a low-resistivity path to ground when the plate is actuated. Consequently, the switch behaves as an OPEN when the plate is not biased (OFF state), and as a SHORT when actuated (ON state). From the point of view of the RF performances the behavior of this sample is totally compromised by the design issue just discussed. However, the purpose in this thesis is to show the effectiveness and the working principle of the heating mechanism, and in this scenario the device meets such a need. As there is a noticeable difference in the S-parameters between the actuated and not actuated states, it is possible to detect the position of the central plate looking at the RF measurements.

More details of the switch are visible in the following figures. Figure 5.3-top reports the details of the heating serpentine, being the visualization of the above gold layer removed. Figure 5.3-bottom shows the input/output RF lines with the ohmic series contact underneath the (not visible) suspended gold plate. Moreover, the poly-silicon biasing central electrode is also visible. Figure 5.4, on the other hand, show only the gold metallizations. The suspended central membrane is visible. As it was mentioned in Chapter 4, in order to make the bridge more sensitive to the compressive loading and to minimize the area of possible stiction, the openings in the central plate have been designed as stripes. Figure 5.5 reports the layout of another sample in which the suspended MEMS structure is not based on a central plate with straight suspensions, but on a unique clamped-clamped membrane with perforations. Finally, Figure 5.6 shows an ohmic switch still based on a central plate with four straight suspending beams, where each of the four anchoring pads has an heater independently operable. In this way each beam can be suspended separately.

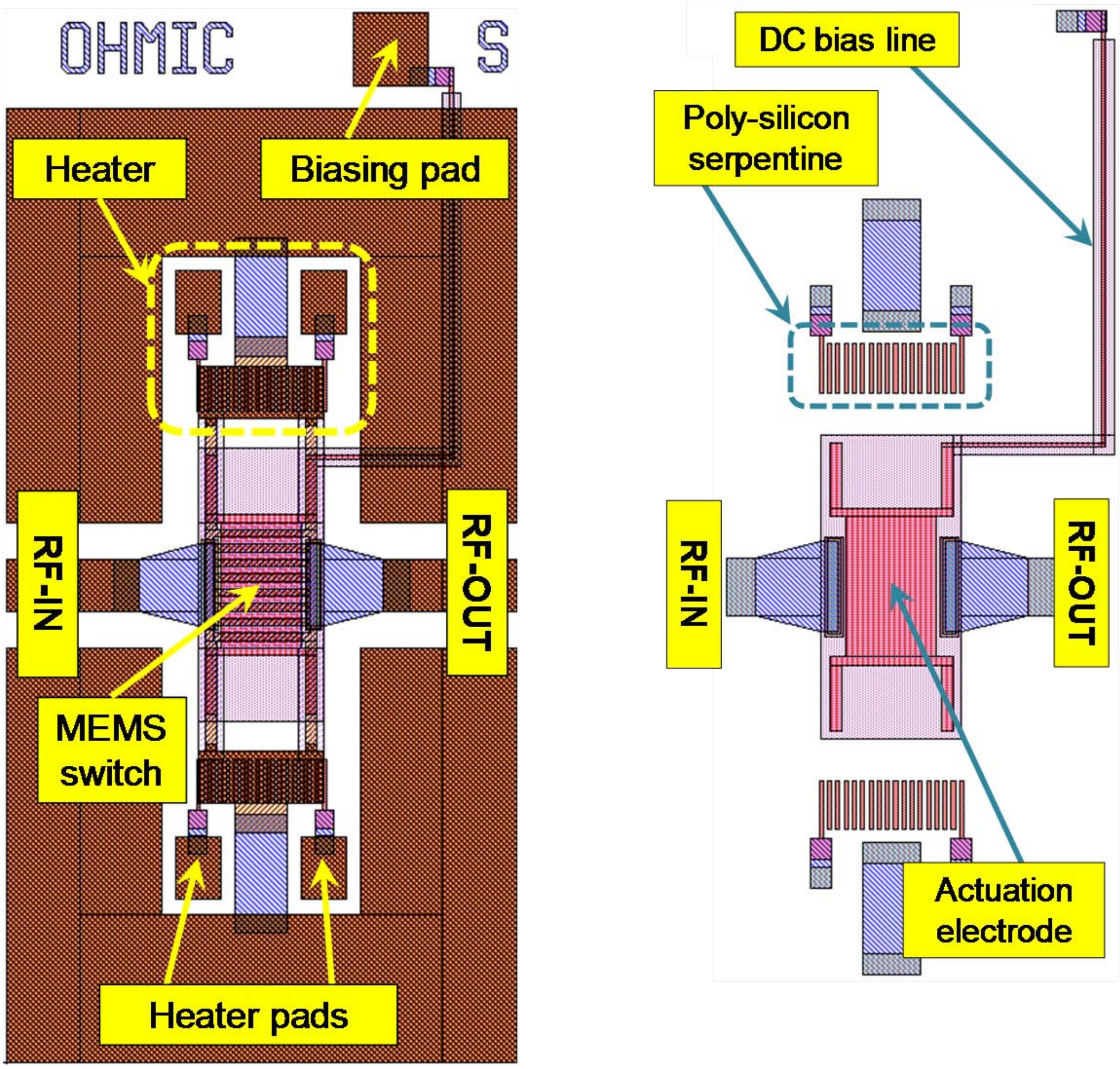

Figure 5.2: *Left.* Schematic of the proposed ohmic switch with two separate heaters underneath the gold anchoring areas. *Right.* Schematic of the same device in which the gold layer is made invisible, in order to highlight the poly-silicon serpentines and actuation electrode, as well as the input/output multi-metal RF lines.

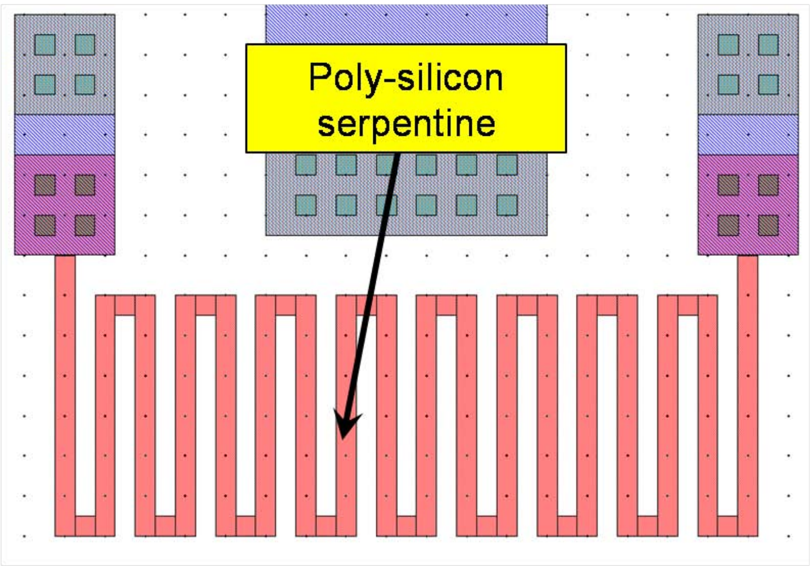

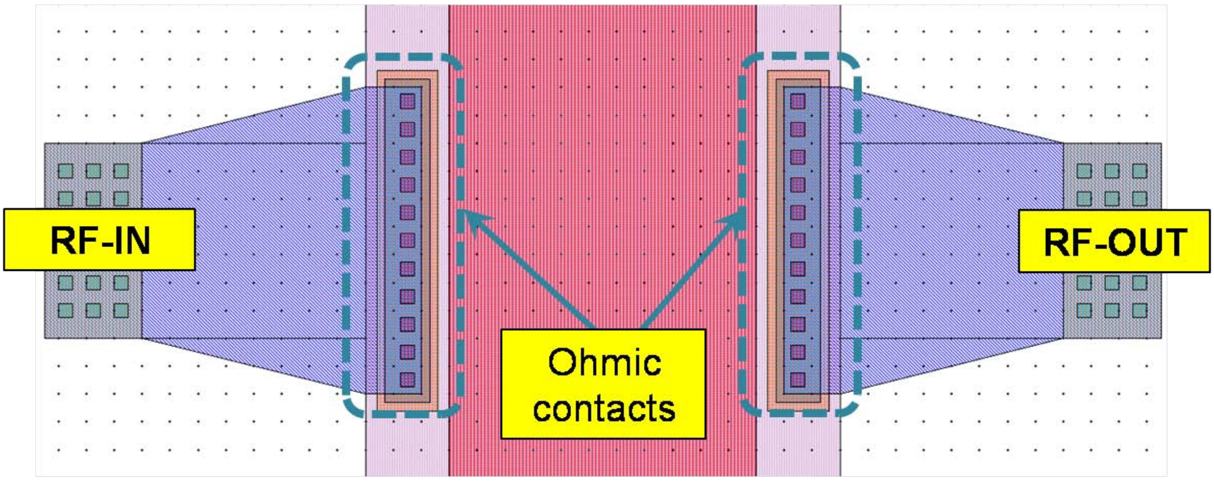

Figure 5.3: *Top*. Details of one poly-silicon serpentine heater. *Bottom*. Details of the input/output RF ohmic contacts.

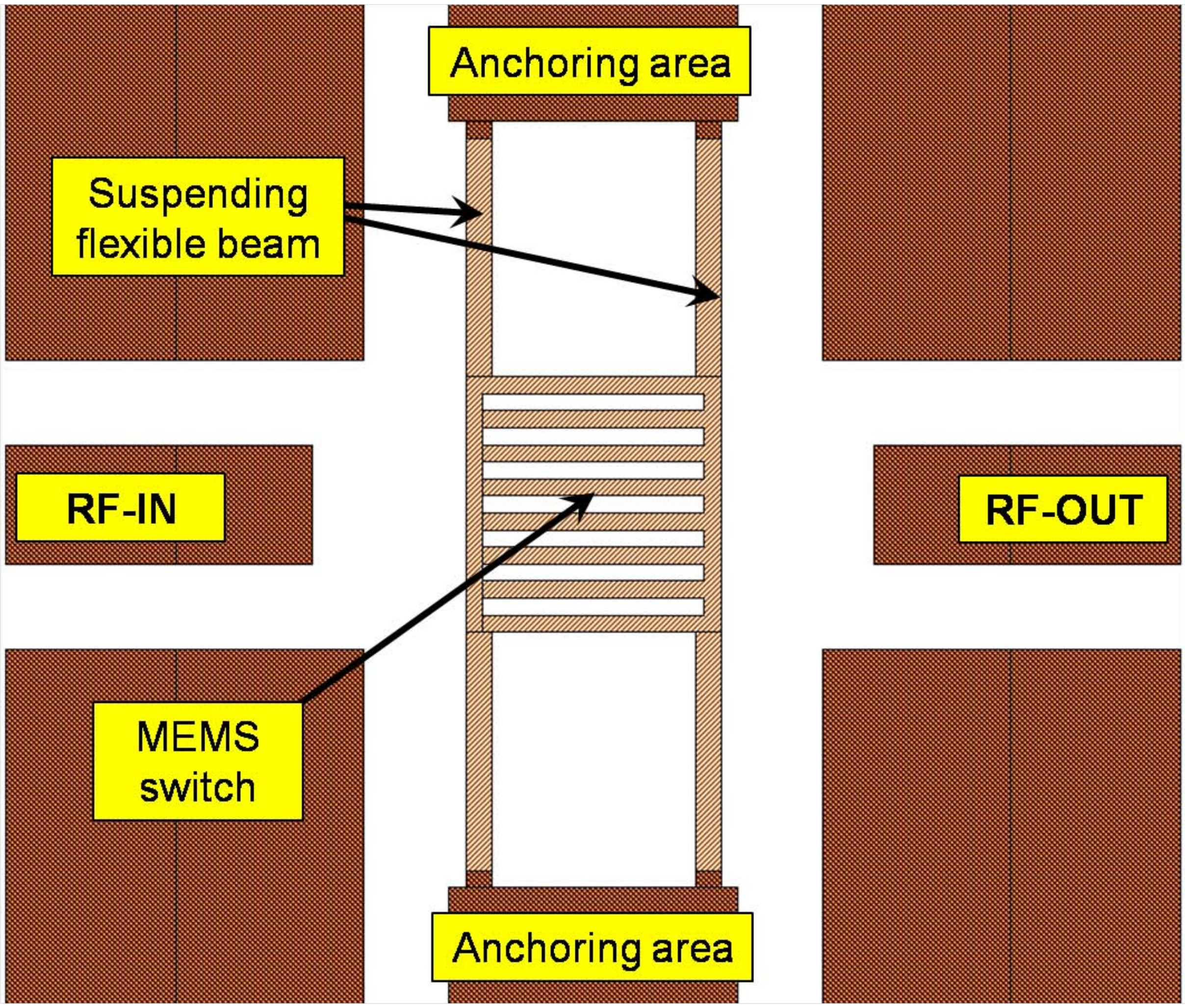

Figure 5.4: Layout of the structure where only the two gold metallizations are visible, indeed highlighting the suspended MEMS part as well as the surrounding CPW frame.

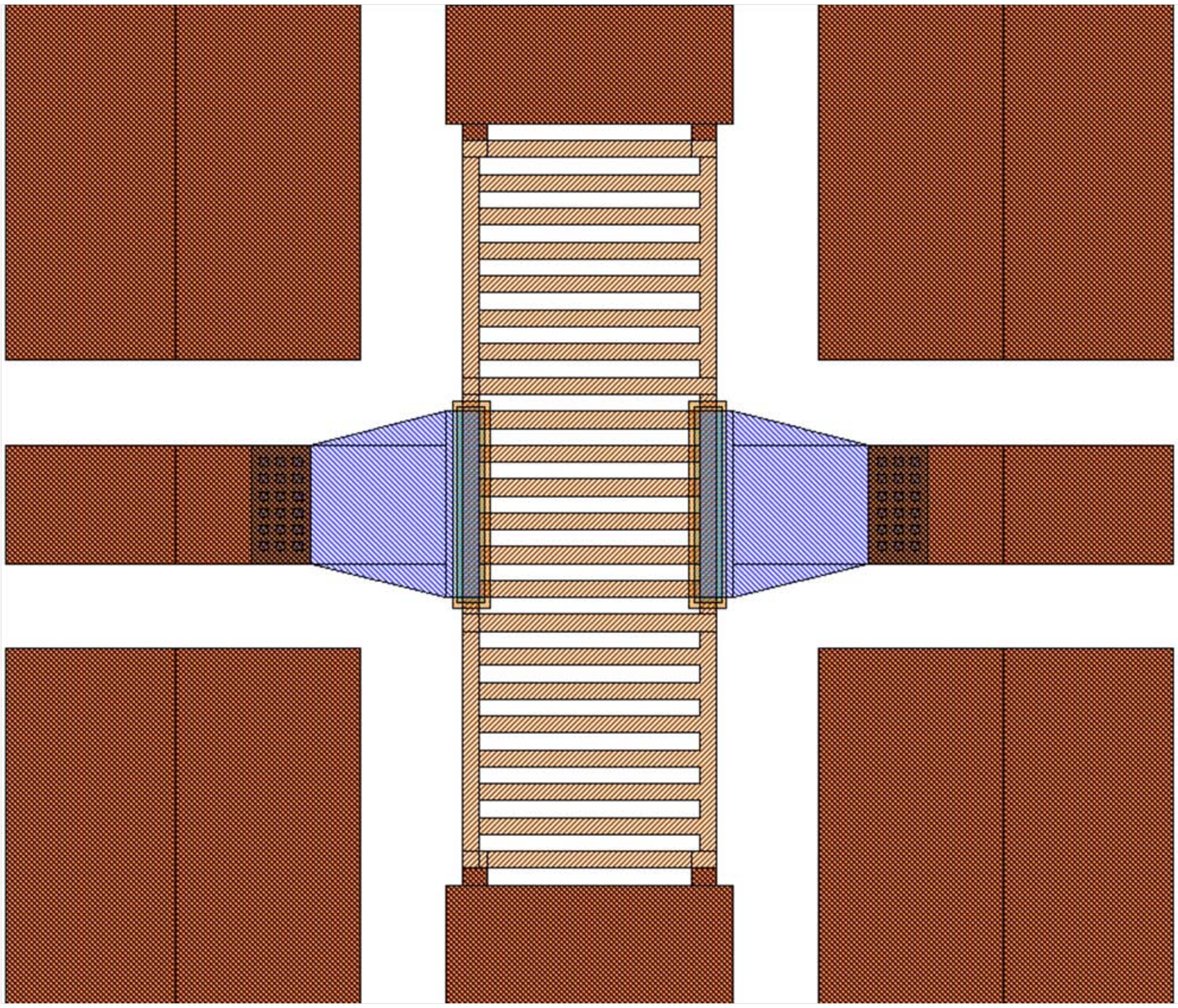

Figure 5.5: Modified device in which the suspended gold plate plus straight suspensions is replaced by a clamped-clamped membrane. The other layers, not visible here, including the heaters and the input/output RF lines, are the same as reported in previous figures.

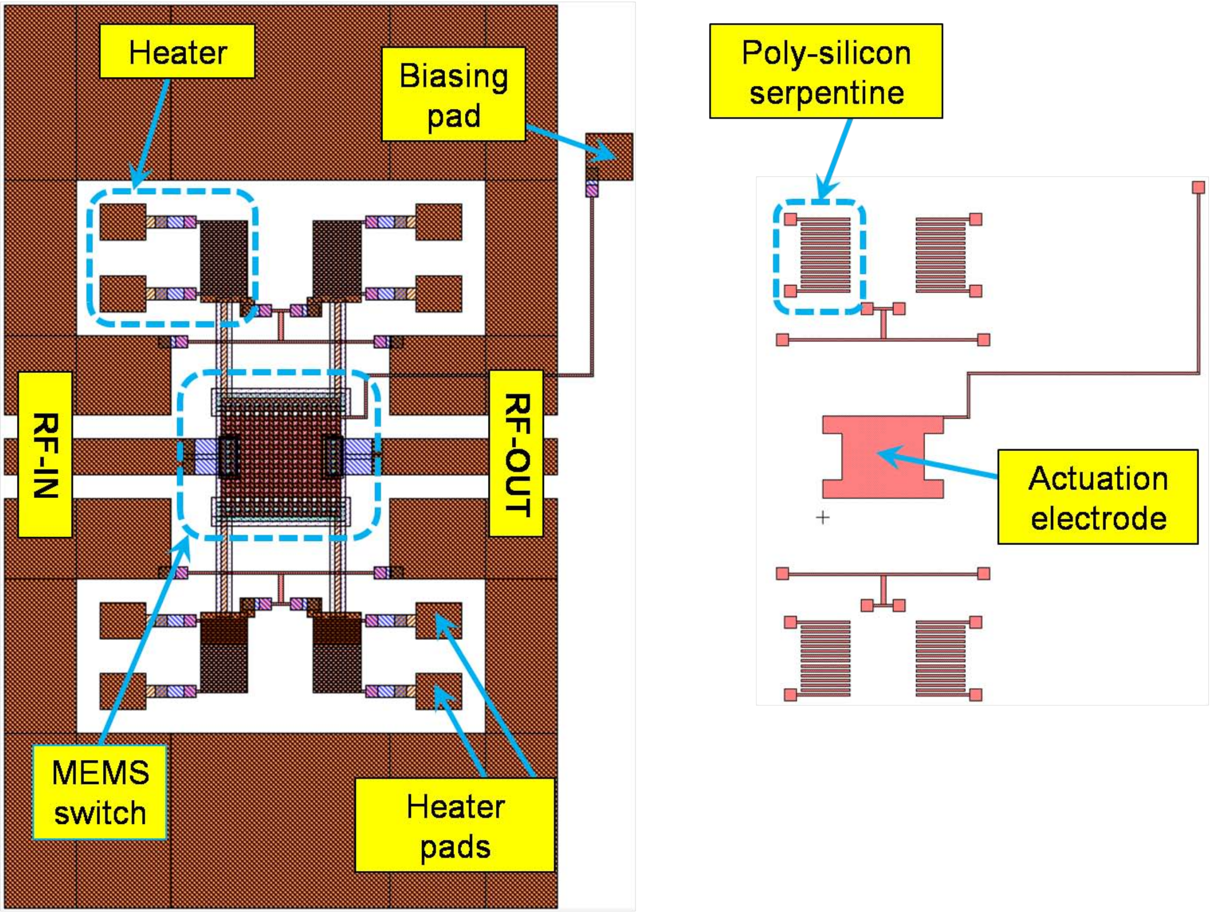

Figure 5.6: *Left*. Modified MEMS switch where four heaters (independently operable) are embedded underneath each straight beam gold anchoring area. *Right*. Details of the poly-silicon layer, realizing the heaters and the actuation electrode.

5.3 Central Plate Heating

We propose also a topology variation in which the heater is embedded in the actuation electrode (i.e. underneath the suspended plate) and not in the anchoring pad. In this case, the heat should help the release by speeding up the entrapped charge dispersion. The topology of the RF-MEMS switch we propose is reported in Figure 5.7-top. It is based on a central gold plate kept above the electrode by means of four folded flexible suspensions [16]. The device realizes a variable capacitor (varactor), i.e. no ohmic contact is established in both the actuated and not actuated states. The minimum capacitance is implemented when no bias is applied between the fixed and the moveable electrode, while the maximum value is reached when the plate pulls-in. Figure 5.7-bottom shows only the polysilicon layer realizing the actuation electrode and the serpentine for heating. By applying a bias to the pad connected to the electrode (labeled as "Biasing pad"in Figure 5.7) the normal operation of the MEMS varactor is ensured (pull-in/pull-out). Differently, when a voltage drop is applied between the two pads labeled as "Heating pad", a current is driven into the serpentine thus leading to its temperature increase due to the Joule effect. Heat diffusion to the silicon oxide layer, above the polysilicon, increases its temperature, thus decreasing the discharging time expressed by formula (3.1) and, consequently, the restoration of the switch operability after stiction occurs. Moreover, the heat also causes the expansion of the gold membrane when it is in contact with the oxide layer, as it happens in presence of stiction. Thermal expansion of gold introduces shear forces that might help in breaking the micro-welding points of an ohmic switch. Since the DUT (device under test) here discussed is capacitive, it is not possible to induce stiction because of large currents passing between the input and the output.

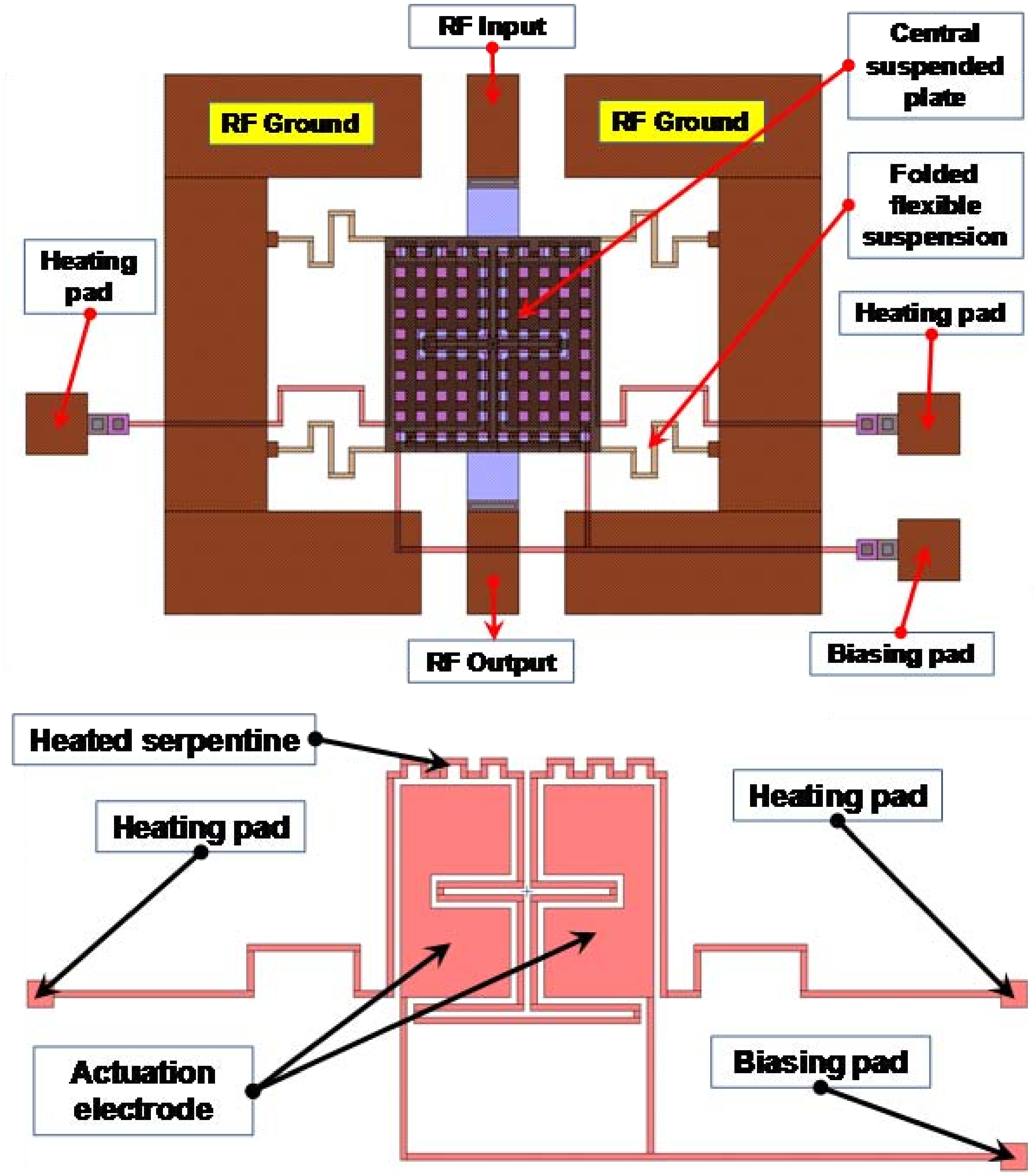

Figure 5.7: *Top-image.* Layout of the RF-MEMS varactor proposed in this work. It is based on a central gold plate connected to four flexible folded suspensions. *Bottom-image.* View of the polysilicon layer only highlighting the actuation pad scheme and the heating serpentine.

Chapter 6

FEM Simulations

The Finite Element Method (FEM) is a numerical technique suitable to obtain an approximate solution of complex physical problems. This method has been developed and described for the first time by Richard L. Courant in 1943 in the Bulletin of the American Mathematical Society [90], [91]. Originally, FEM has been used in mechanical applications, but since then the scope of application areas has been significantly enhanced, and nowadays the problems that can be analyzed by means of this method include dynamics of fluids, thermodynamics, acoustics, electromagnetism and so on. The period of noticeable improvements of FEM and its adaptation to different engineering disciplines falls in the 1980th. This phenomenon is related to the diffusion of personal computers that could provide larger computational capabilities.

Apart from the Finite Element Method, there are several different numerical techniques that allow to find approximate solution of certain physical problems with different levels of accuracy and complexity. Among them are, for instance, the Finite Difference Method (FDM), the Boundary Element Method (BEM) and the Finite Volume Method (FVM). Depending on the peculiarity of the problem each method has its advantages and disadvantages.

The main idea that lies behind the FEM is to consider any object as a set of sub elements connected to each other by means of nodes. Usually, the elements have a shape of triangles or squares for two dimensional problems, and prisms or tetrahedrons for the three dimensional objects. The behavior of each finite element is characterized by a set of mathematical functions describing the particular physical phenomenon (e.g. stiffness of material or propagation of electromagnetic signals) that can be either in the form of linear or higher-order polynomial expressions (depends on the geometry of the structure and on the particular phenomenon observed). The global solution is obtained by solving the above mentioned equations within each sub-element, according to the Boundary Conditions (BCs). The FEM is particularly suitable for the problems that involve models with complex or irregular topology. FEM has proven its efficiency in a variety of problems and at different levels of complexity.

The Finite Difference Method along with the Finite Element Method has been developed for solving linear and nonlinear differential equations governing engineering problems. These methods are reasonably simple in their formulation, and can be extended without significant difficulties to the 2D and 3D domains. As a general rule, such methods require less computational efforts. The main disadvantage of this technique is in its inefficiency in coping with the problems involving complex geometry. For the arbitrary shaped models it could be quite challenging to generate finite difference equations for the nodes next to the boundaries.

The Boundary Element Method is probably the simplest technique in terms of problem discretization. It deals only with the boundaries of the model and does not involve the internal region of the object. Thus, BEM drastically reduces the time required for the problem modeling and calculation efforts as well. The BEM is an integral-type numerical technique in which the integration of governing differential equation is followed by the numerical analysis.

Another example of numerical procedure to derive an approximate solution of complex engineering problems is the Finite Volume Method. It is as simple in formulation as FDM and as accurate at the regions of geometrical irregularity as FEM. As a result the computational efforts are larger than in FDM, but smaller than in FEM with the resulting accuracy comparable with FEM.

Summarizing details about each numerical method, it is clear that the FEM is the most suitable technique for the problem that involves the objects with complex geometry and requires coupling of different physical domains. Therefore FEM has been chosen as the main analytical method for studying the behavior of the test structures related to this work.

FEM analysis that is going to be discussed in this section has been performed in ANSYS™. Being it a multiphysical simulation tool, it is possible to couple different effects during the simulation flow. ANSYS, Inc has developed a wide range of analytical software applications that are dedicated to assist in carrying out analysis and obtaining accurate numerical solutions of complex physical problems.

All ANSYS products offer a solution on the basis of the Finite Element Method (FEM). Nowadays the Company has developed a wide range of software tools that cover a majority of physical domains. Among the them are Structural Mechanics Solutions Products (including ANSYS Mechanical, ANSYS Structural, etc.), Fluid Analysis Solutions Products (ANSYS CFD, ANSYS CFX,) etc.

6.1 Elements Used in the FEM Analysis

In this section, details on the use of ANSYS in order to simulate the RF-MEMS devices with heating mechanism discussed in this thesis are reported.

Several element types are available depending on the specific physical domains that need to be coupled. This particular problem requires that an element is suitable with 3D structures simulation and that it also allows to account for thermo-electro-mechanical effects.

To this purpose in the ANSYS element library the SOLID226 and SOLID227 elements are available, depending on the type of mesh and on the structure geometry to be studied [92]. SOLID226 has a brick shape with 20 nodes (one at each corner and one on each edge). Every node can be described by up to five degrees of freedom, such that the translations in the direction of three coordinate axis, temperature and voltage. This design allows the SOLID226 to be particularly suitable for the problems that account for the Joule heating effect. SOLID227 has similar properties, but is defined in the tetrahedral shape. Generally, tetrahedral elements are used to define an irregular mesh (and it is actually the only way to consider the model that has been imported from the geometry file generated by external compatible CAD tool). The possible drawback of irregular mesh is that it usually consists of more elements than the regular one, formed by the brick-shaped elements. This issue affects, firstly, the computation time. The second aspect is that the amount of elements forming the mesh is also critical from the PC capabilities point of view. During the computation procedure the processor stores all information related to the solution in RAM memory, it means that physical RAM memory, depending on its amount, could keep the data only for limited amount of nodes. When this amount is exceeded the PC automatically terminates the solution and the problem remains unsolvable, or swapping of data begins with the hard disk, leading to non-acceptable simulation time. The way out is to optimize mesh and to reduce the amount of nodes involved in the problem.

Another peculiarity of the analysis conducted in the ANSYS is related to the interaction of two physically separated components (surfaces or solids). Such objects may feel each other only if the contact elements are defined on their surfaces. The discussed problem involves the contact interaction between the suspended plate and underneath area. So, the contact is required to be additionally defined. For this purpose the CONTA174 and TARGE170 are the elements which represent the surface-to-surface contact between two rigid bodies and in the presented model they are created on the bottom side of the suspensions (CONTA174) and on the substrate underneath suspended beams (TARGE170).

6.2 Analysis Properties

The structural-thermoelectric analysis in ANSYS™requires specifying several material properties; among them are Young's modulus, Poisson's ratio, thermal conductivity, coefficient of thermal expansion, electrical resistivity etc. The complete list of materials and their properties are reported in Tables 6.1 - 6.4. The performed analysis takes into account large deflections of the model (the option *nlgeom=on* in the solution settings), while the reference temperature (temperature used for calculations of material expansion and convection) is 300 K (room temperature).

Table 6.1: The properties of the ***polysilicon*** material used in the ANSYS simulations.

Young's modulus, E [GPa]	175
Poisson's ratio, ν	0.36
Density, ρ_1 [kg/m^3]	2300
Resistance, ρ_2 [Ωm]	157.5×10^6
Thermal conductivity, k [W/mK]	150
Coefficient of linear thermal expansion , α [μm/mK]	2.9

Table 6.2: The properties of the ***silicon*** material used in the ANSYS simulations.

Young's modulus, E [GPa]	180
Poisson's ratio, ν	0.28
Density, ρ_1 [kg/m^3]	2330
Resistance, ρ_2 [Ωm]	2.3×10^3
Thermal conductivity, k [W/mK]	153
Coefficient of linear thermal expansion , α [μm/mK]	2.6
Specific heat, c [J/Kg °C)]	700

Table 6.3: The properties of the ***silicon oxide*** material used in the ANSYS simulations.

Young's modulus, E [GPa]	66
Poisson's ratio, ν	0.17
Density, ρ_1 [kg/m^3]	2650
Resistance, ρ_2 [Ωm]	10×10^{10}
Thermal conductivity, k [W/mK]	1.4
Coefficient of linear thermal expansion , α [μm/mK]	0.55
Specific heat, c [J/Kg °C)]	705.5

Table 6.4: The properties of the ***gold*** material used in the ANSYS simulations.

Young's modulus, E [GPa]	75
Poisson's ratio, ν	0.42
Density, ρ_1 [kg/m^3]	19300
Resistance, ρ_2 [Ωm]	2.44×10^{-8}
Thermal conductivity, k [W/mK]	315
Coefficient of linear thermal expansion , α [μm/mK]	14.2
Specific heat, c [J/Kg °C)]	130.5

The distribution of temperature due to Joule effect has been obtained by taking into account all possible ways of heat transfer, e.g. conduction, convection and radiation. The conduction of heat through the entire structure is considered by means of thermal conductivity coefficient k provided for each materials presented in the model (Tables 6.1 - 6.4). The heat loss q due to convection is determined by the boundary conditions that are specified on all the surfaces of the device. These BC's are provided by means of setting the film coefficient h, which indicates the rate of heat flow out of the solid. In this analysis film coefficient h has been calculated to each surface of the model and considered as temperature dependent (i.e. account for the temperature difference between the model and the environment). The top surfaces of the structure were considered as a heated horizontal plate, facing up (Figure 6.1), and h was obtained as film coefficient for natural convection from the surfaces with such type of orientation. The bottom surface was approximated with the case of a heated horizontal plate, facing down (Figure 6.1). Such approach is not very realistic, since in the real device the bottom surface will contact the material of the object on which this device is displaced. However, the advantage of such BC's is that even if the result will overestimate the real temperature of the device, it can serve as a maximum limit beyond which the temperature of the structure won't rise. Finally, the side surfaces were considered as the vertical walls within a laminar flow of air (Figure 6.1). An example of the film coefficients of each type is given in the Table 6.5.

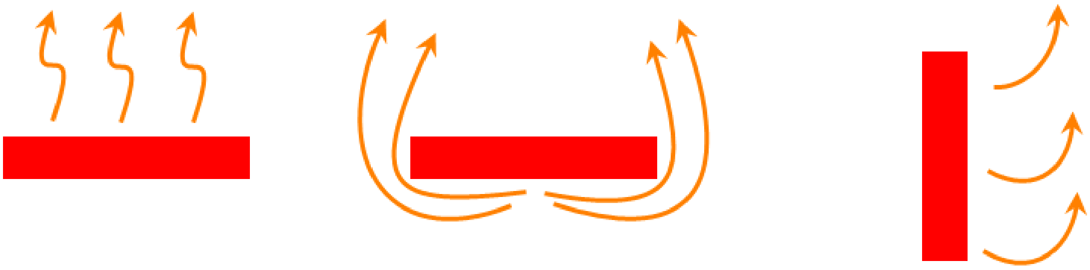

Figure 6.1: Different cases of convection accounted for in the simulation.

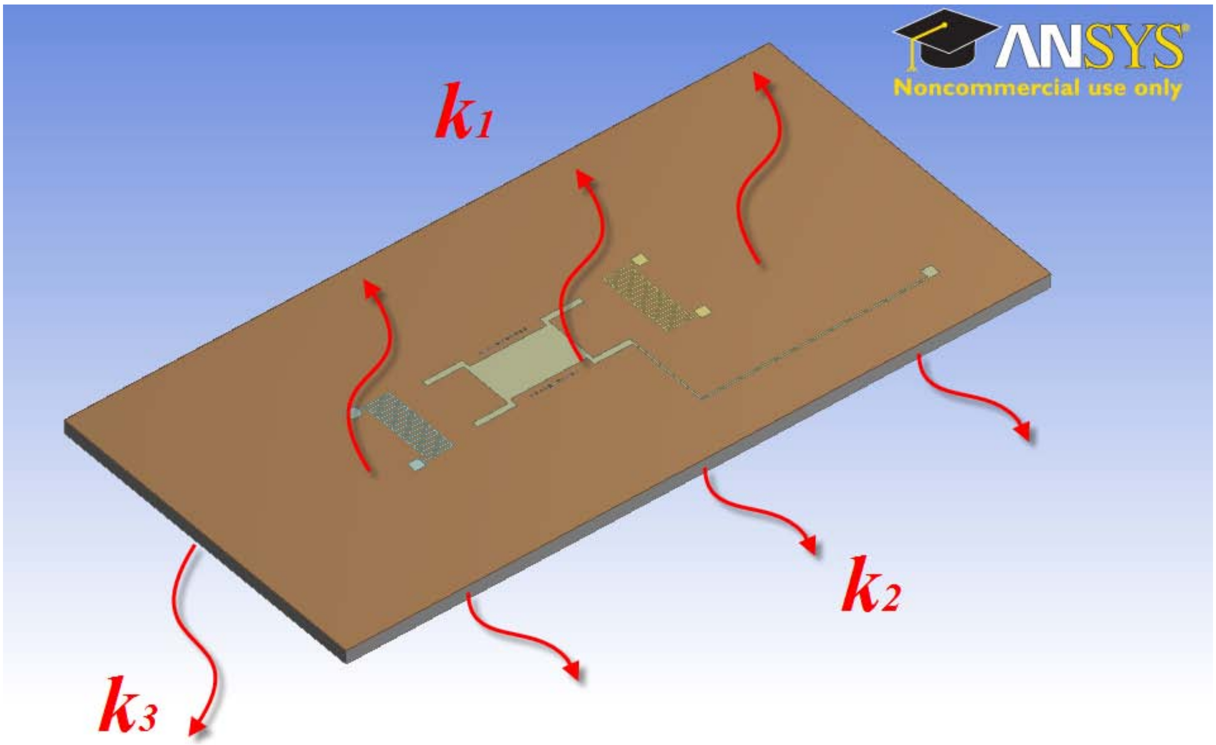

Figure 6.2: An example of convection BC defined by film coeficients through the up, side and bottom surfaces.

Table 6.5: The film coefficients *h* which define the convection BC through the top (*k1*), side (*k2*) and bottom (*k3*) surfaces related to the analysis of the structure from the Figure 6.9.

Temperature, K	k1	k2	k3
300	11.87	45.17	25.11
500	40.38	75.20	85.38
700	44.14	85.99	93.35
900	46.07	95.30	97.43
1100	47.27	103.8	99.96
1300	48.20	112.1	101.9
1500	48.96	120.4	103.5

The energy emitted by means of thermal radiation was also taken into account. The emissive power of the devices is characterized using the emissivity property of silicon, which is equal to 0.7 (i.e. effective emissivity of silicon, dimensionless quantity).

However, in the performed numerical analysis the non-ideal case (when the suspended parts of the microstructure experience intrinsic mechanical stress) haven't been considered.

6.3 The Results of FEM Analysis

6.3.1 Thermoelectric Coupled Effect

The first thing that has been investigated by means of FEM analysis is the heat induced by means of each serpentine into the die. The temperature distribution caused by different geometries of heater was considered as well. The meshed models of both serpentines are shown in Figure 6.3 and Figure 6.6 correspondingly. In these simulations each serpentine was embedded into the piece of silicon wafer that has a square shape with the side length of 12mm. The 50 V of DC voltage drop was applied across each serpentine in order to generate the Joule heating effect. The simulation results can be observed in the Figure 6.4 (magnified) and Figure 6.5 for the first test structure and in the Figure 6.7 (magnified) and Figure 6.8 for the second sample. Since the first serpentine is longer than the second one (and thus has higher resistivity), under the 50V bias it generates less heat than the shorter counterpart. The temperature of the first die rise up to approximately 310K, whereas the maximum temperature of the other structure reaches 319K.

6.3.2 Thermoelectromechanical Coupled Effect

In this simulation the switch is considered together with the surrounding piece of wafer that again has a square shape. The meshed model of the entire structure is shown in the Figure 6.9. In this case the serpentine has the second type topology (as in the Figure 6.6), which is actuated by means of 250 Volts of DC bias. Only one of the available heaters are biased in this analysis. The temperature of this structure rises up to 404K. From the Figures 6.10 and 6.11 it is clear that the expanded central plate goes upwards for several microns. Thus, this result proves the assumption that the generated heat induces the compression force which contributes to the releasing force.

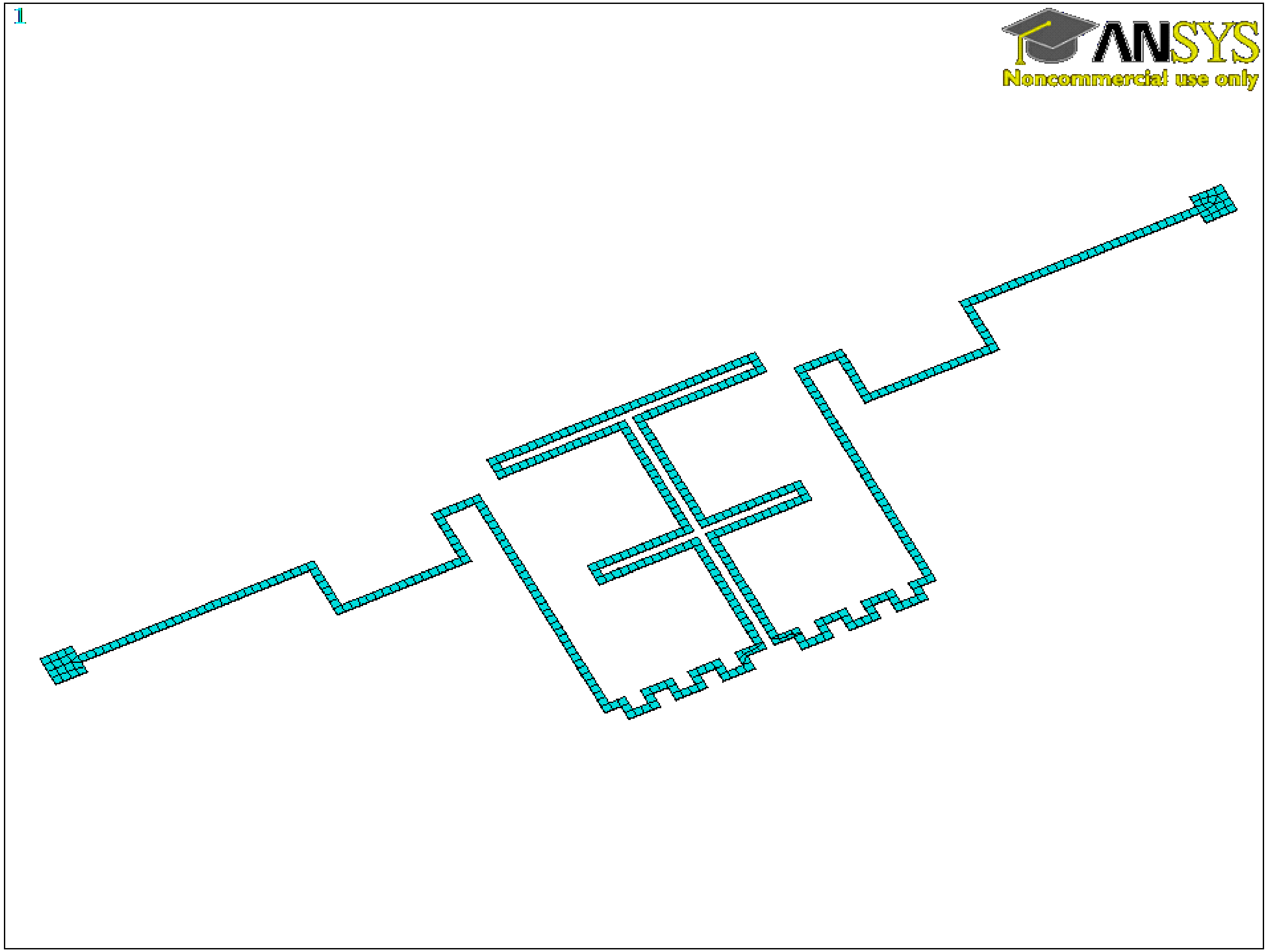

Figure 6.3: The meshed model of polysilicon serpentine designed for the RF-MEMS varactor (Figure 5.7)

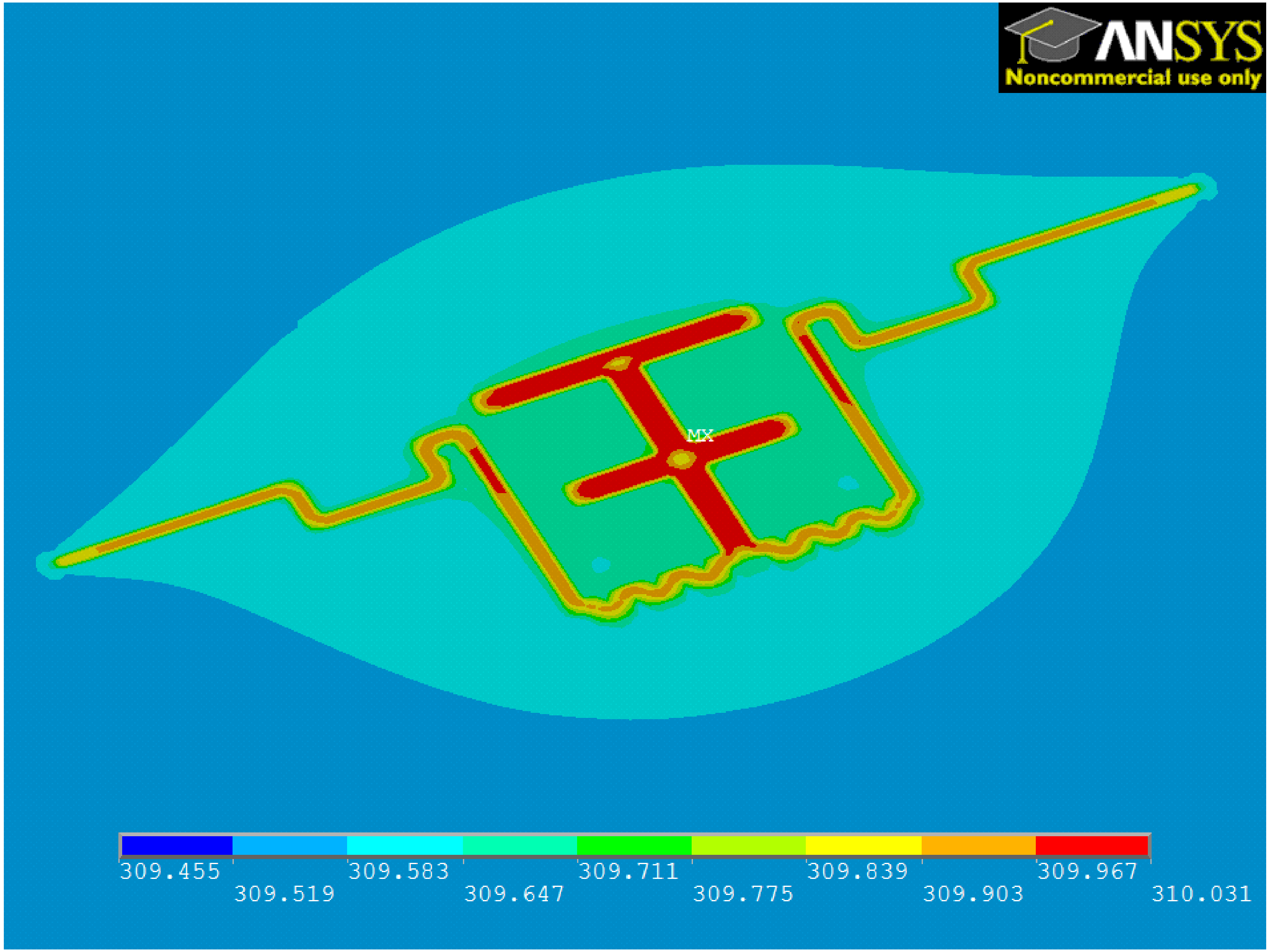

Figure 6.4: The magnified view of the temperature distribution in the silicon substrate due to the heat generated by polysilicon serpentine from the Figure 6.3

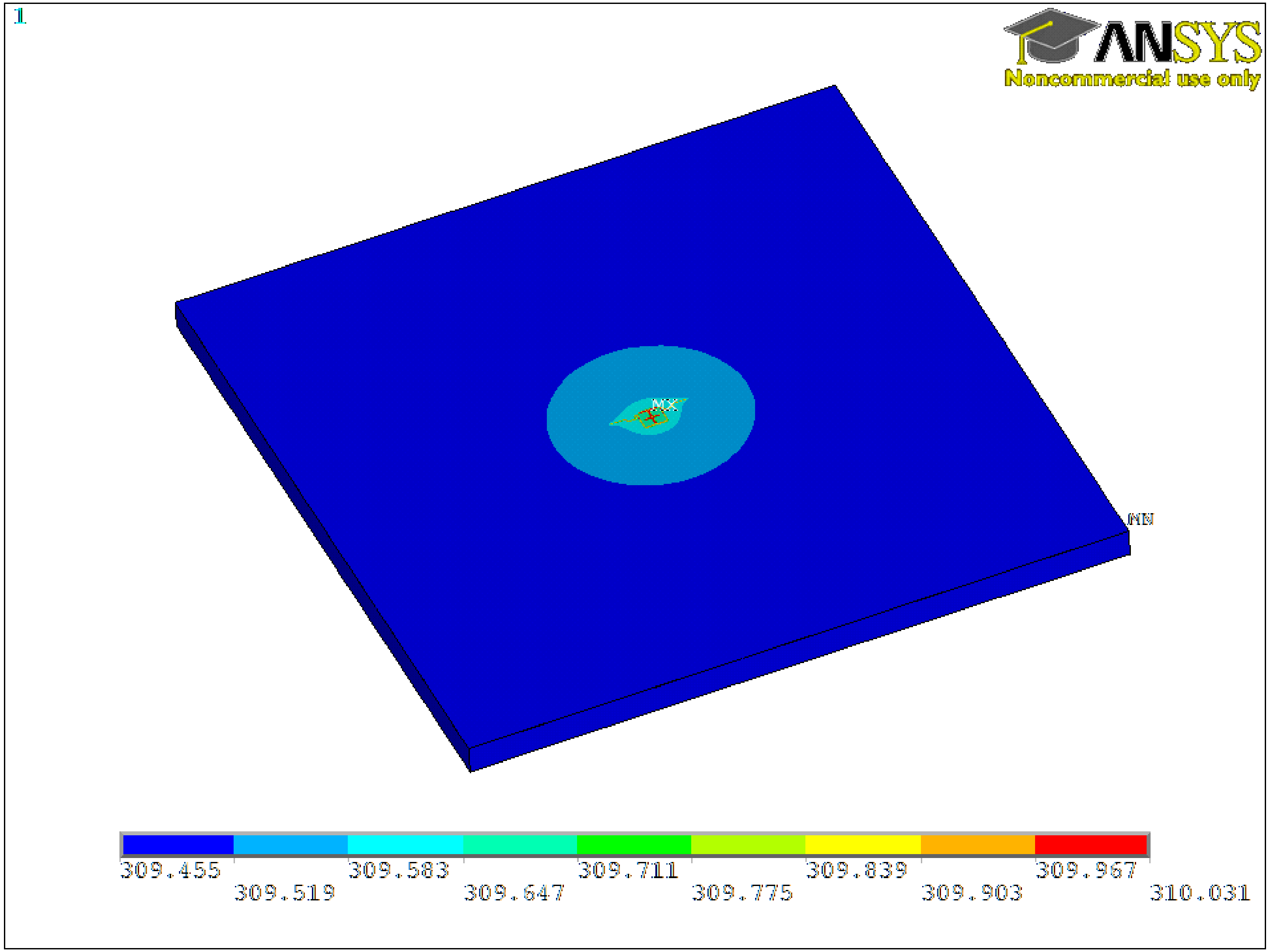

Figure 6.5: The temperature distribution in the silicon substrate due to the heat generated by polysilicon serpentine designed for the RF-MEMS varactor (Figure 5.7).

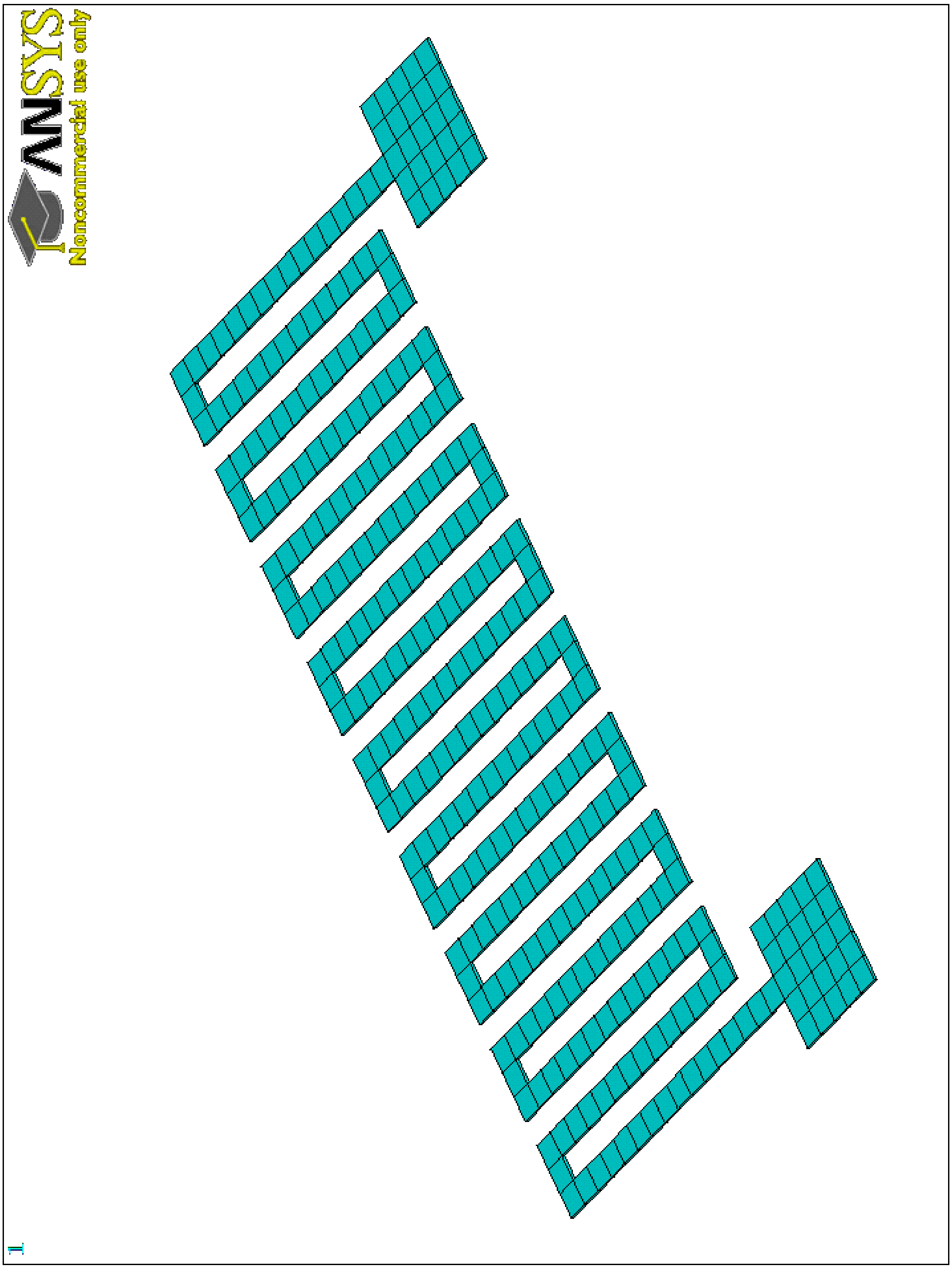

Figure 6.6: The meshed model of the polysilicon serpentine designed for the RF-MEMS ohmic switch (Figure 5.2)

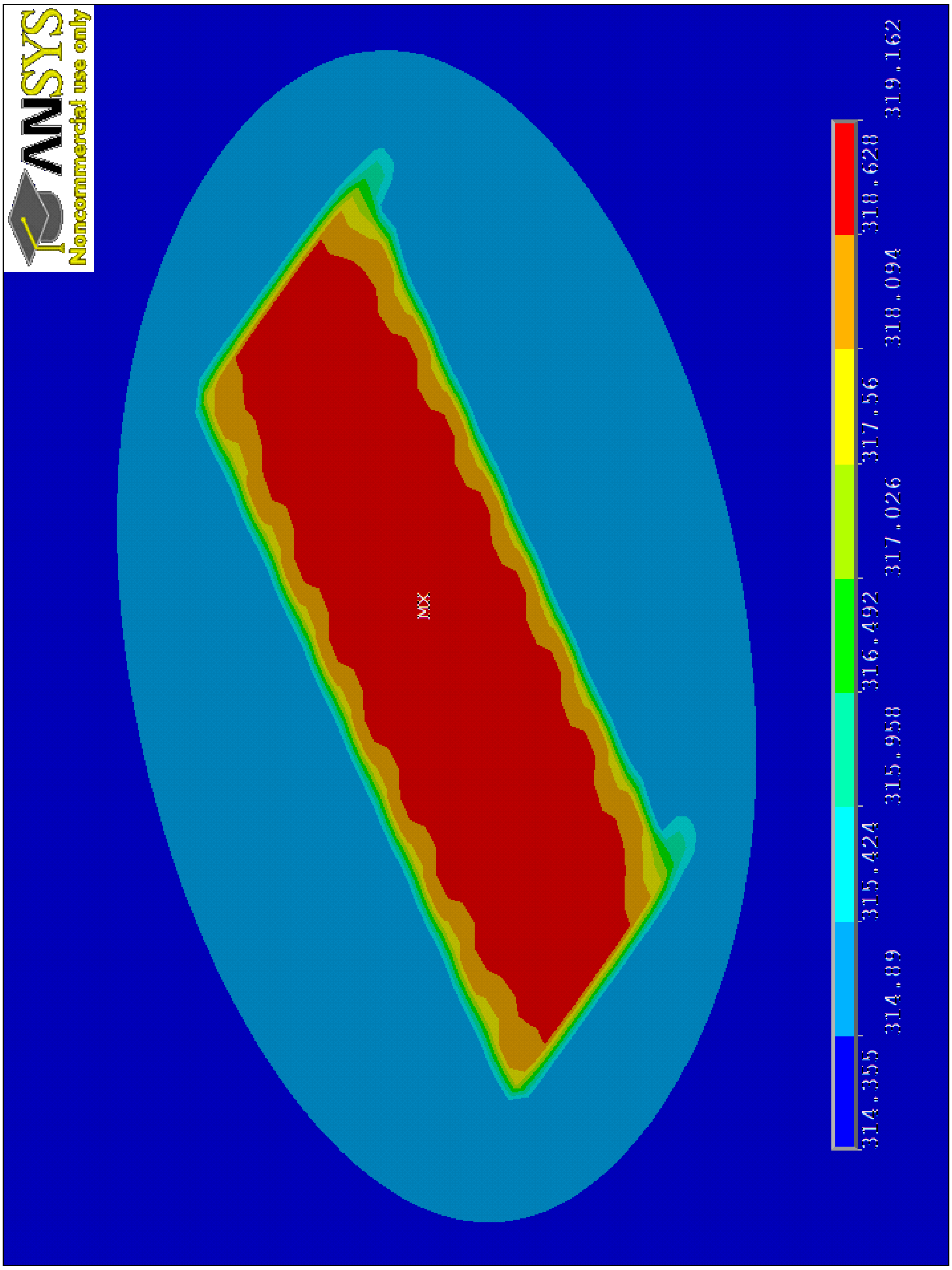

Figure 6.7: The magnified view of the temperature distribution in the silicon substrate due to the heat generated by polysilicon serpentine from the Figure 6.6

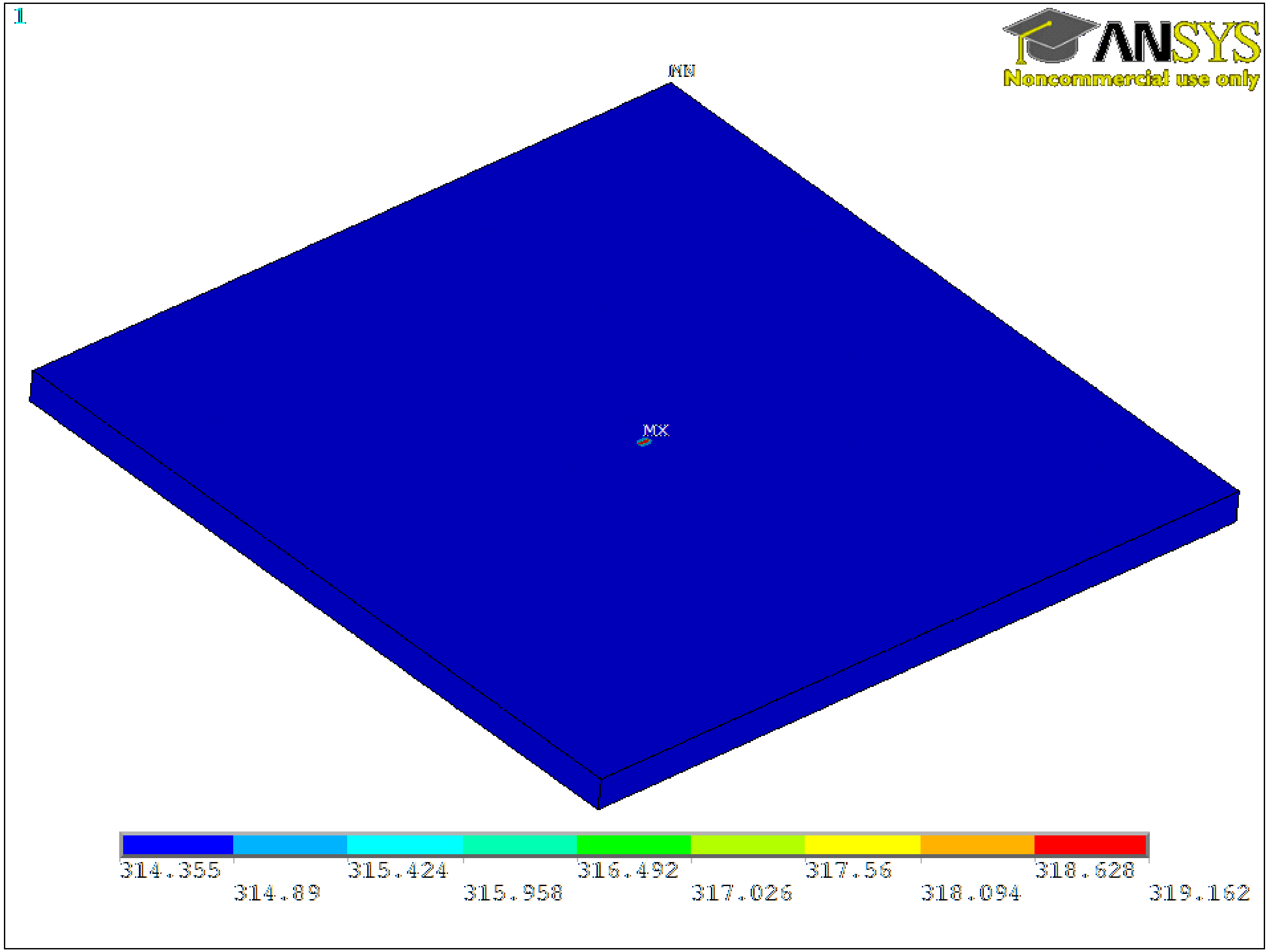

Figure 6.8: The temperature distribution in the silicon substrate due to the heat generated by polysilicon serpentine designed for the RF-MEMS ohmic switch (Figure 5.2).

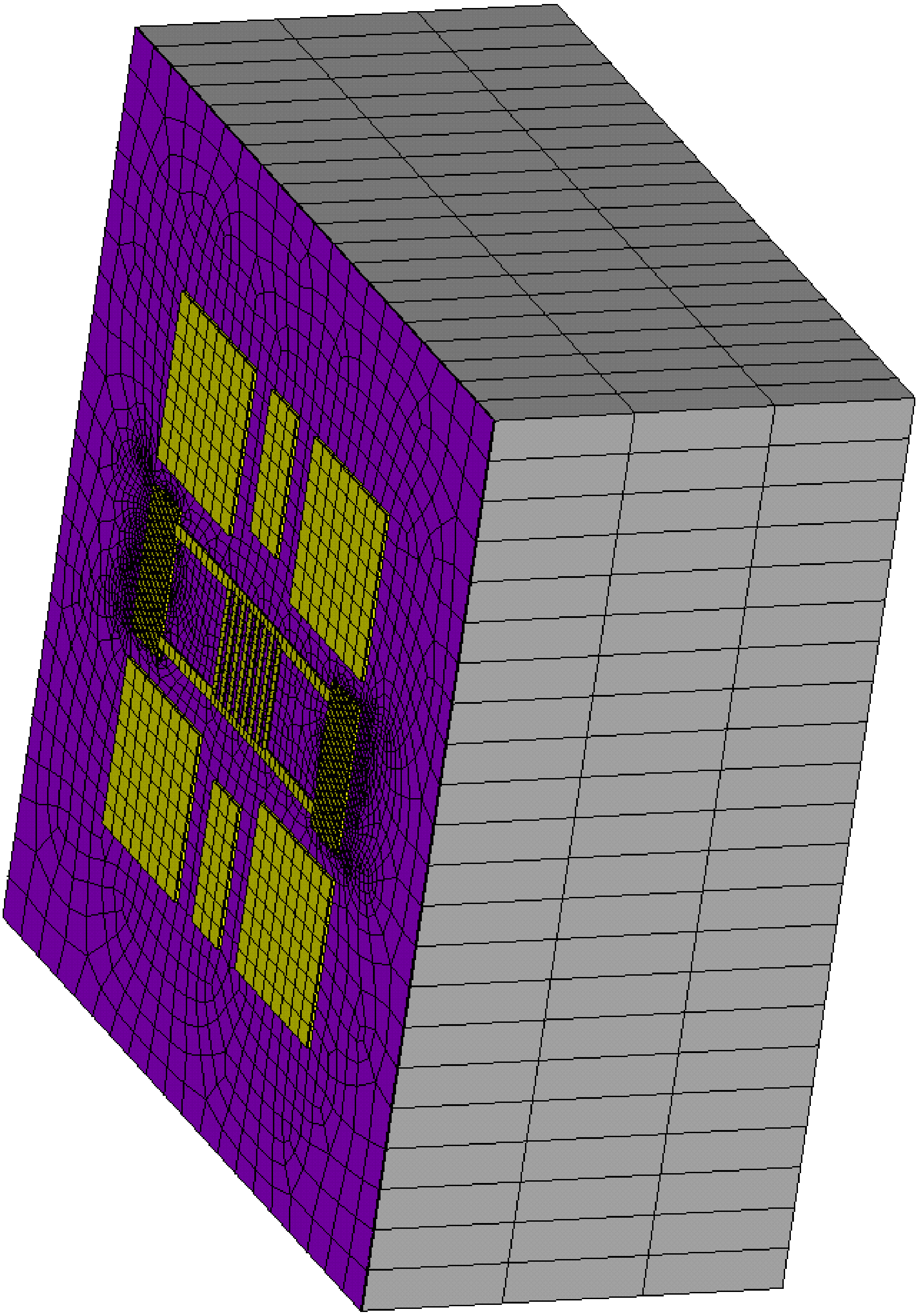

Figure 6.9: The meshed model of the RF-MEMS ohmic switch which layout is demonstrated in the Figure 5.2.

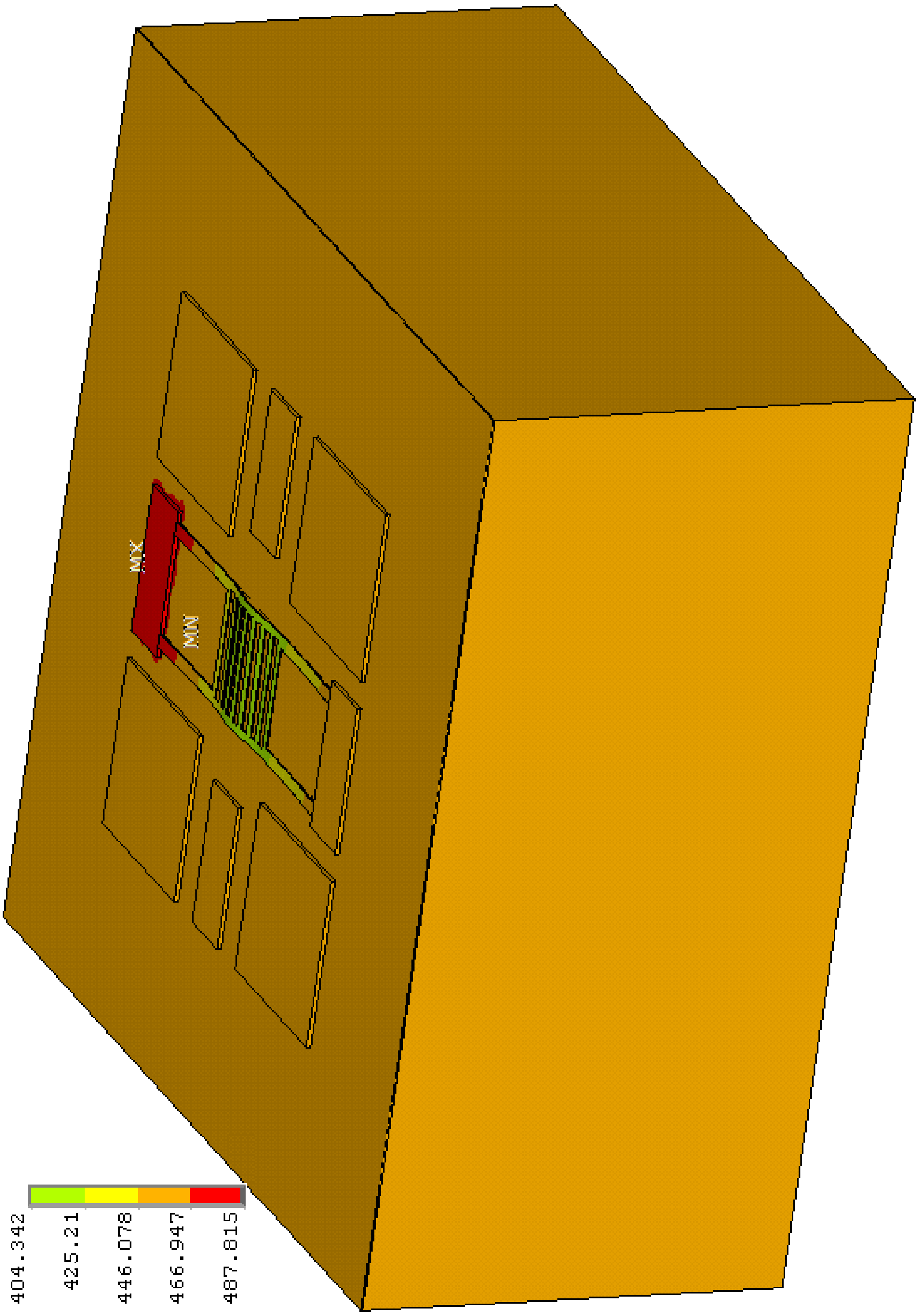

Figure 6.10: The temperature distribution through the die containing RF-MEMS ohmic switch due to the heat generated by the 250 V of DC bias applied to one of its heaters.

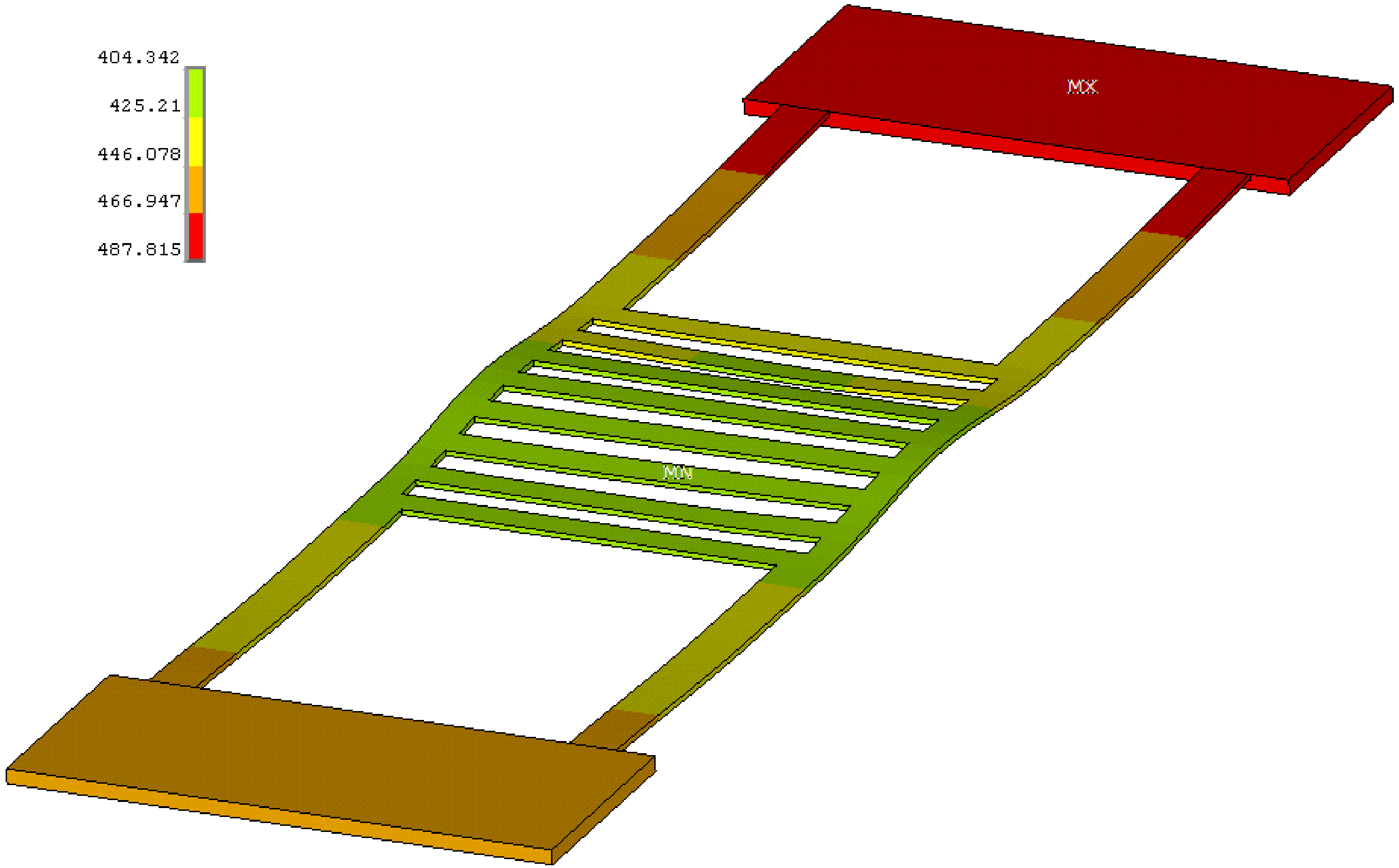

Figure 6.11: The displacements of RF-MEMS ohmic switch central plate due to material expansion generated by the induced heat.

Chapter 7

Experimental Results

The whole behaviour of the MEMS switch concept proposed in this thesis, involves different physical domains, namely, electrical, thermal, mechanical and electromagnetic. Consequently, both simulation and experimental testing require a careful planning in order to get sensible and accurate indications by such phases. The most reasonable approach in doing so, is to start from the coupling between two physical domain. After obtaining experimental results, such data have to be exploited in order to validate the simulation method adopted to describe the physical coupling of the two domains. Once the consistency between experiments and simulations is cross-checked, the next step is to increase the complexity of the analyzed problem, adding a further physical domain that couples with the previous ones analyzed. Such an incremental approach is important not only for what concerns simulations, but also for the experimental testing of MEMS devices. Indeed, each type of testing, depending on the particular physical effects analyzed, requires different measurement equipments and setups that need to be properly conceived and calibrated in order to yield accurate data.

7.1 Thermoelectric Measurements

Following the just discussed approach, we commenced our experimental investigation on the behaviour of the proposed MEMS switches starting from the coupling between the electrical and thermal domains. The DUT (Device Under Test) heat is generated driving an electric current through one of the heaters embedded within it (i.e. high-resistivity poly-silicon serpentine). The heating of the DUTs is observed by means of a thermal camera. In the experiments that are going to be shown we exploited two small pieces of wafer containing a few RF-MEMS switches with heating mechanism. Figure 7.1 reports the whole wafer layout, highlighting the two just mentioned pieces (labelled as sample A and B). The device distribution in both of them is reported in Figures 7.2 and 7.3, respectively. As first step, the effective resistance of the poly-silicon serpentine of the DUTs has been measured by means of a Keithley 2612 Source Meter, and its value is 39 kΩ.

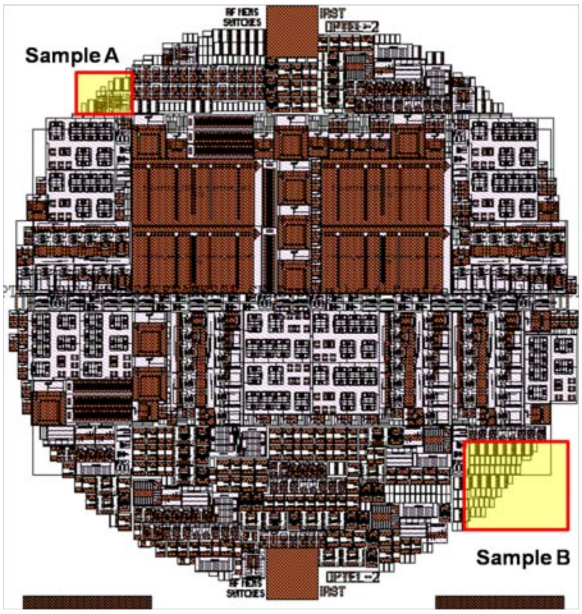

Figure 7.1: Whole wafer layout. The wafer is fabricated in FBK RF-MEMS technology, and the samples A and B are highlighted.

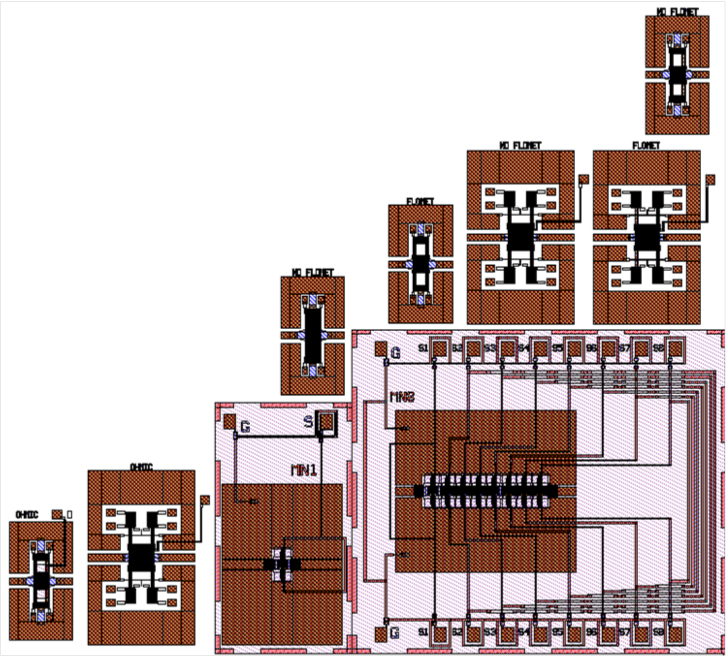

Figure 7.2: Close-up of the sample A layout (refer to Figure 7.1).

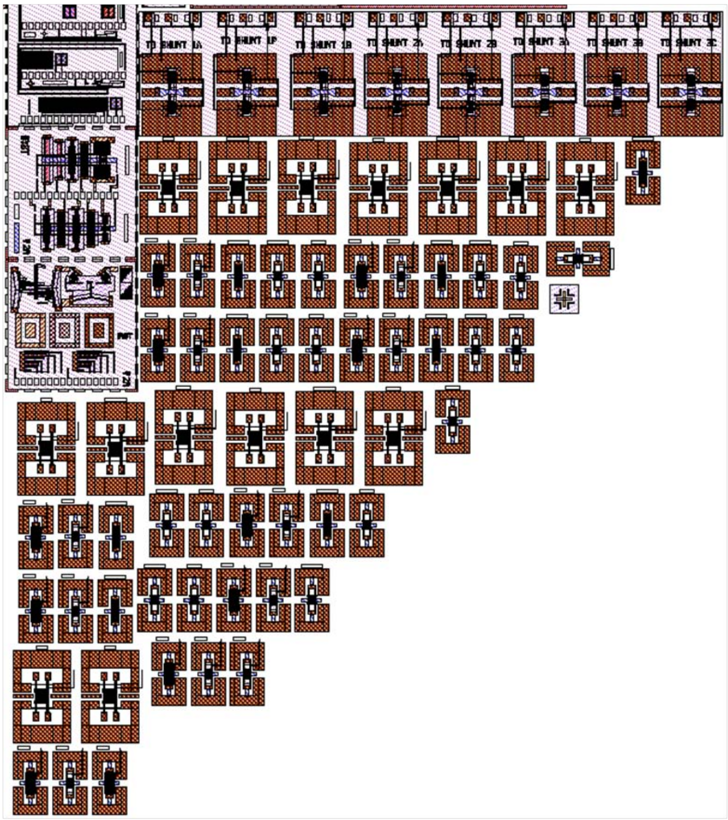

Figure 7.3: Close-up of the sample B layout (refer to Figure 7.1).

Subsequently, different currents have been driven by means of two micro-probes into the high-resistivity serpentine of one RF-MEMS switch sample. The devices have been tested onto a probe station, and in order to reach a thermal insulation between the silicon pieces and the heat sink represented by the metallic stage, a polystyrene layer has been placed in between, being such a material a good thermal insulator. A current of 1, 2, 3 and 4 mA was alternatively driven into the serpentine for different periods of time. In all cases, the applied current was a square-pulse (i.e. ON-OFF signal, with no rising and falling ramps). Moreover, between one measurement and the following one, the silicon pieces rested long enough to cool down again to room temperature. Figure 7.4 reports the thermal camera images for the small silicon piece (sample A in Figures 7.1 and 7.2) when the driven current is 4 mA. The micro-probes injecting the current into the poly-silicon are visible and highlighted in the left photograph. The temperature is reported for the four images after 2.5, 5, 7.5 and 10 sec of heating. The increasing intensity of the piece colour shows the heating of the whole silicon substrate (the scale on the right of Figure 7.4 reports the temperature range in Kelvin of the piece). The gold of the RF-MEMS samples on the silicon piece always look dark with respect to the surrounding silicon, like if they are still cold. This can be easily explained by the operation principles on which relies the infrared thermal camera. Generally, an infrared camera measures and images the emitted infrared radiation from an object. In order to obtain the correct thermal map of the object surface, the camera should be pre-setup. Emissivity of the object is one of the parameters that is necessary to specify in order to adjust this equipment. Since, in our case the camera was set up to represent correctly the temperature of silicon substrate (the emissivity is around 0.7), the temperature of the isles of gold (with emissivity value approx. 0.02) is not shown correctly. The temperature indicated in the labels below each image is the one measured in the specific point of the silicon surface indicated by the thick arrow in the second picture from the left, and is the same for all the other measurements. Such temperature values have been extracted by means of the software provided with the thermal camera that, after a measurement is performed and stored, allows to post-process the acquired data.

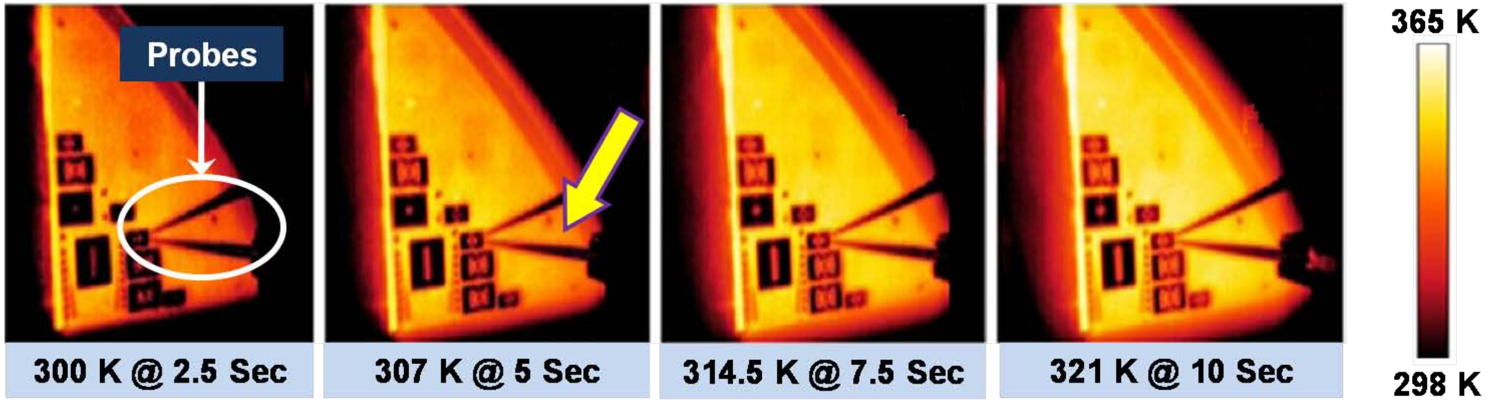

Figure 7.4: Thermal response of the sample A, as observed with the thermal camera, when applying a 4 mA current to a poly-silicon serpentine.

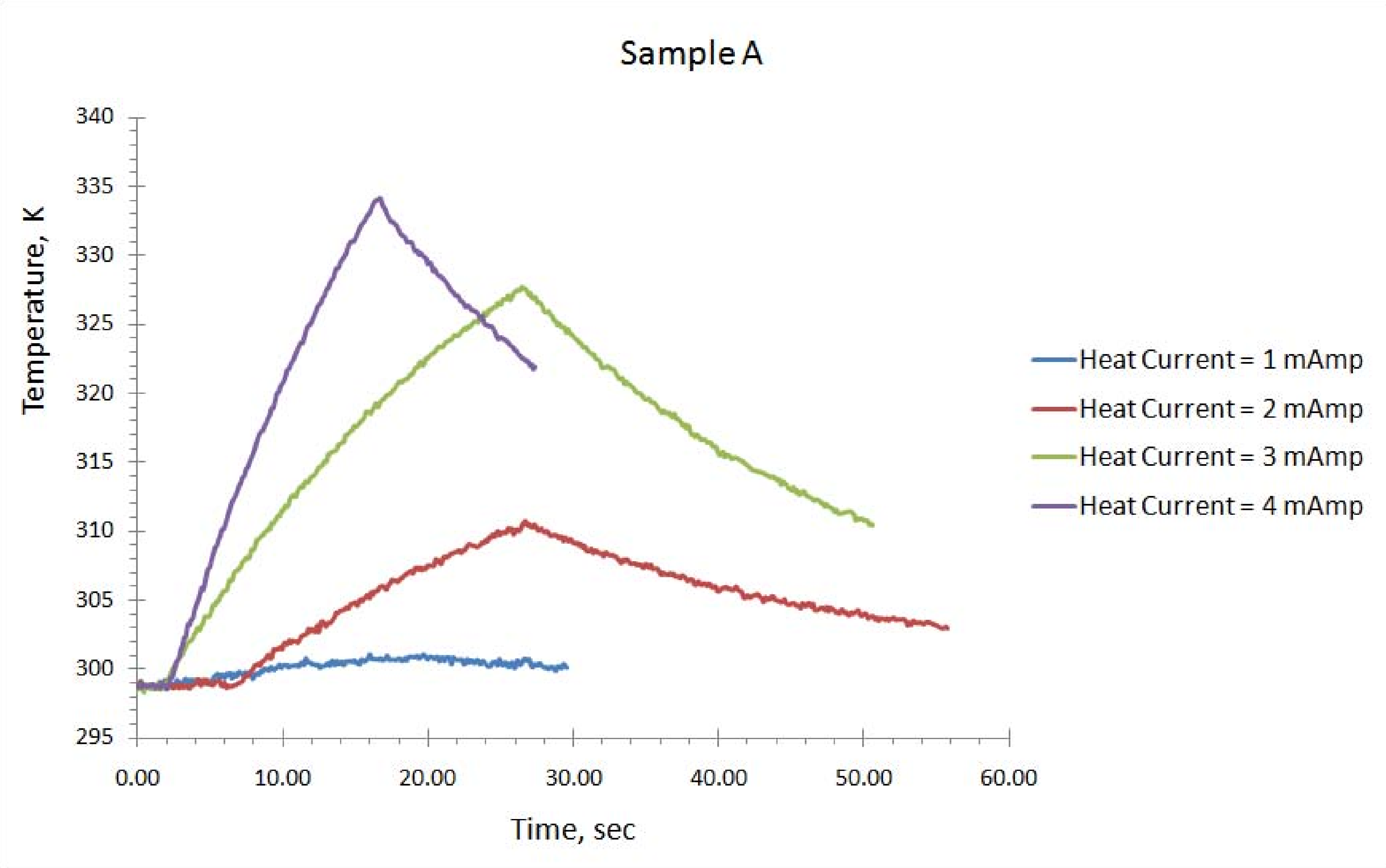

Figure 7.5: The graphs from thermal camera data for sample A.

The temperature of the same point on the silicon piece reported in Figure 7.4 is shown in the graph of Figure 7.5. As expected, there is a clear relation between the amplitude of the driven current and duration of the current pulse, and the maximum temperature of the specimen. As expected, the specimen exhibits a certain thermal inertia in increasing its temperature. This is due to the heat diffusion into the silicon. Moreover, the larger is the current driven into the serpentine, the faster is the temperature increase. This aspect poses the basis for some considerations on the final exploitation of the RF-MEMS devices discussed in this thesis. Indeed, in order to maximize the efficiency of the restoring mechanism, the heat diffusion should be as much limited as possible. This means that the final RF-MEMS device employed within a certain systems, should be thermally insulated by the surrounding components, also to avoid that the heat it produces when the restoring mechanism is activated could damage the surrounding devices.

The same measurements have been performed on the sample B. Figure 7.6 reports the thermal response of sample B observed with the thermal camera. Also in this case the driven current is 4 mA. Probes are indicated with two arrows in the left photograph, are not visible in the darker part of the sample, while become visible when the sample heats up (see the right picture). Also in this case the detected temperature refers to a specific point on the sample surface that is highlighted in figure with a thick arrow. The measured temperature is lower than in the case of sample A, as the piece surface is larger in this case This evidence confirms that, in the same conditions of driven current and heater resistance, the surface of the silicon piece influences the maximum temperature that can be reached. Moreover, given the rather uniform temperature diffusion, it is straightforward that it is rather indifferent which of the two heating serpentines is activated (see the RF-MEMS device layout in the chapter on fabrication and design).

The curve corresponding to a driven current of 4mA in the sample B specimen that is shown in Figure 7.7 is compared to the ANSYS simulation of the same structure, as reported in Figure 7.8. The qualitative comparison of the curves is rather good, even though differences concerning the temperature are visible both during the heating and cooling down of the specimen. The ANSYS model accounts both for radiation and convection at the boundaries of the silicon piece. In this simulation (transient) no heat sink has been set in the lower face of the substrate, i.e. where the physical specimen lays on the probe station. On the other hand, polystyrene was placed between the chuck and the specimen, in order to limit the heat dispersion towards the metal of the probe station. However, the thermal insulation provided by this solution is not as good as the one of a continuous layer of air (ANSYS simulation). This is the most likely reason for which the simulation overestimates the measured temperature (see Figure 7.8).

Finally, Figures 7.9 and 7.10 report two snapshots of the thermal camera software interface that allows extracting information from the acquired measurements.

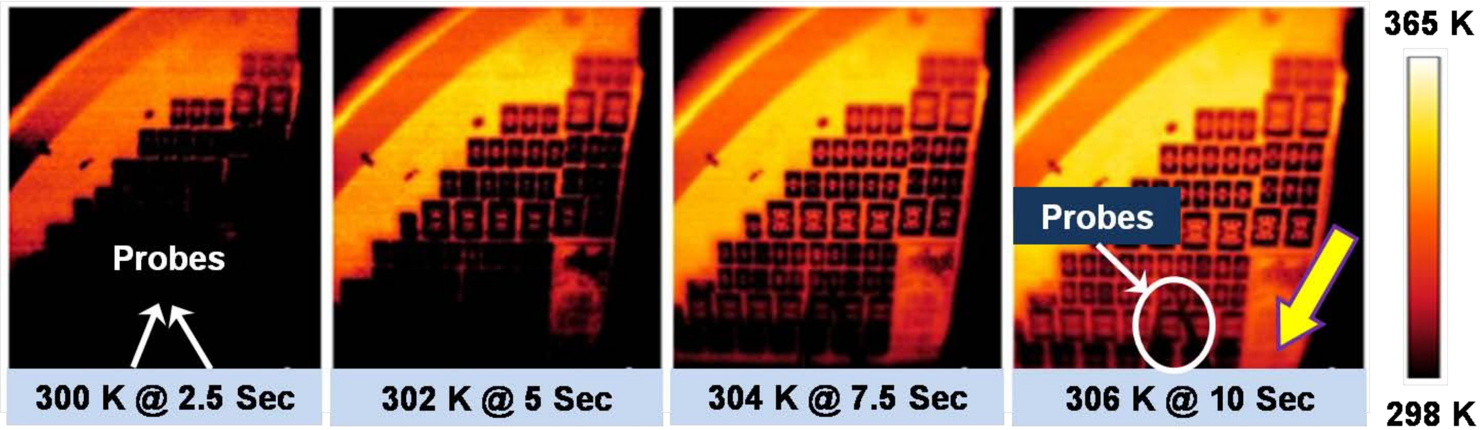

Figure 7.6: Thermal response of the sample B, as observed with the thermal camera, when applying a 4 mA current to a poly-silicon serpentine.

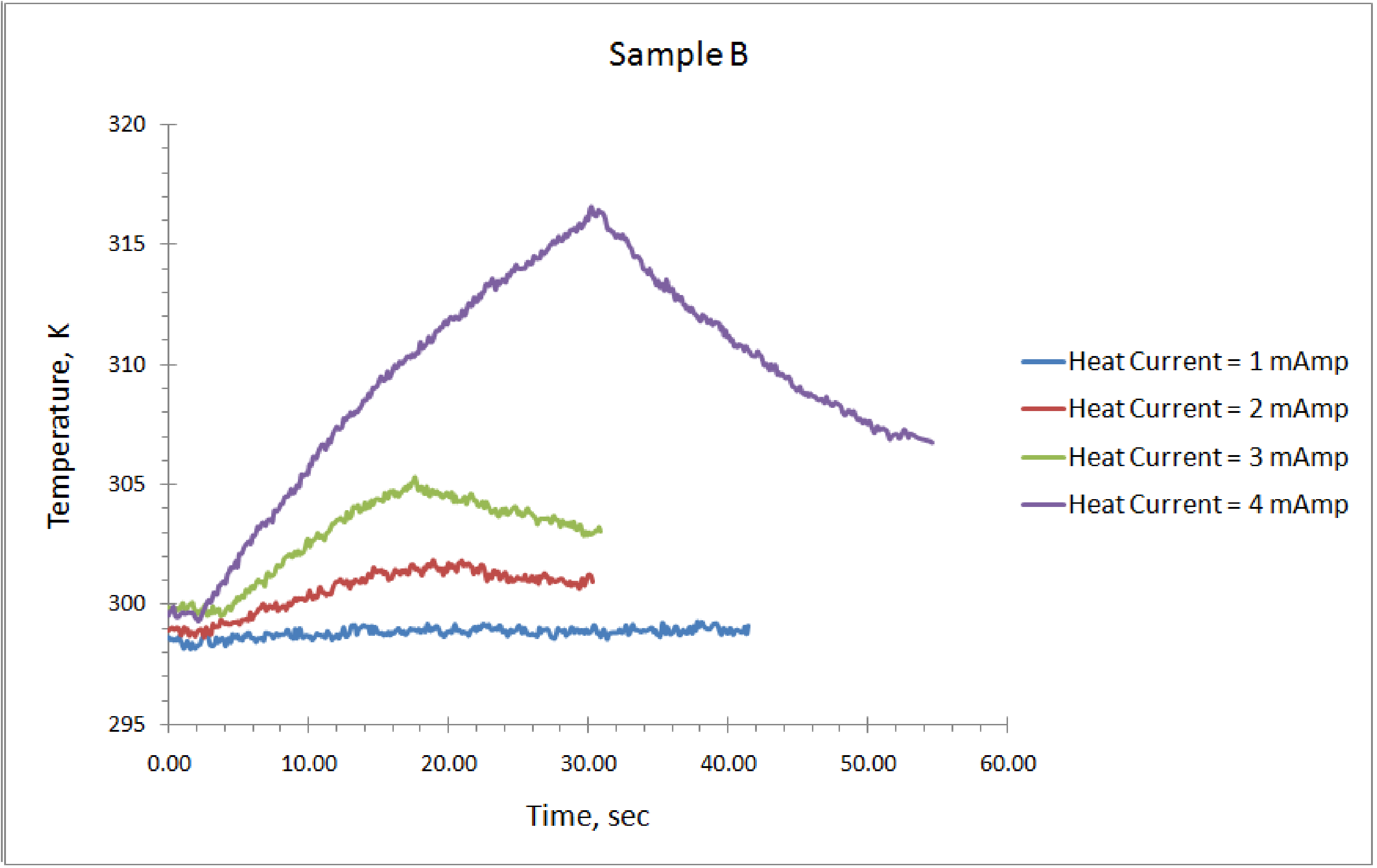

Figure 7.7: The graphs from thermal camera data for sample B.

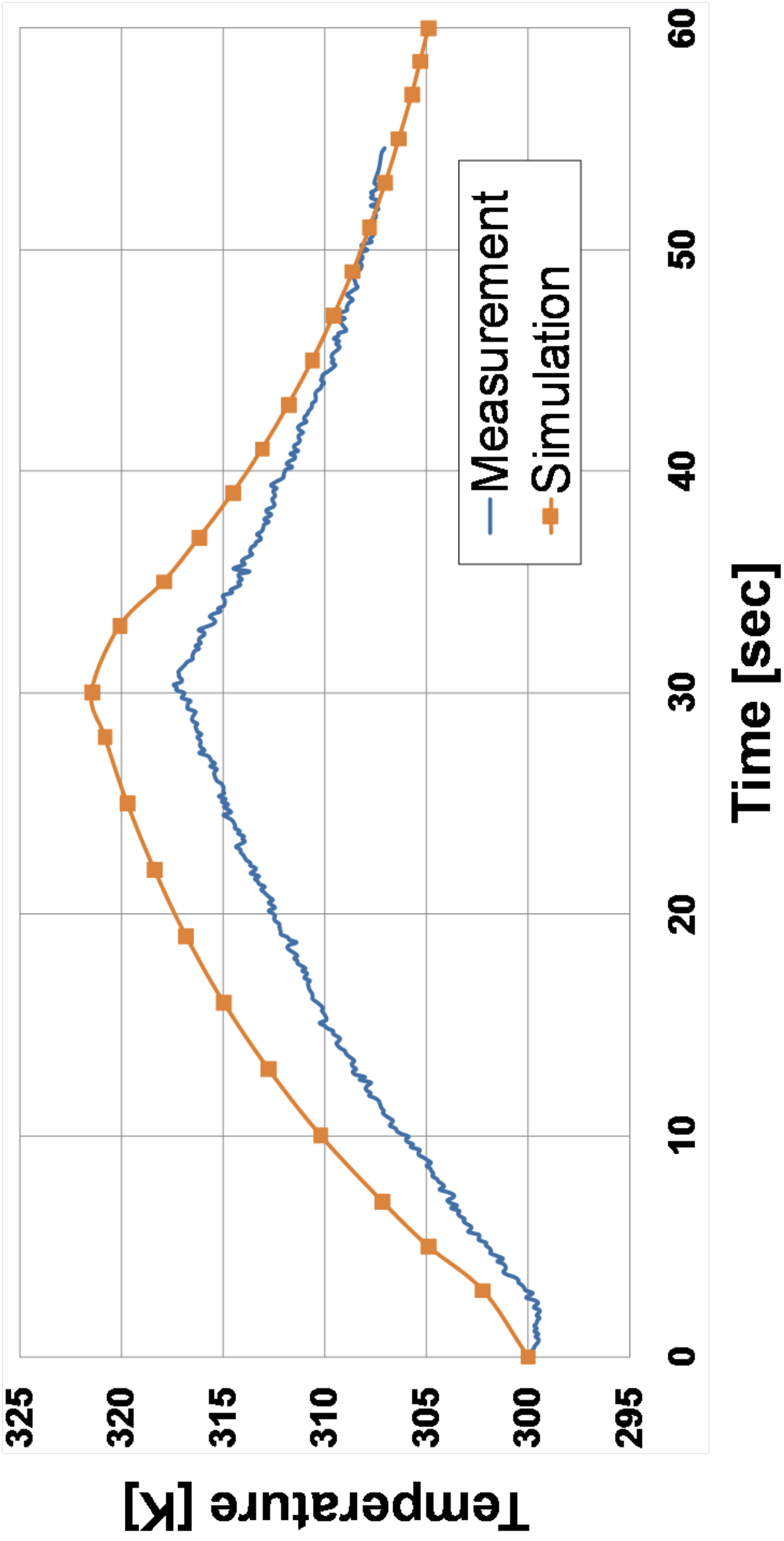

Figure 7.8: Measured vs. simulated behavior of the specimen temperature over time ($I_{Heater} = 4$ mA, 30 sec ON and 30 sec OFF).

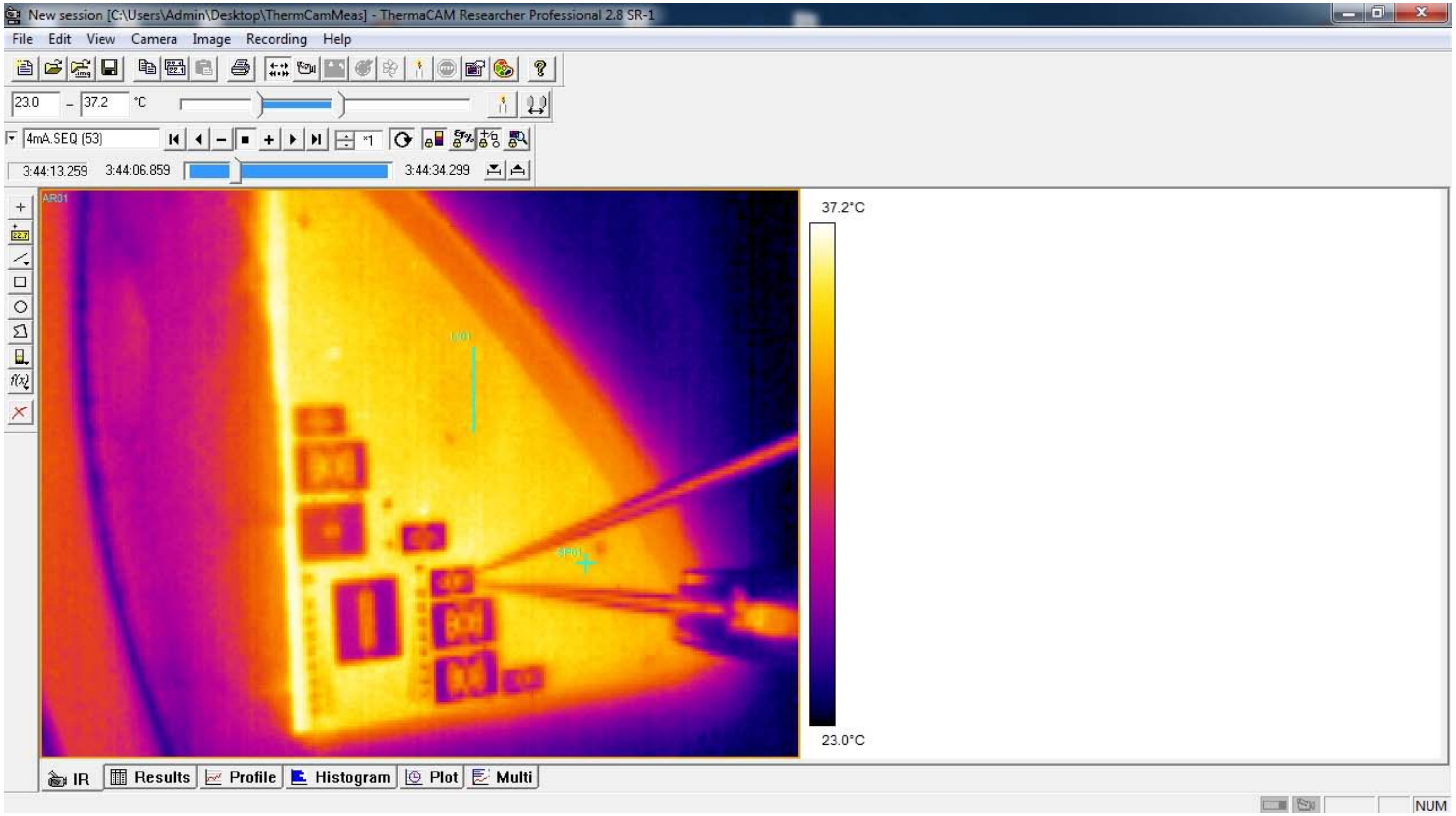

New session [C:\Users\Admin\Desktop\ThermCamMeas] - ThermaCAM Researcher Professional 2.8 SR-1

23.0 – 37.2 °C

4mA.SEQ (53)

3:44:13.259 3:44:06.859 3:44:34.299

Figure 7.9: The snapshot from of the interface of ThermaCAM™Researcher Pro 2.8 SR-1 software produced by FLIR systems AB ©.

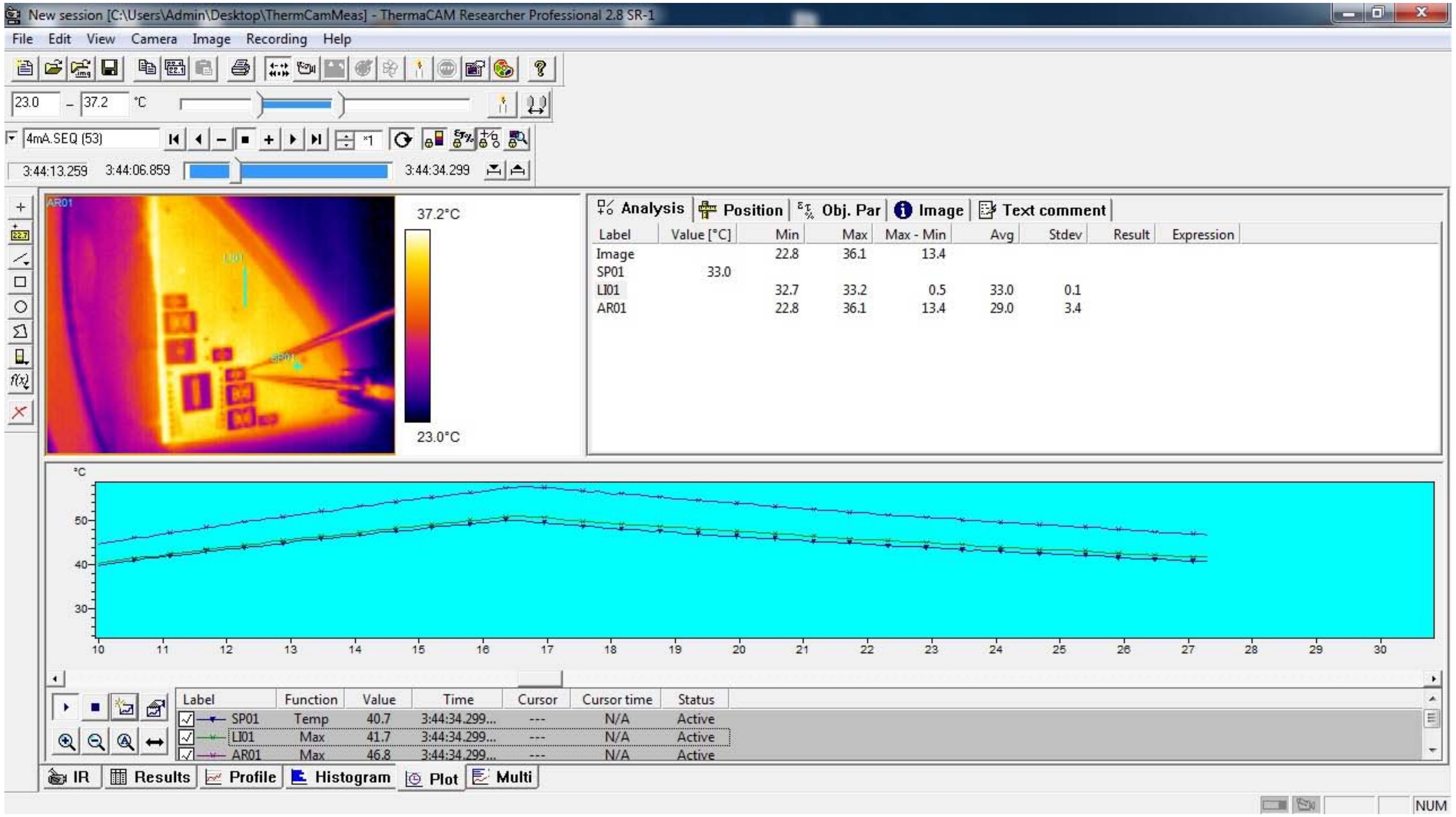

Label	Value [°C]	Min	Max	Max - Min	Avg	Stdev	Result	Expression
Image		22.8	36.1	13.4				
SP01	33.0							
LI01		32.7	33.2	0.5	33.0	0.1		
AR01		22.8	36.1	13.4	29.0	3.4		

Label	Function	Value	Time	Cursor	Cursor time	Status
SP01	Temp	40.7	3:44:34.299...	---	N/A	Active
LI01	Max	41.7	3:44:34.299...	---	N/A	Active
AR01	Max	46.8	3:44:34.299...	---	N/A	Active

Figure 7.10: The snapshot from of the interface of ThermaCAM™Researcher Pro 2.8 SR-1 software produced by FLIR systems AB ©.

7.2 Electromechanical and Electromagnetic Measurements

The experimental testing of the discussed samples has been carried out by means of an on-purpose setup reported in Figure 7.11. The measurement setup exploits the S-parameters observation as read-out of the switch state (actuated/not-actuated, stuck or released). The input/output ports of the switch are contacted with GSG (Ground-Signal-Ground) microprobes connected to a VNA (Vector Network Analyzer). The RF power supplied to the MEMS device is 0 dBm and S-parameters are monitored at the constant frequency of 6 GHz. The VNA has not been properly calibrated because we are interested in monitoring the state of the switch rather than its RF performances, that in any case are not good because of the layout issues previously discussed. Beside the S-parameters monitoring, one DC voltage source is exploited in order to provide the proper controlling voltage to the suspended MEMS plate and another DC power source is used to drive the current through the high-resistivity poly-silicon heater. Both the sources are connected to the MEMS samples by means of DC microprobes onto a probe-station.

A LabView routine has been implemented on purpose in order to control all the measurement equipment mentioned above and also to collect the experimental data. The graphic interface of the routine is shown in Figure 7.12.

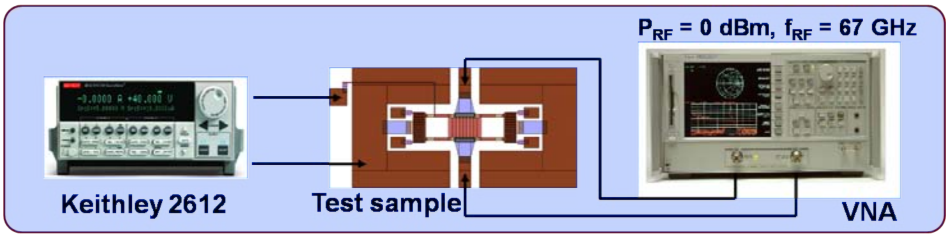

Figure 7.11: Measurement Setup.

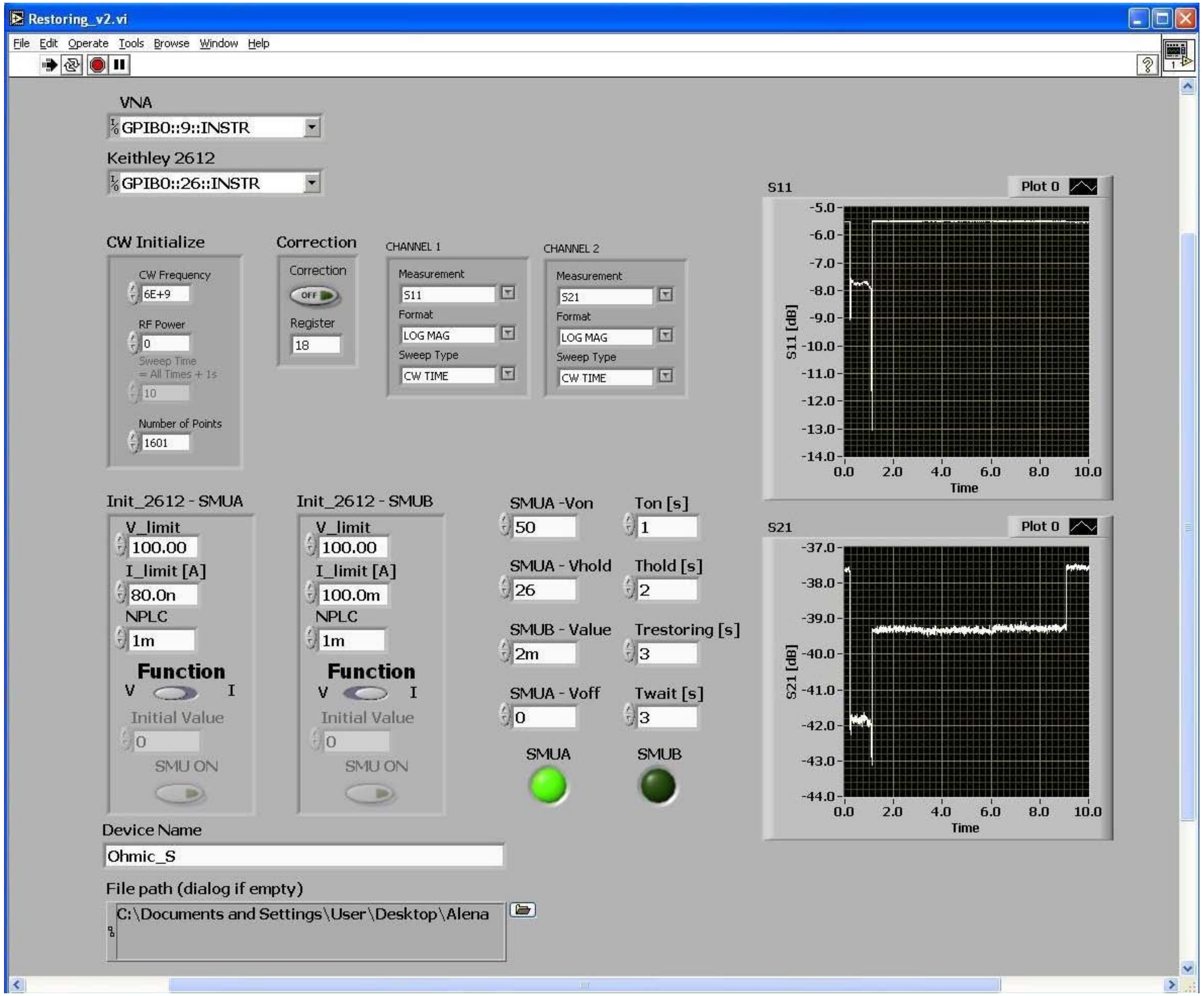

VNA
GPIB0::9::INSTR

Keithley 2612
GPIB0::26::INSTR

CW Initialize
CW Frequency 6E+9
RF Power 0
Sweep Time = All Times + 1s 10
Number of Points 1601

Correction
Correction OFF
Register 18

CHANNEL 1
Measurement S11
Format LOG MAG
Sweep Type CW TIME

CHANNEL 2
Measurement S21
Format LOG MAG
Sweep Type CW TIME

Init_2612 - SMUA
V_limit 100.00
I_limit [A] 80.0n
NPLC 1m
Function V I
Initial Value 0
SMU ON

Init_2612 - SMUB
V_limit 100.00
I_limit [A] 100.0m
NPLC 1m
Function V I
Initial Value 0
SMU ON

SMUA -Von 50
Ton [s] 1
SMUA - Vhold 26
Thold [s] 2
SMUB - Value 2m
Trestoring [s] 3
SMUA - Voff 0
Twait [s] 3

Device Name
Ohmic_S

File path (dialog if empty)
C:\Documents and Settings\User\Desktop\Alena

Figure 7.12: Snapshot of the LabView routine interface exploited for the measurements.

A few MEMS switch samples have been tested under different stress and operation condition. In general, it was noticed that this particular layout is not particularly prone to the stiction induced by the charge entrapped into the silicon oxide layer. This is very likely due to the vertical step between the polysilicon electrode and the RF in/out multimetal contact areas, that does not allow any direct contact between the suspended gold plate and the oxide above the biasing electrode also when the plate is actuated (see Figure 5.1). This characteristic avoids the charge direct injection between the suspended MEMS membrane and the insulating layer. Besides, the straight flexible suspensions are rather rigid, leading to a large restoring force. Because of these motivations, in some experiments carried out, when it was not possible to reach a stiction condition also after several hours of constant polarization of the DUT (Device Under Test), an alternative way to keep the MEMS membrane down was exploited. By definition, stiction due to accumulated charge occurs when the amount of charge is large enough to generate a spurious effective bias larger than the pull-out voltage. Consequently, the LabView routine controlling the setup was extended in order to apply a voltage larger than the MEMS pull-in one, indeed actuating the switch, and then lower it to a level slightly higher than the pull-out one. The result is that the switch is still kept down but in a condition that is closer to the one of stiction. The aim is to observe the effect of the serpentine heating during this low-voltage biasing phase. Even just a small upward movement of the plate caused by the heat-induced deformation could be sufficient to release the switch. It can be analytically explained looking at the pull-out voltage formula (7.1), [79]:

$$V_{\text{pull-out}} = \sqrt{\frac{2k_e}{\varepsilon\varepsilon_0 A}(g_0 - g)\left(g + \frac{t_d}{\varepsilon_r}\right)^2} \tag{7.1}$$

where, k_e is the equivalent spring constant taking into account the stretching component, g_0 and g are the correspondingly the default and the current distance between the movable and the fixed electrodes, where t_d and ε_r are the thickness and relative dielectric constant of the dielectric layer, ε_{air} is the permittivity of air, ε accounts for the reduction in the parallel-plate capacitance due to the roughness of the metal-to-dielectric interface and finally A is the area of the electrodes. From the (7.1), the Figure 3.3 and recalling the fact that the intensity of the stiction forces reduces with increasing the distance between the contact areas, the release of the switch could occur even if the induced heat will cause rather small vertical displacement of the central plate.

The experimental data reported below refer to one of the few samples for which it was necessary to apply the hold-down bias discussed above. The device layout is the one reported in Figure 5.2 First of all, a DC sweep was applied to the controlling bias in order to observe the pull-in/pull-out static characteristic of the DUT. The applied voltage is a triangular zero mean value symmetric bias, ranging from -60 V up to 60 V. The measured S_{11} parameter characteristic (return loss) is reported in Figure 7.13, while the S_{21} transmission parameter is shown in Figure 7.14. Looking at Figure 7.13, the pull-in transition is visible, both in the positive and negative voltage regions, at around 40 V, while the pull out occurs at around 23 V. However, such transitions are more evident in the S_{21} plot (Figure 7.14), where a transition of about 10 dB is visible between the actuated and not actuated states. The stability of the ohmic contact is very poor, but this issue is related to the fact that the design was conceived just for testing purposes of the heating mechanism, and not to address good RF performance. The DUT layout, indeed, is derived from a shunt variable capacitor. The only difference is in the in/out signal path that is discontinuous, and in the opening of ohmic contact areas underneath the suspended plate. This means that when the switch is not actuated, there is an open between the input and output lines. On the other hand, when the switch is actuated, the RF signal finds a low-resistive path to ground, and the entire structure behaves as a short. Consequently, in both cases the RF signal present to one port of the DUT does not reach the other end of the structure. At this preliminary stage, such an issue can be tolerated as, on one side, we are not interested in the RF characteristic of the samples and, on the other hand, the readout of S-parameters make in any case possible to observe the influence of the heating on the state (ON/OFF) of the DUTs.

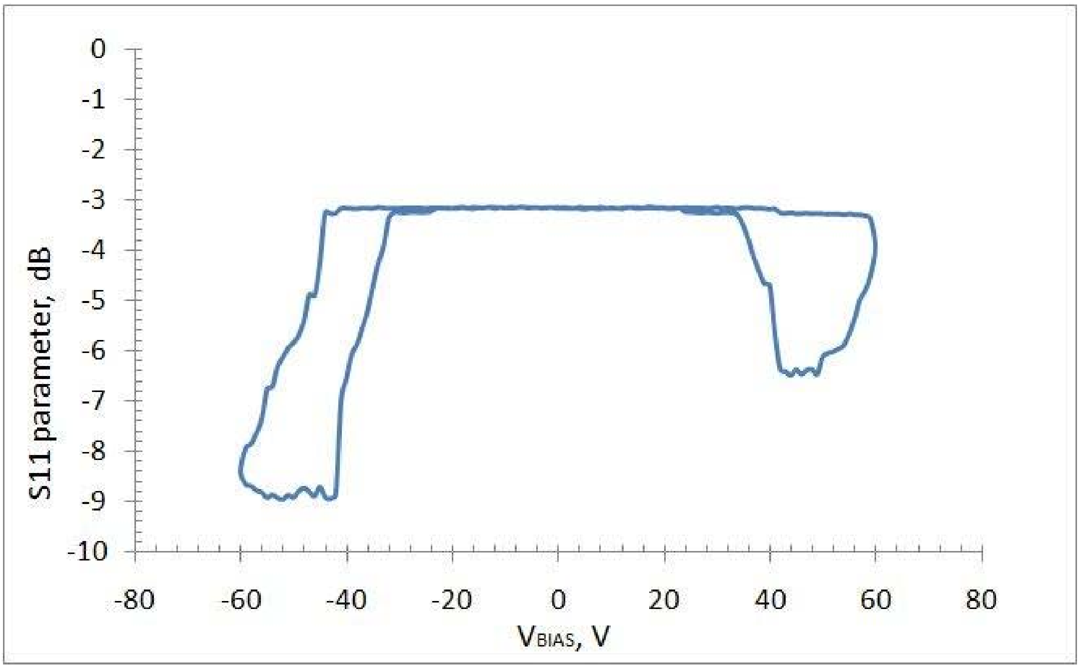

Figure 7.13: S_{11} parameter measured at 6 GHz when a triangular bias is applied to the device, highlighting the pull-in/pull-out characteristic.

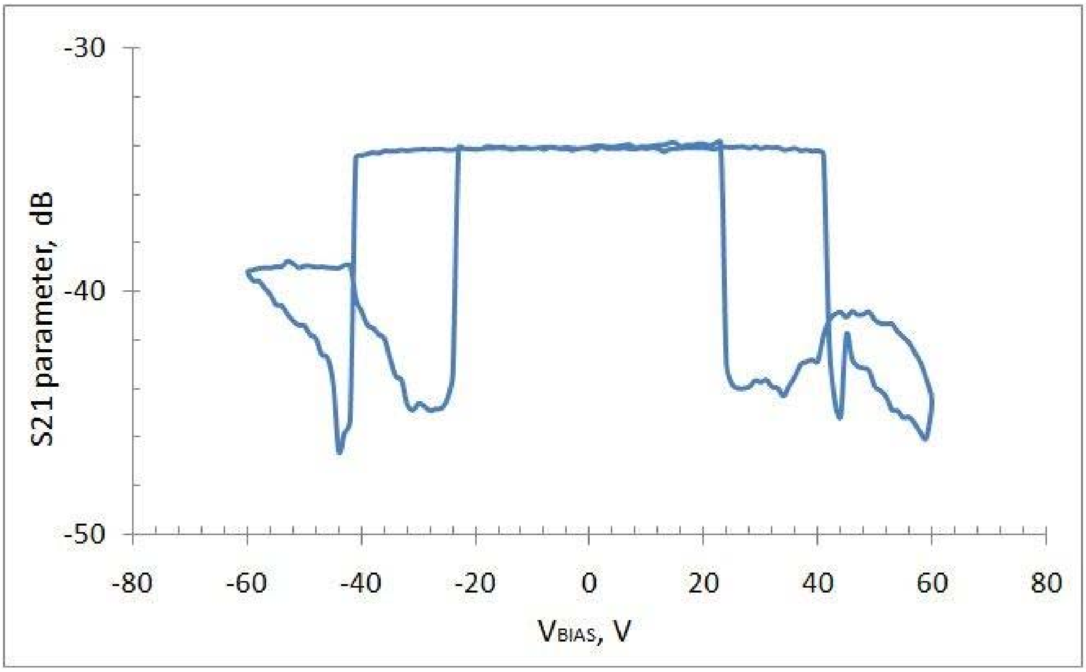

Figure 7.14: S_{21} parameter measured at 6 GHz when a triangular bias is applied to the device, highlighting the pull-in/pull-out characteristic.

In the following plots, the S_{11} and S_{21} parameters are reported versus time. After a delay of 200 msec, a voltage square pulse with a peak value of 50 V is applied and kept for 1000 msec in order to bring the DUT in the actuated state (see the plots in Figures 7.13 and 7.14). After that, the bias is lowered from 50 V down to about 25 V, i.e. lower than the actuation voltage but slightly higher than the release voltage (i.e. hold bias), ins such a way to keep the central plate down, indeed creating a condition very similar to the stiction induced by accumulated charge. After 2000 msec and while the hold voltage is still applied, a current is driven through the high-resistivity serpentine heater for 3000 msec, then the current is switched off and the hold voltage is still kept for 3000 msec. After this, the hold bias drops to zero and the evolution of S-parameters is still observed for 1000 msec. All the measurement phases just described are highlighted in the following plots by means of vertical lines also described in the labels.

Let us start analyzing the plots reported in Figures 7.15 and 7.16 (S_{11} and S_{21} parameters, respectively). In this case the applied hold bias after the 50 V peak is 24.5 V. The S-parameter measurement was repeated four times with 0 mA driven into the serpentine (i.e. no bias applied to the heater pads), 1 mA, 2 mA and 3 mA. Since the resistance of the heating (34 KΩ) was previously determined by means of a tester, the DC voltage applied to the heater in order to drive the currents just mentioned was: 0 V, 34 V, 68 V and 102 V, respectively. In all cases, the S_{11} parameter shows a rather large variation between the rest position (around 5.5 dB) and the actuated one when the 50 V peak is applied (around 10.5 dB). However, when the voltage drops to the hold value of 24.5 V, the S_{11} reaches a value very close to the rest position. This characteristic is also confirmed by the pull-in/pull-out experimental characteristic previously reported in Figure 7.13, where in the voltage range between the pull-out and the pull-in, the S_{11} difference between the actuated and rest position

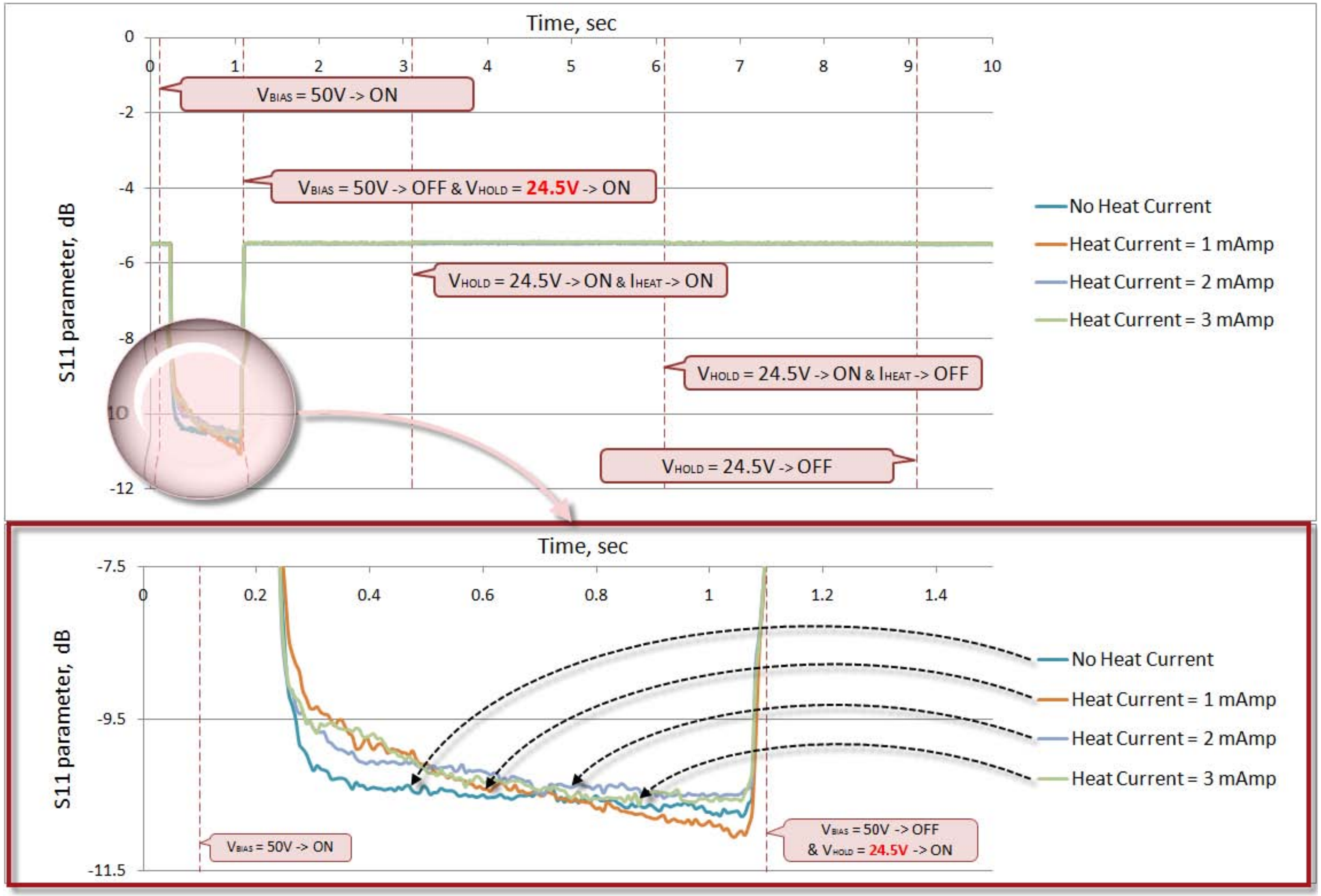

Figure 7.15: S_{11} parameter measured vs. time when no current is driven into the heater, and when a current of 1, 2 and 3 mA flows through it. The hold voltage applied to the switch is 24.5 V.

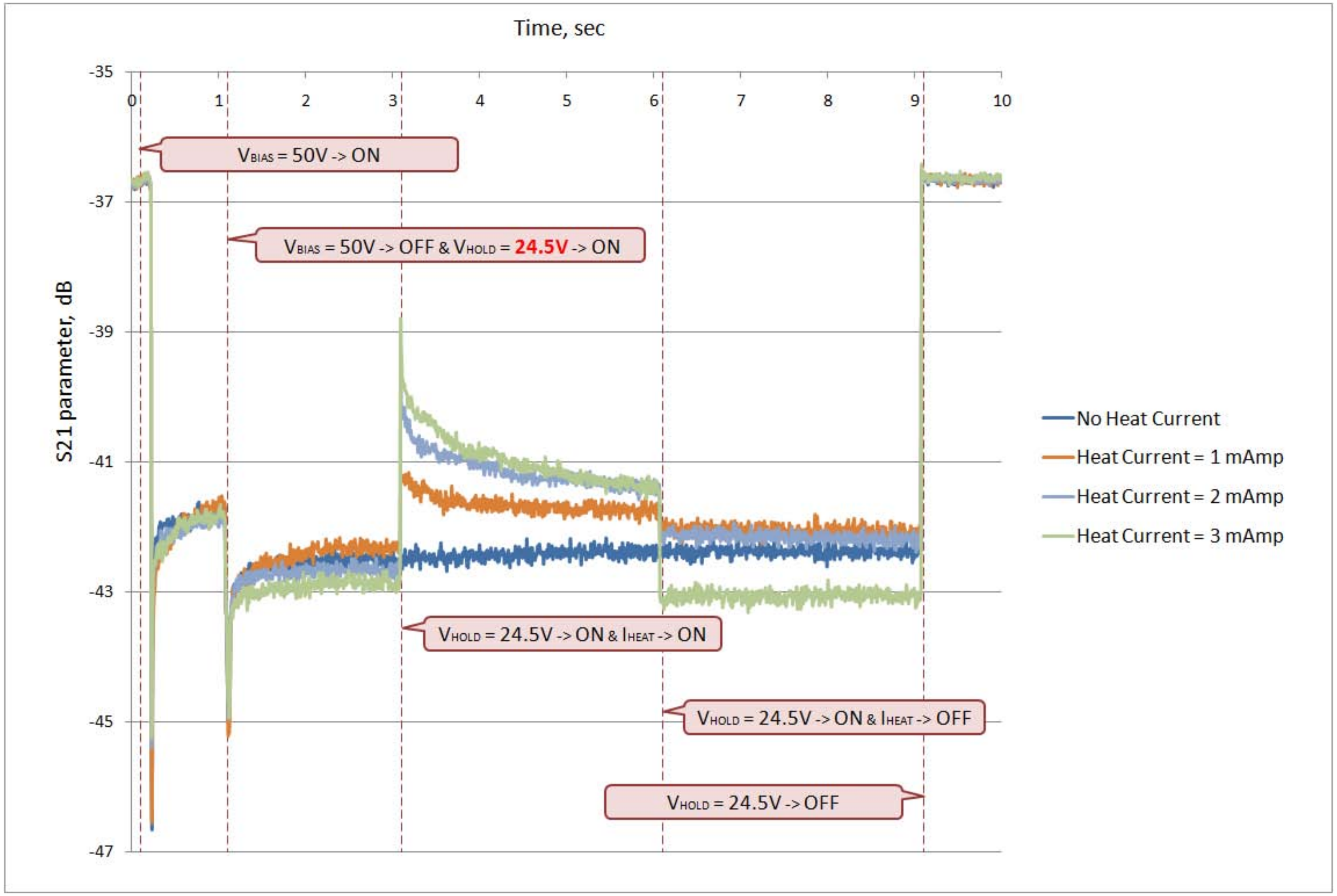

Figure 7.16: S_{21} parameter measured vs. time when no current is driven into the heater, and when a current of 1, 2 and 3 mA flows through it. The hold voltage applied to the switch is 24.5 V.

is just around 0.2 dB. On the other hand, since the S_{21} exhibits a larger range between the rest and actuated position, it enables a clearer reading of the switch evolution during the measurement.

Figure 7.16 shows that when the 50 V bias is applied, the S_{21} shows a large peak due the contact between the suspended gold membrane and the underneath ohmic contacts. After this very short transient, the S_{21} start to increase from about 43 to 42 dB. This decrease of isolation is due to the charge accumulation in the oxide layer above the polysilicon electrode, that screens over time the applied voltage, indeed leading to an effective electrostatic attractive force that is lower. This consideration is confirmed also when the peak voltage drops to the hold one (24.5 V). In the phase before the heating current is applied, indeed, the S_{21} snaps down to a slightly higher isolation level, due to the bias decrease that reflects, because of the accumulated charge, into a higher attractive force. Looking at the S_{21} curve corresponding to 0 mA driven into the heater, i.e. no heating, a slight decrease of the isolation is visible (0.1-0.3 dB) until the hold voltage is removed and the switch comes back into its initial position. Let us focus now on the phase of the measurement when the heating current is applied. Regardless of the current magnitude applied, the S_{21} shows a peak towards a worse isolation, i.e. a decrease in contact pressure on the ohmic areas, proving indeed the existence of a restoring force induced by the thermal expansion. After this peak, the S_{21} tends to decrease, leading to slightly better isolation levels, which means towards the actuated state. A clear correlation between the amplitude of the induced restoring force and the driven current magnitude is visible in Figure 7.16. When the heat is removed, the S_{21} suddenly comes back to a value very close to the one of the first measurement without activating the heater. Only in the case of 3 mA the S_{21} snaps down to a value slightly lower than the one of the first measurement, but in line with the trace corresponding to 3 mA before the heat is induced. Very likely, in this case, the larger amount of heat induced by the current heats up the oxide enough to speed-up the entrapped charge dispersion. This might explain a larger attractive force when the heat is OFF and the hold bias is still ON.

Looking now at Figures 7.17 and 7.18, it is possible to observe the measurements similar to the previous ones but, in this case, with an hold voltage of 25 V. Also in this case, the S_{11} plots do not allow a clear reading of the switch behavior. On the other hand, looking at the S_{21} parameter (Figure 7.18) gives much more information. Also in this case, the 50 V bias causes a sudden peak of isolation that then tends to decrease a little over time. When the bias drops down to the hold voltage (25 V) the S_{21} is slightly better and seems also rather flat. In particular, in this case is more visible the effect of accumulated charge increase as the measurements are performed in sequence. Indeed, assuming that not all the charge is released before the next measurement, it is possible to see that the S_{21} slightly increases from the first to the last measurement (i.e. no heat, 1, 2 and 3 mA). Focusing now on the phase of the measurement when heating is induced, when the current is 1 and 2 mA a restoring force is indeed induced. On the other hand, when the current is 3 mA it seems that the thermal expansion results in an additional contribution to the contact force (directed downward) rather than in a restoring force (directed upward). It is rather difficult to have a clear understanding of how the thermal expansion acts on the central plate, and, as demonstrated by the results here discussed, depending on several factors it can induce both a restoring force or a further contribution to the actuation force. In the following phase when the heat mechanism is OFF, the four traces are rather close together, being the latter an additional evidence of the trapped charge dispersion speed-up cause by the heat.

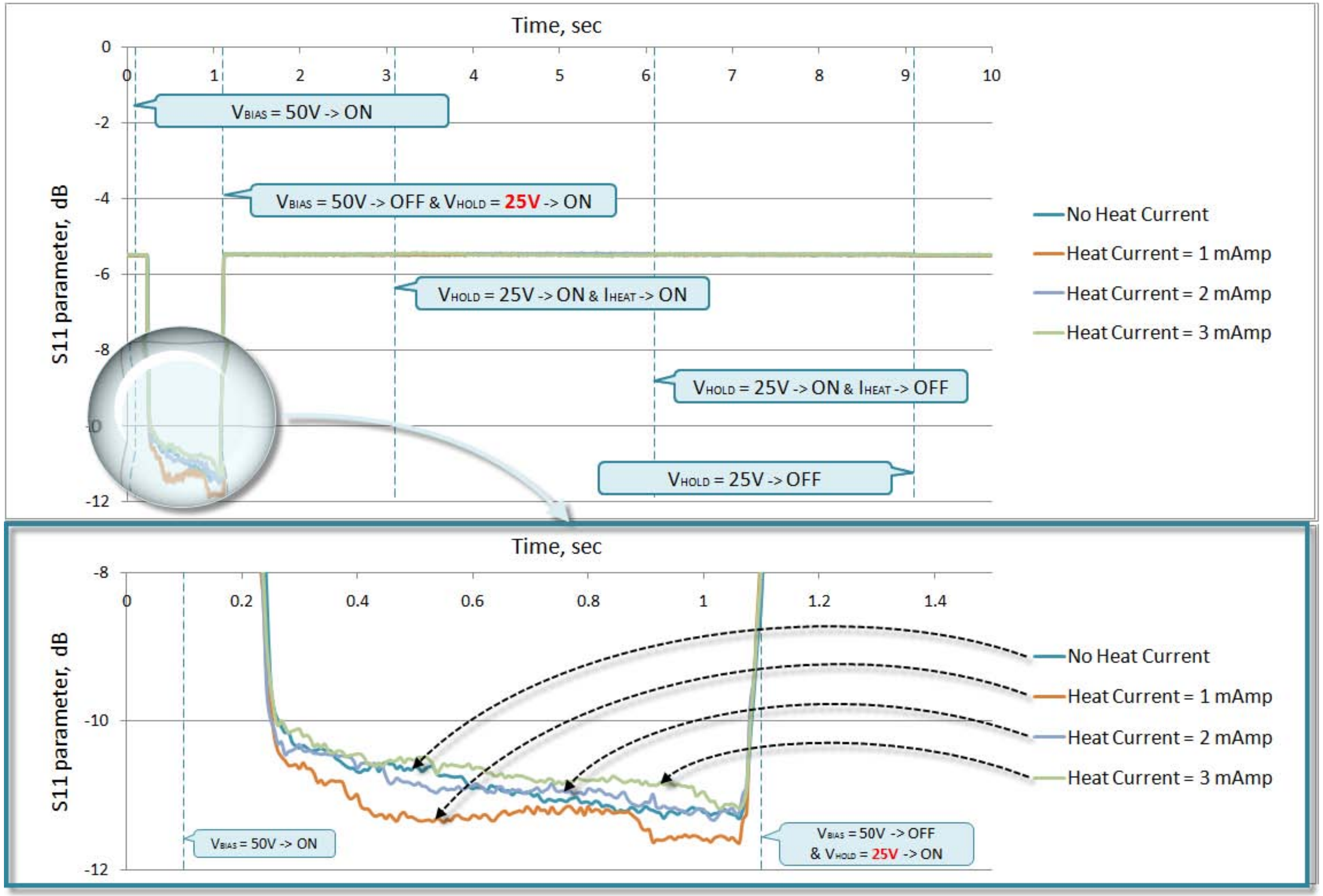

Figure 7.17: S_{11} parameter measured vs. time when no current is driven into the heater, and when a current of 1, 2 and 3 mA flows through it. The hold voltage applied to the switch is 25 V.

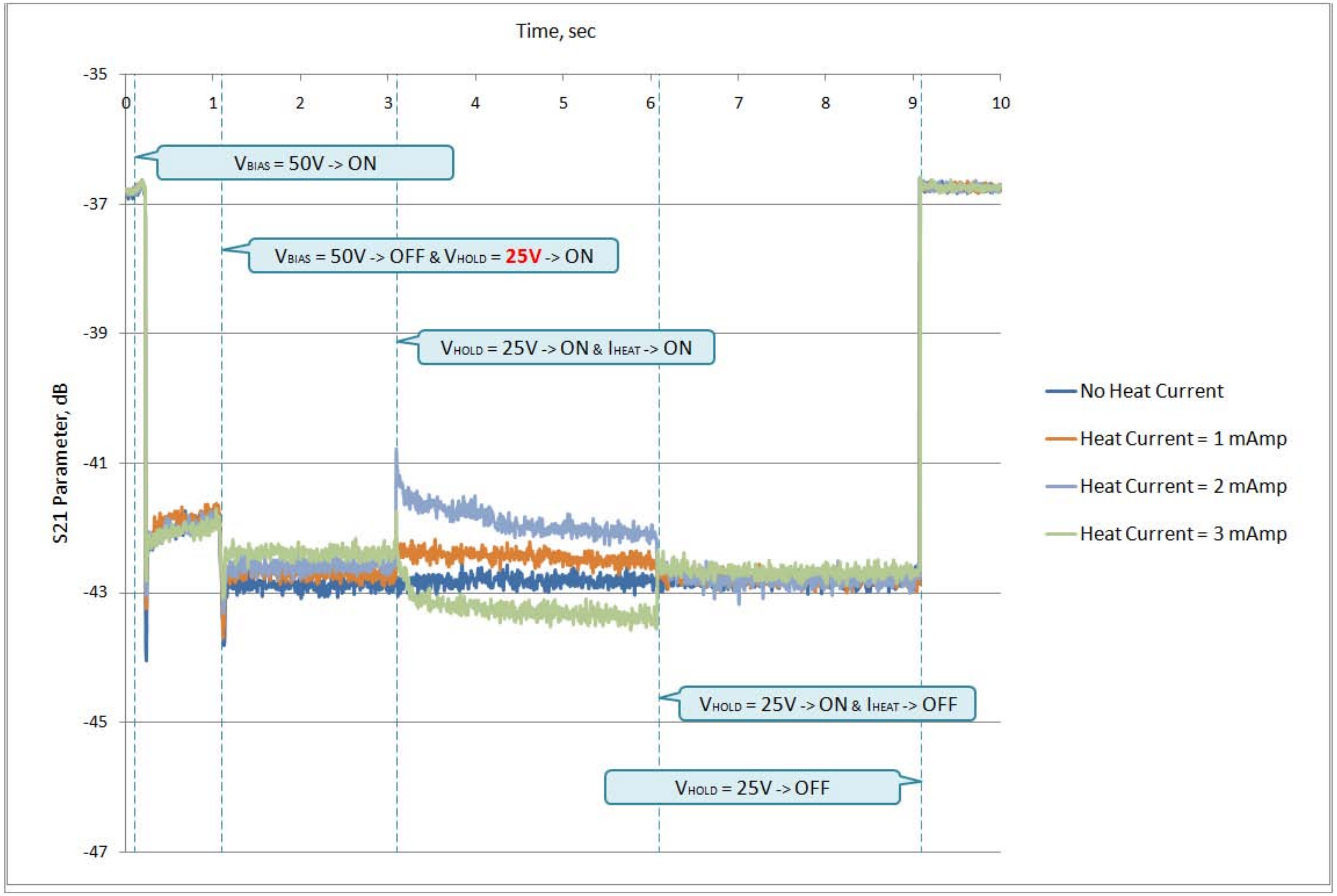

Figure 7.18: S_{21} parameter measured vs. time when no current is driven into the heater, and when a current of 1, 2 and 3 mA flows through it. The hold voltage applied to the switch is 25 V.

Below, experimental data referred to another sample like the just discussed one are shown. Looking at Figures 7.19 and 7.20 the S_{11} and S_{21} parameters are visible as a function of the triangular applied bias from -70 V to 70 V. In this case the return loss (S_{11}) is the trace showing a larger step between the actuated and not actuated states and, consequently, will be exploited in the following plots in order to monitor the effect of heating.

In the following Figure 7.21, the switch is brought to actuation by applying a bias level beyond the pull-out one. Afterwards, the voltage is lowered to 27 V. In the following measurements data have been collected only after the biasing voltage dropped to the hold level. Looking at the behavior of the S_{11} parameter when the heating current is switched ON and OFF, it is clear that the thermal expansion leads to an additional force contribution directed downward, indeed opposing the release. In this case, the current driven into the serpentine is 1 mA.

In Figure 7.22 the measurement conditions are the same of previous figure, but in this case the current driven into the serpentine is 1.5 mA. Peaks towards a better return loss values are visible when the current is pulsed ON. However, a clear difference between the time portion with and without heating is not visible.

In Figure 7.23 the response to a heating current of 2 mA is reported. In this case the heating induces effectively a restoring force (directed upward) as the S_{11} diminishes of about 6 dB when the heater is working, in comparison to the initial state.

Figure 7.24 shows the response when a current of 3 mA is forced into the heater. In this case the behavior is more complicated with respect to previous cases. The first pulse, longer in time compared to previous plots, causes, right after the down-peak, an increase of return loss, compatible with the presence of a restoring force. However, during the pulse, the S_{11} starts to decrease, indicating a better ohmic contact (downward displacement of the central plate). On the other hand, the second applied pulse still causes a pulse towards a small value of S_{11} (40 dB) that, subsequently, tends to increase. In any case, the effect of the second pulse is all against the release of the actuated structure.

The further plot reported in Figure 7.25 still refers to an applied current of 2 mA, even if this time the hold bias was lowered to 25.5 V, i.e. closer to the pull-out voltage. In this case the heating pulse causes, an increase of S_{11}, corresponding to the introduction of a restoring force. Moreover, when the pulse is switched OFF, the plate releases despite the hold voltage is still ON. In this case, the heating mechanism definitely helped in recovering the DUT from the actuated position.

Finally, Figure 7.26 shows the S_{11} behavior when the heating current is pulsed ON and OFF several times.

In order to conclude this section some considerations are needed. The yield of the devices that released because of heating was rather low, as the measurement reported above suggest. However, it was noted that the same device, depending on the particular applied heating current and hold voltage, can or cannot reach a successful release. First of all it is not clear which might the effective contribution of the sticking force due to the entrapped charge, and consequently the hold-down bias we applied to keep the switch activated was qualitatively imposed. Moreover, it seems that the current applied to the heater, as well as its waveform, can influence the reaching of a successful release. Because of these motivations we are currently investigating this aspect by performing measurements with different heating signals applied to the switches. Such measurements will be included in the final thesis and showed during the defense.

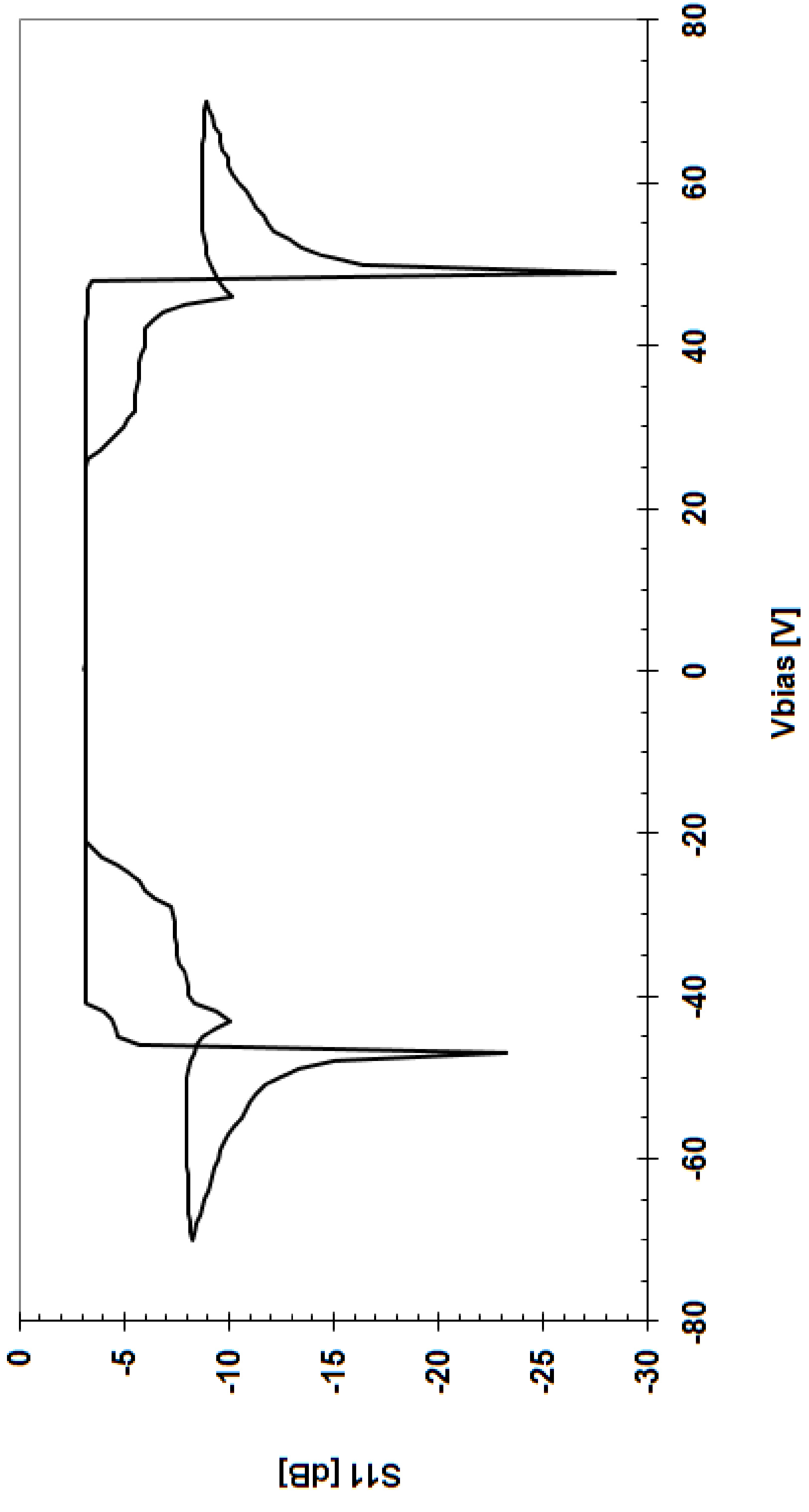

Figure 7.19: S_{11} parameter measured in response to a triangular bias (pull-in/pull-out) characteristic.

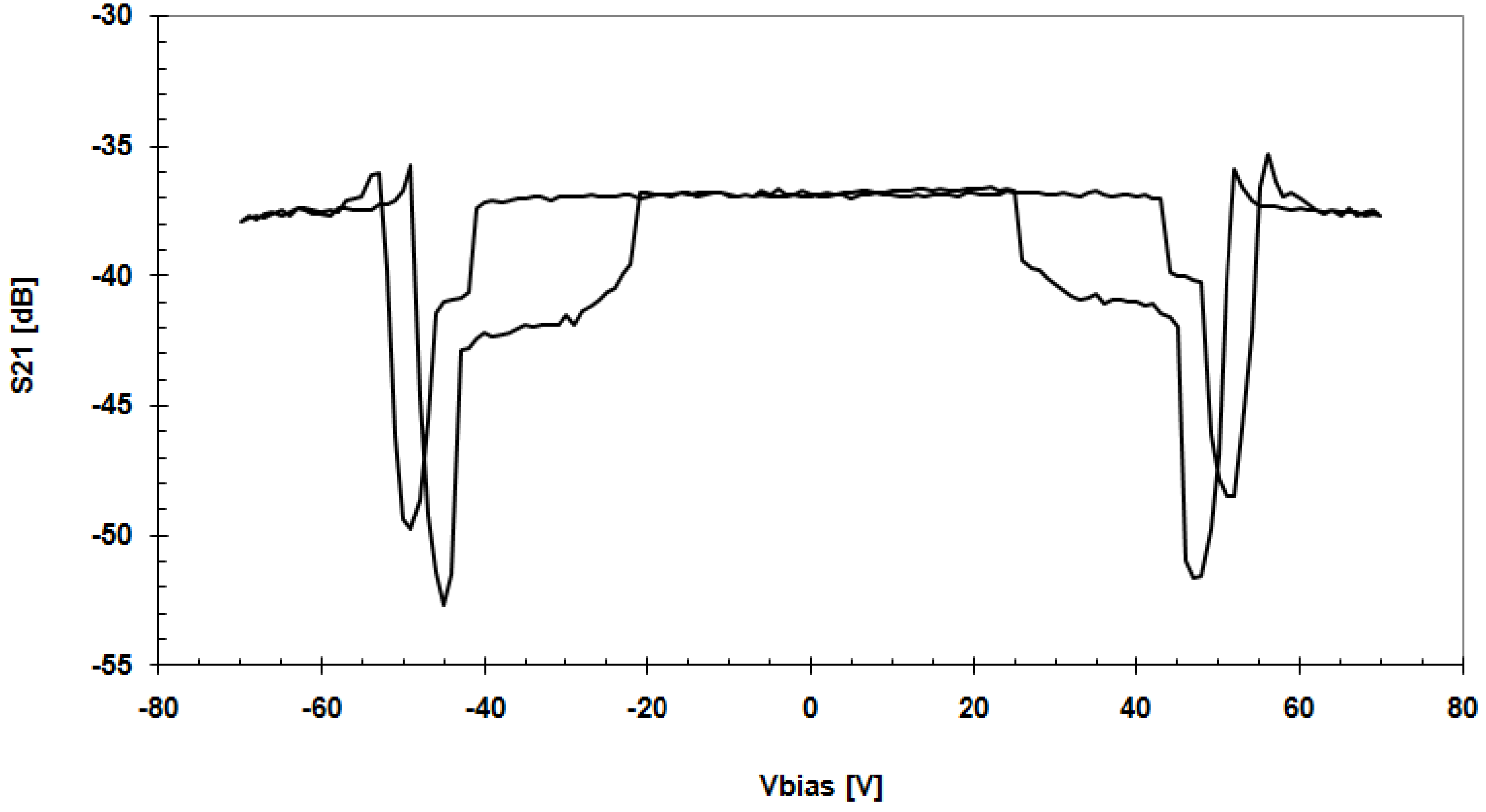

Figure 7.20: S_{21} parameter measured in response to a triangular bias (pull-in/pull-out) characteristic.

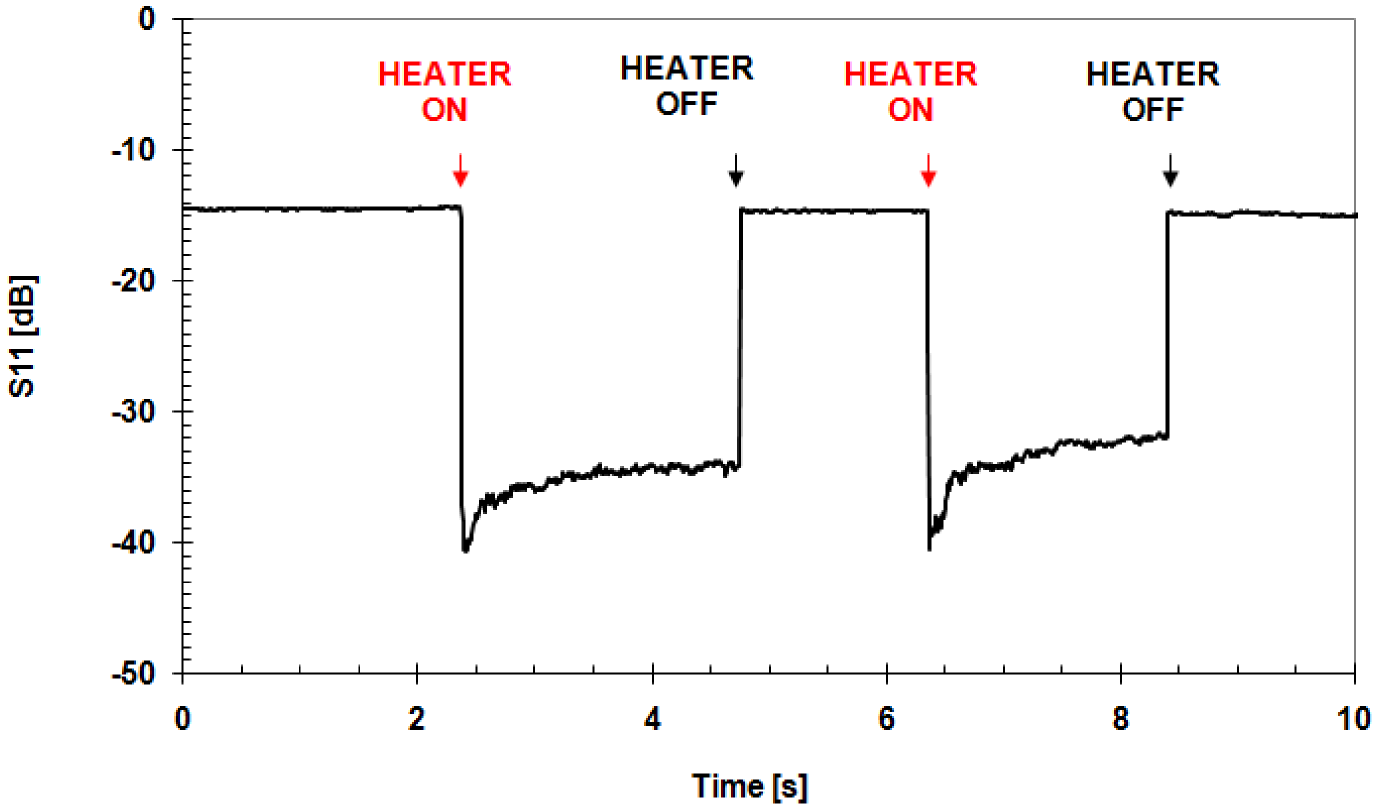

Figure 7.21: S_{11} measured characteristic vs. time when a current of 1 mA is driven into the heater and an hold-down DC bias of 27 V (beyond pull-out) is applied

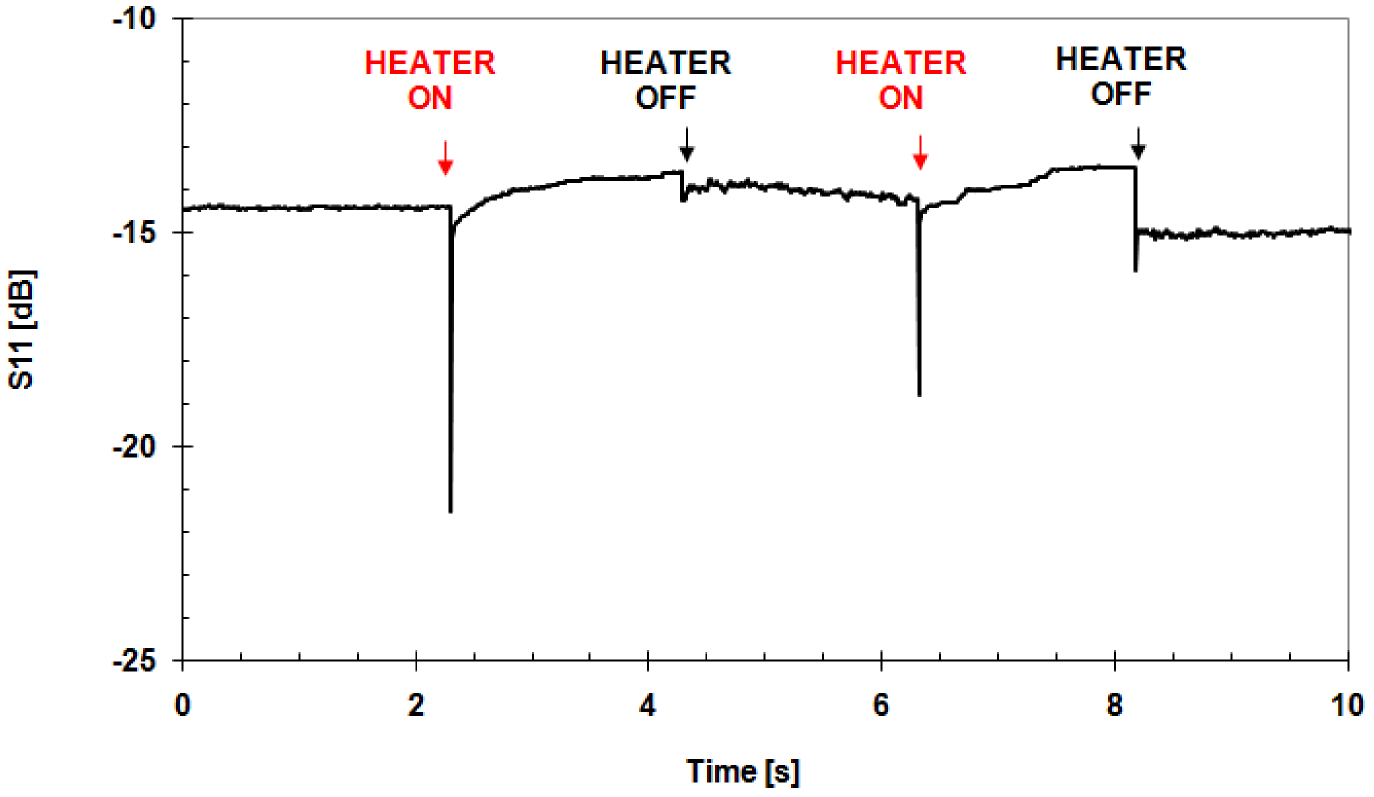

Figure 7.22: S_{11} measured characteristic vs. time when a current of 1.5 mA is driven into the heater and an hold-down DC bias of 27 V (beyond pull-out) is applied

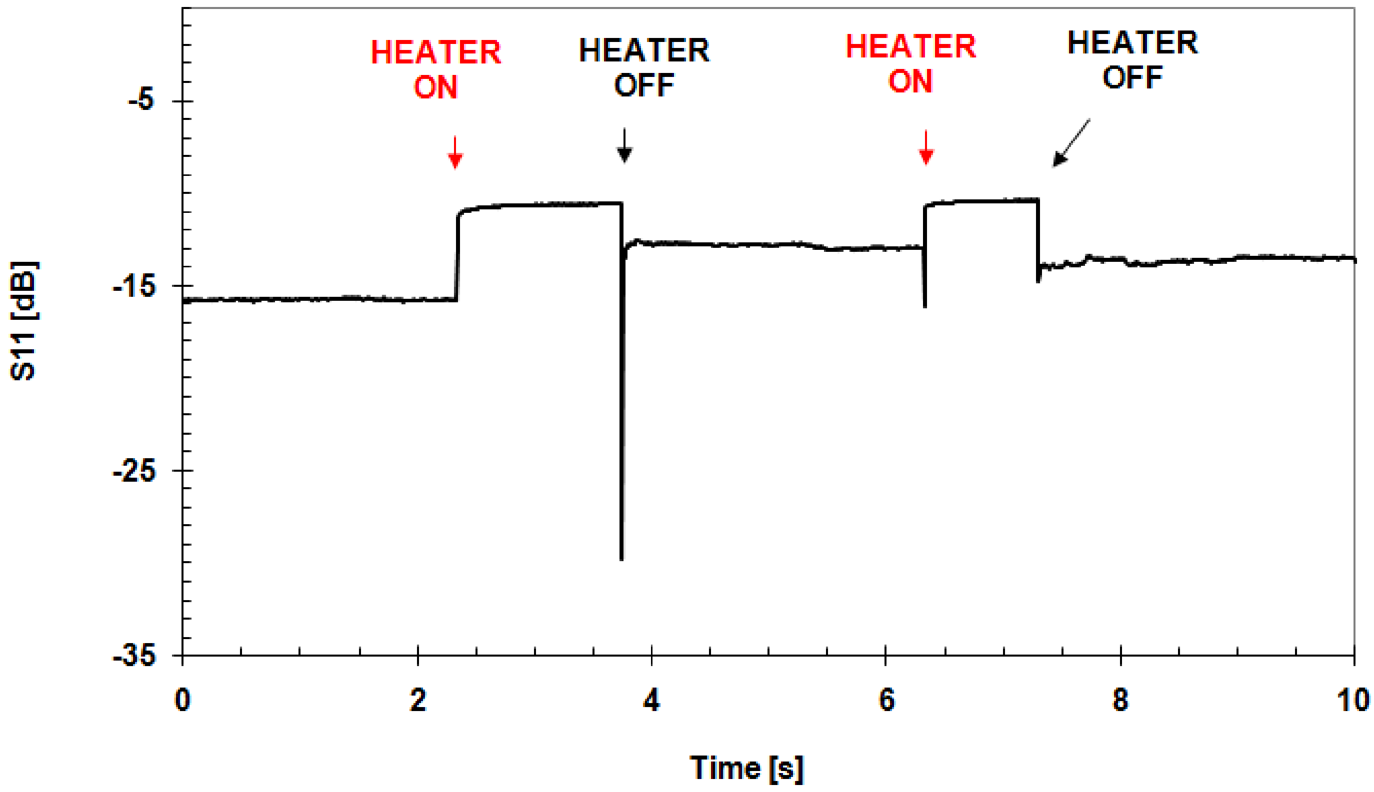

Figure 7.23: S_{11} measured characteristic vs. time when a current of 2 mA is driven into the heater and an hold-down DC bias of 27 V (beyond pull-out) is applied

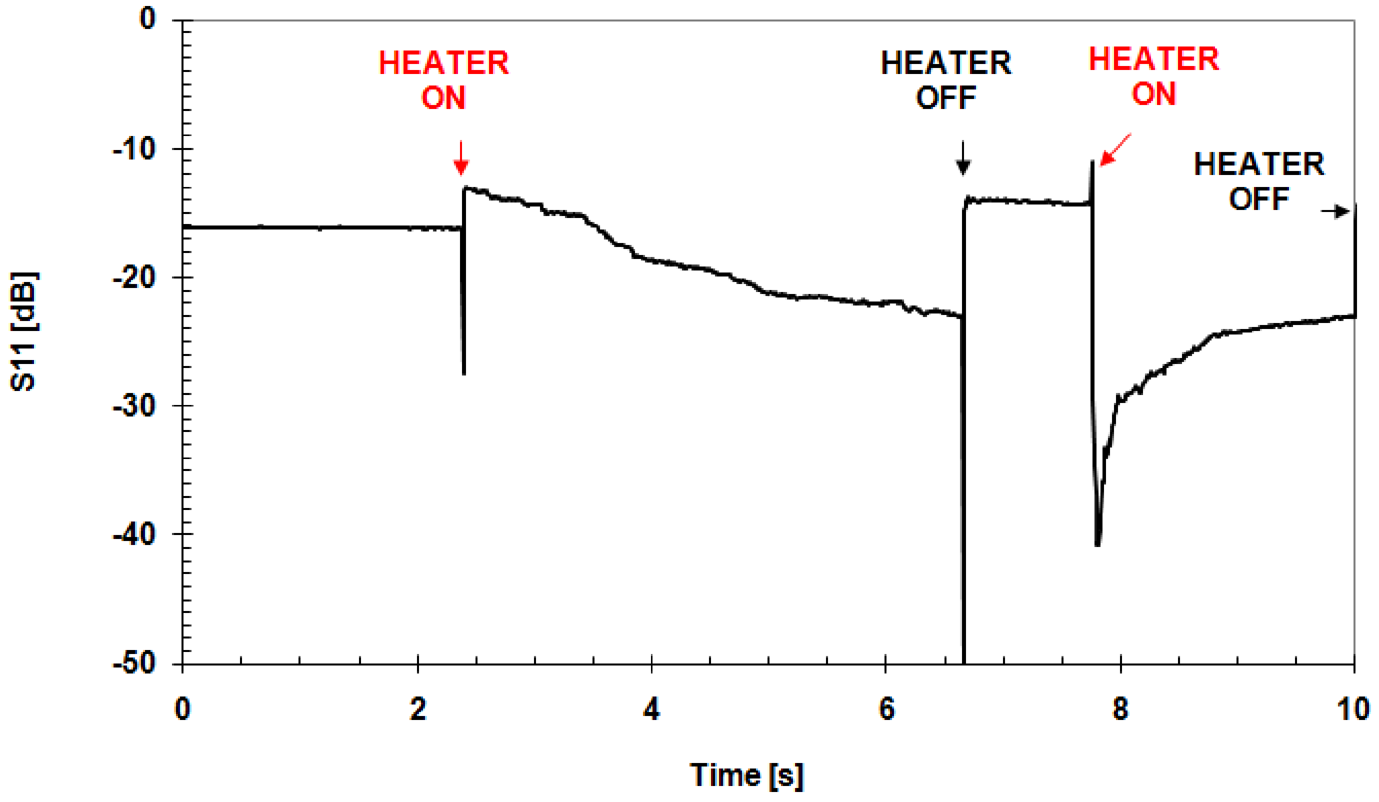

Figure 7.24: S_{11} measured characteristic vs. time when a current of 3 mA is driven into the heater and an hold-down DC bias of 27 V (beyond pull-out) is applied

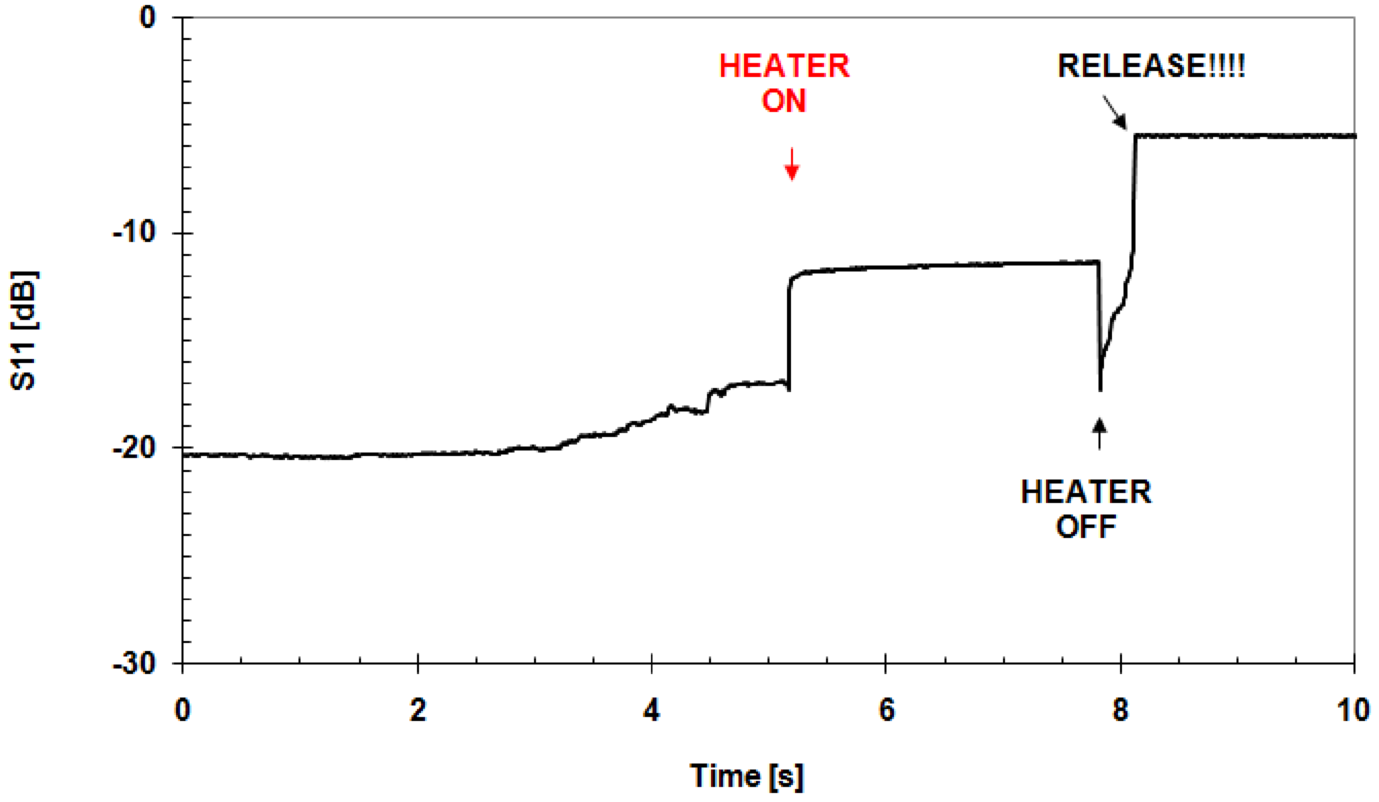

Figure 7.25: S_{11} measured characteristic vs. time when a current of 2 mA is driven into the heater and an hold-down DC bias of 25.5 V (slightly beyond pull-out) is applied

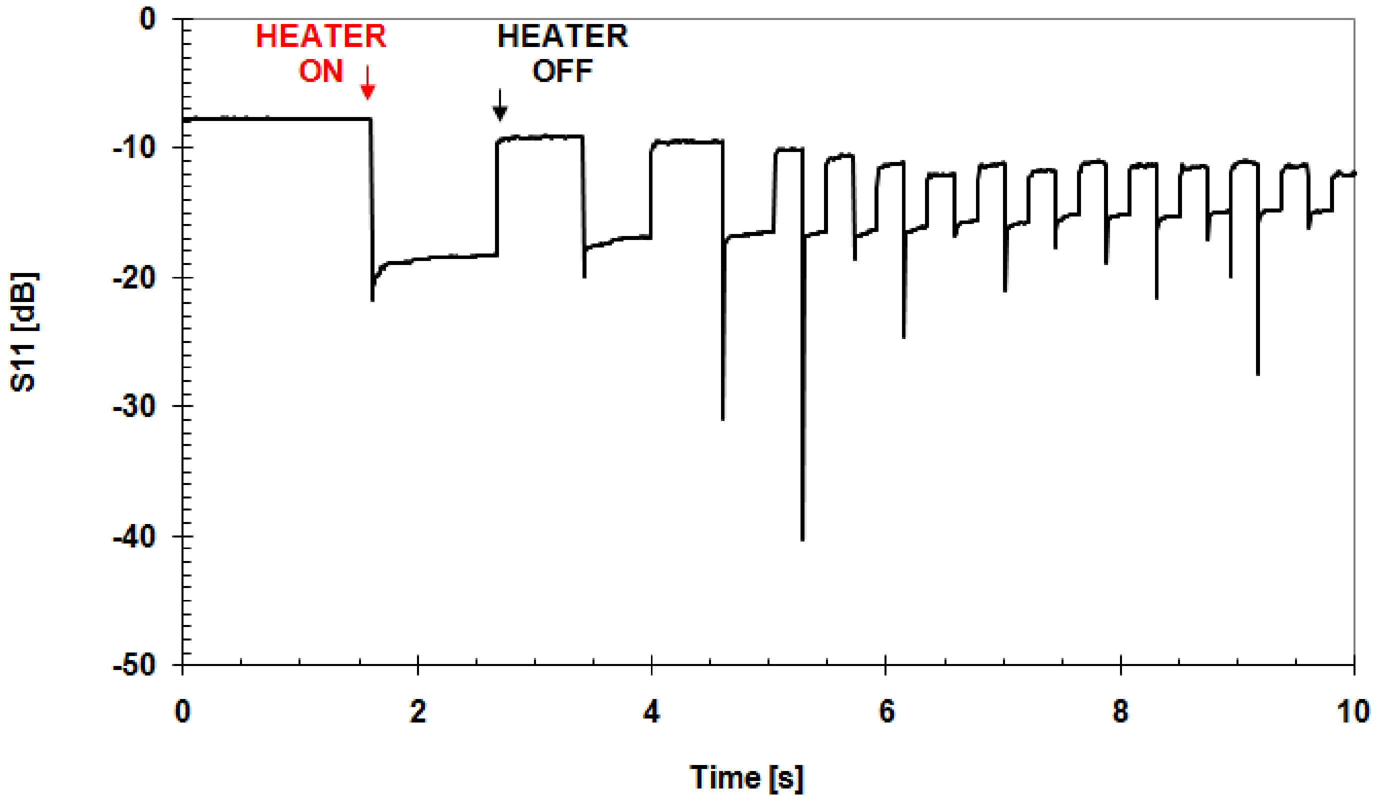

Figure 7.26: Measured S_{11} parameter characteristic when the current into the heater is pulsed ON and OFF several times.

7.3 Optical Profilometer Measurements

Additional measurements of the discussed RF-MEMS samples have been performed by means of a white light optical interferometer (WYKO NT1100 DMEMS by Veeco®, `www.veeco.com`). The RF-MEMS samples were stressed with a DC bias larger than the pull-in voltage up to more than 1 hour. Afterwards, the bias was removed, leaving the device stuck because of accumulated charge within the insulating layer. The natural evolution of the central stuck switch (i.e. without applying any heating current) was then monitored by scanning repeatedly the profile of the RF-MEMS device since the moment the DC signal was removed. Since the acquisition of a 3D profile requires a few seconds to be completed, the monitoring is not continuous over time, but the vertical quote of the switch is acquired every 20 seconds. This delay time between subsequent measurements was chosen in order to guarantee the profiling system to perform correctly the acquisition of each frame. On the other hand, when a heating current was applied, the DUT evolution was observed by the operator directly looking at the screen of the profiling system, and counting the time, from the heating mechanism activation, with a timer. The sudden release of a switch can easily be detected by observing the raw image from the interferometer microscope. Indeed, the variation of the central MEMS membrane vertical quote brings it out of focus, and the modification of the fringes configuration clearly indicates a vertical movement. Due to the measurement setup just discussed, the measured data are less rigorous compared to the ones presented before, where monitoring of the plate was completely automated and continuous in time. However, the measurements performed with the optical profiling system provide a further confirmation of the qualitative operation of the proposed heating mechanism. The 3D image of an RF-MEMS switch obtained with the interferometer is reported in Figure 7.27.

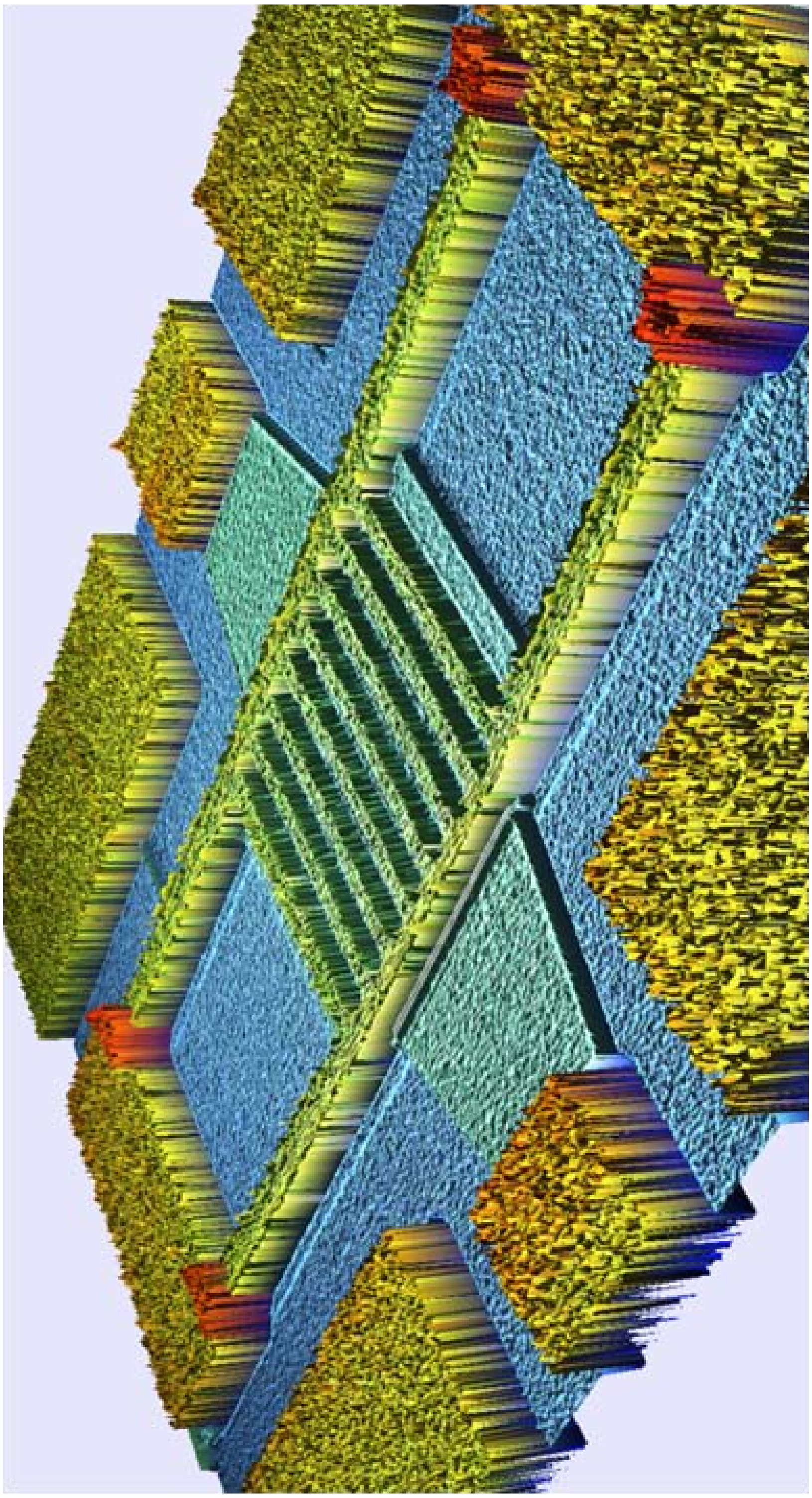

Figure 7.27: The image of the sample obtained with the interferometer and generated by the Veeco Vision®software during measurements.

Table 7.1: Summary of all the significant parameters concerning the measurements performed with the opitcal interferometer.

Applied DC biasing level	25-70 V
DC biasing time to reach stiction	1350-3800 sec
Time for the self release of the stuck switch	600-8000 sec
Serpentine resistance	30-40 kΩ
DC voltage applied to the serpentine	50-100 V
DC driven through the serpentine	1.25-3.3 mA
Time for the heat induced release	Instantaneous-60 sec

A few samples were measured. All the measurement characteristics are reported in Table 7.1. Thanks to the application of an heating current to the serpentine, most part of the analyzed samples released is a short time, up to 1 minute at most.

Concerning the natural evolution of a stuck switch (with no heating), Figure 7.28 reports one of the measured examples. In this case, the natural release of the switch took more than 2 hours. Moreover, after this time the switch did not recover yet its normal operation, as the central plate exhibits a sudden upward step to an intermediate level, between the rest and the actuated position. This indicates that the accumulated charge natural dispersion is a long process, that might lead to not acceptable times in order to restore the switch normal operation. On the other hand, the recovery time can be significantly decreased by activating the heating mechanism proposed in this thesis.

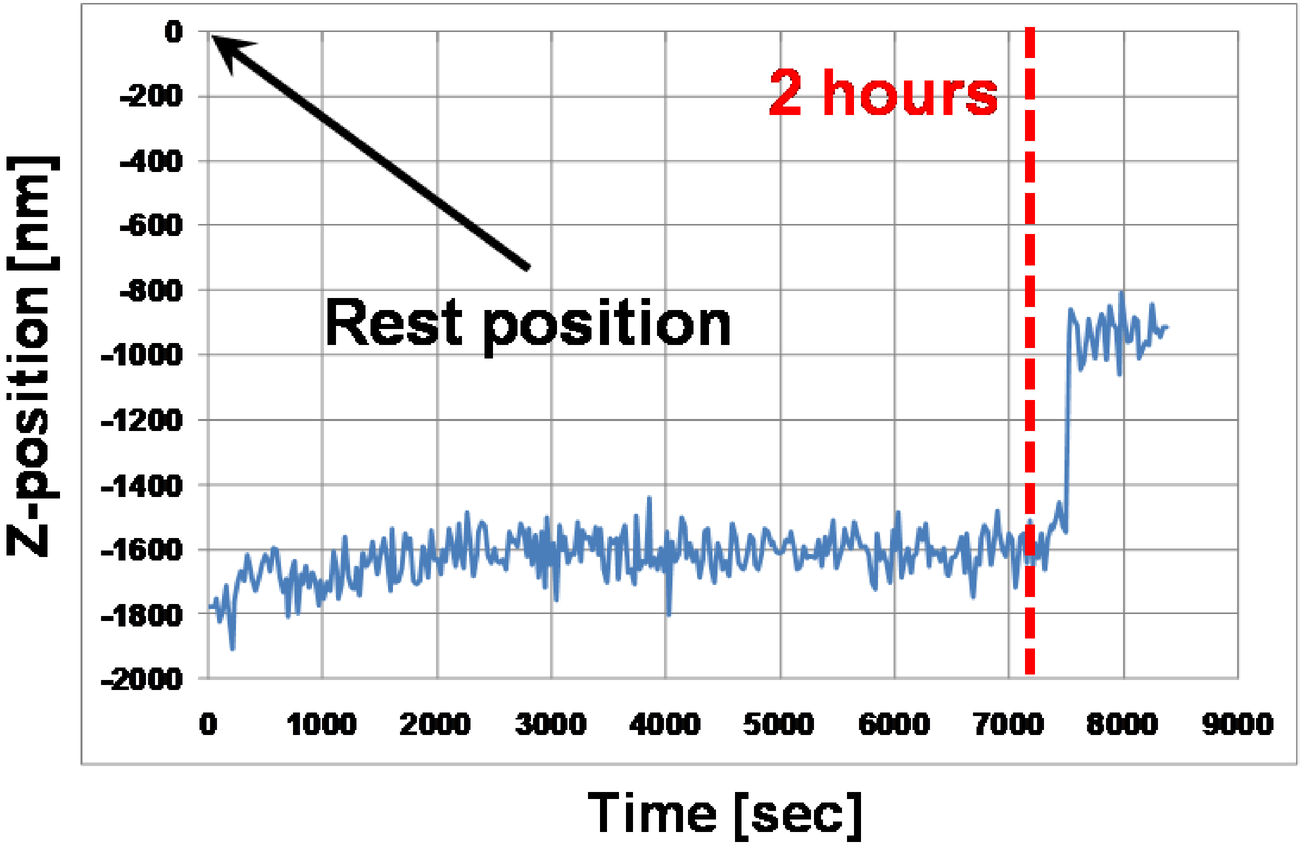

Figure 7.28: Natural evolution of one sample after it is brought to stiction. Since no heating current is applied, the entrapped charge takes more than 2 hours to escape till lowering the spurious bias below pull-out. However, not all the charge is gone, as the plate releases to an intermediate position that is not the initial one.

7.4 Central Plate Heater Measurements

In this section we report the results of experimental testing carried out on a few fabricated samples of the RF-MEMS varactor reported in Figure 5.7. All the data that are going to be shown have been collected by means of an optical profiling system based on interferometry (WYKO NT1100 DMEMS by Veeco®). The system can be used with a white light illuminator to capture the 3D static profile of MEMS devices. Moreover, it also allows observing the dynamic behaviour of the DUTs thanks to a pulsed stroboscopic illuminator synchronized, by a controlling PC, with the periodic biasing signal generated by an arbitrary waveform generator. First of all we wanted to determine the typical actuation and release voltages for the type of MEMS varactor discussed here. For this reason we performed measurements using the profilometer and applying a triangular voltage with zero mean value. The periodic stimulus was set to a very low frequency (20 Hz) in order to make all the dynamic effects, i.e. the MEMS switch inertia and the viscous gas-film damping, negligible. Figure 7.29 shows the pull-in/pull-out characteristic of one of the tested devices. The activation voltage is 10 V and the release voltage is 8 V. The same measurement was performed on other samples from the same fabrication batch. In some cases the pull-in and pull-out voltages are very close to the one visible in Figure 7.29. However, when dealing with samples coming from a different wafer, higher voltages (pull-in from 12 V up to 20 V) were measured. This discrepancy can be explained with a non-uniform thickness of the electrodeposited gold realizing the suspensions, as well as with a different distribution of the residual stress within the gold itself [19]. After determining the pull-in/pull-out characteristic, the DUTs are brought to stiction for charge accumulation by applying a DC bias level, higher than the pull-in voltage, for a certain period of time.

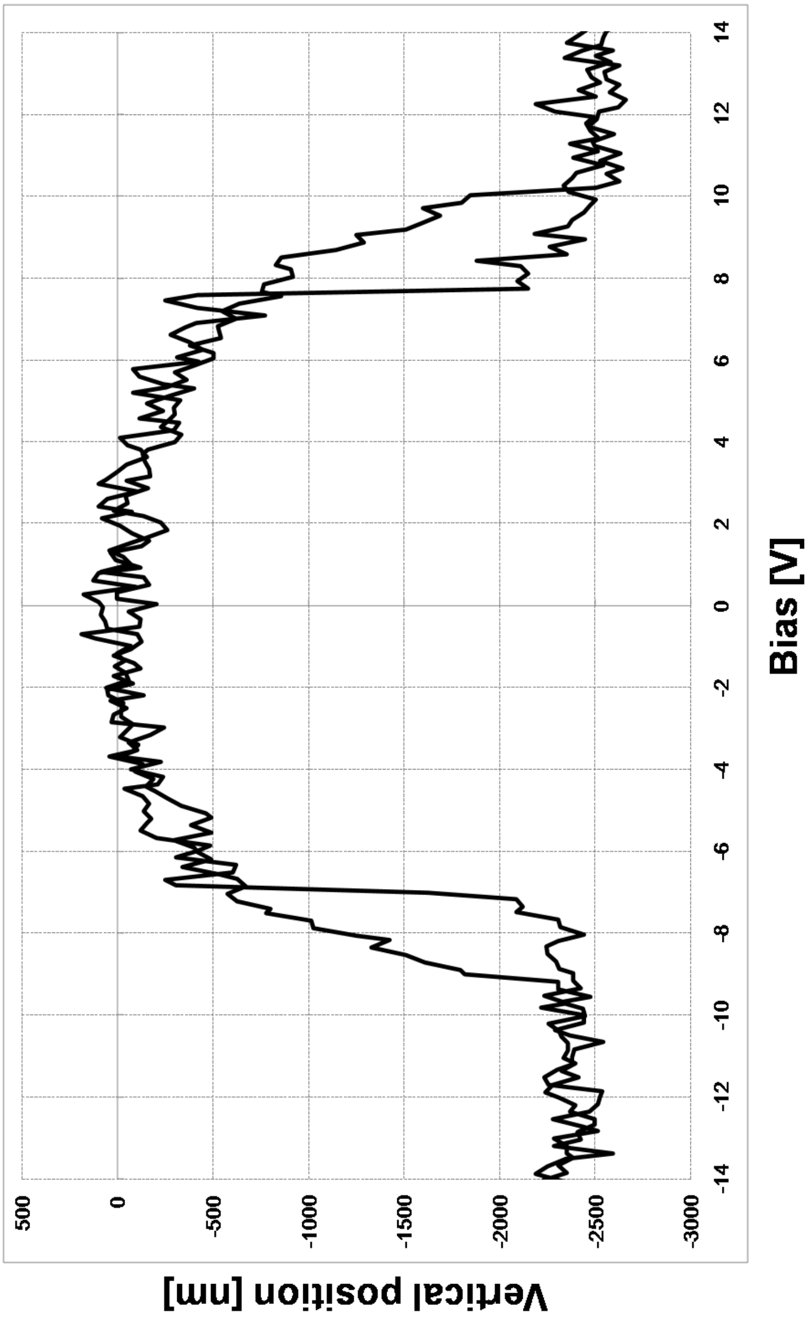

Figure 7.29: Experimental pull-in/pull-out characteristic of one of the tested MEMS varactors.

Subsequently, the bias signal is reduced to zero and a further 3D static profile of the switch is collected in order to verify its actual stiction. In case the switch does not release, a voltage is applied between the serpentine pads inducing a current through it, and the vertical quote is monitored in order to detect the release induced by heat generation. The just described testing procedure was applied to one of the samples that exhibited a pull-in/pull-out characteristic similar to the one reported in Figure 7.29. The 3D measured profile of the DUT is shown in Figure 7.30 where the fixed gold pads indicated by the arrows have been set as zero-height reference in the profilometer data processing software. This means that any vertical displacement of the central suspended plate is relative to this reference. Figure 7.31 shows the vertical quote of the switch, calculated by the profilometer software averaging all the measured points on the plate surface, depending on the measurement step as reported below.

- **Step 1** refers to the plate quote with respect of the reference (see Figure 7.30) measured when no controlling voltage is applied to the MEMS sample (rest position). The height is about 200 nm above the reference.

- **Step 2** reports the quote of the central plate measured right after applying 9 V DC (slightly higher than the pull-in voltage) for 4 minutes. In this case the averaged height is about 1.8 μm below the reference (negative value), indicating a plate total vertical displacement of about 2 μm with respect of the initial position. This profile was measured after the biasing level was already reduced to zero, thus indicating the presence of stiction induced by charge accumulation.

- **Step 3** concerns the 3D profile measured while a voltage of 100 V was applied between the serpentine input/output pads (see Figure 5.7) for a few seconds. Being the serpentine resistance of 57.3 KΩ, as previously determined by means of an I-V (current vs. voltage) measurement, the current flowing through it is 1.75 mA. The vertical height is very close to the one of Step 2.

- **Step 4** finally shows the plate averaged quote as it results from the 3D profile measurement performed a few seconds after the 100 V bias applied to the serpentine was removed. In this case the quote is about 400 nm below the reference, clearly indicating the plate release even if to an intermediate position if compared with the rest one (reported in Step 1).

The incomplete release observable in measurement Step 4 is very likely induced by a partial discharge of the silicon oxide layer. Indeed, despite the heated serpentine speeded up the charge dispersion, after a few seconds a certain amount of charge is still entrapped within the oxide, thus inducing a spurious bias level that is not anymore sufficient to keep the plate in the ON position, but is enough to maintain it in an intermediate position other then the initial one.

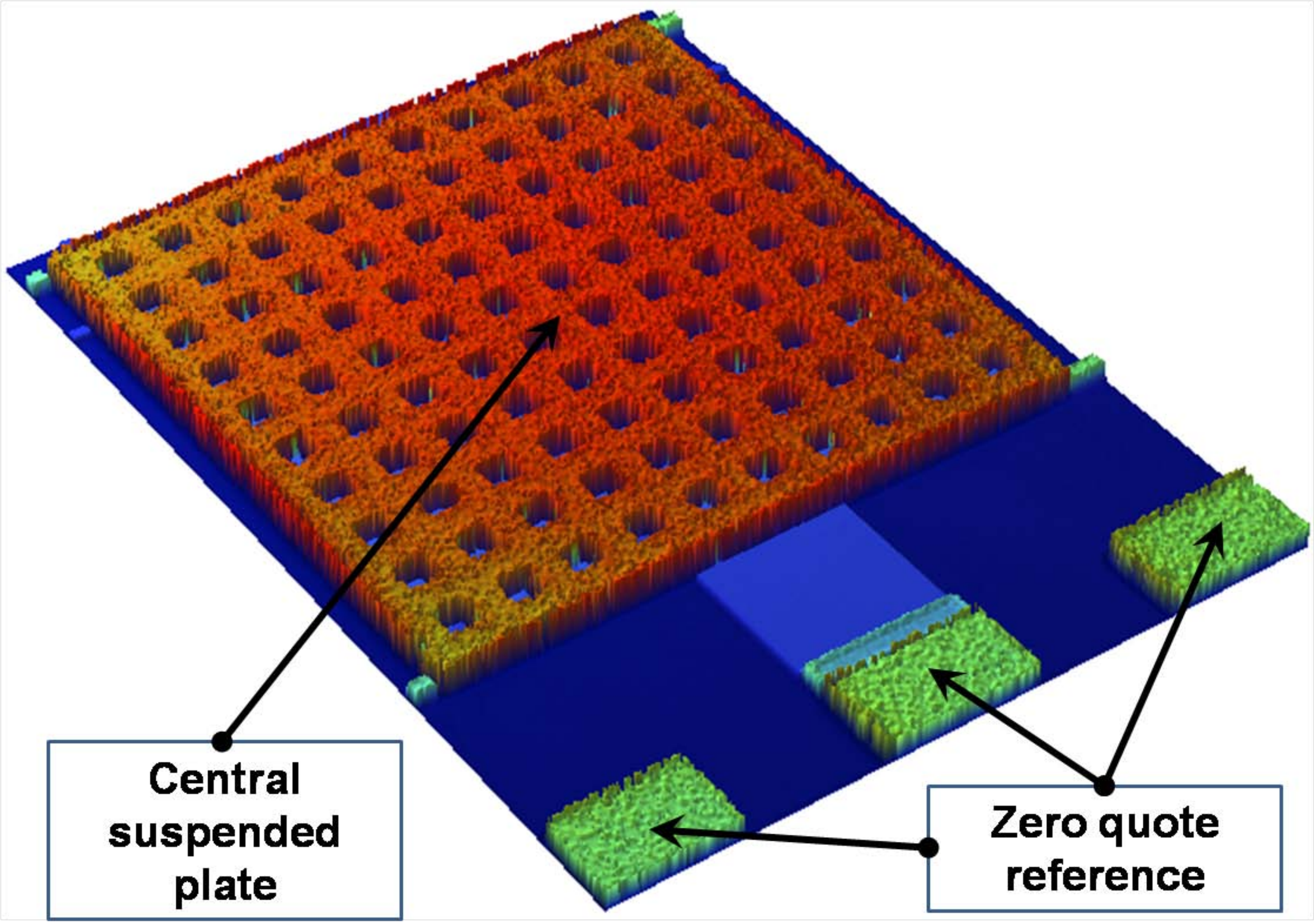

Figure 7.30: Measured 3D profile of the MEMS varactor sample that underwent the experimental procedure to induce the stiction and then restore it by means of the heating serpentine.

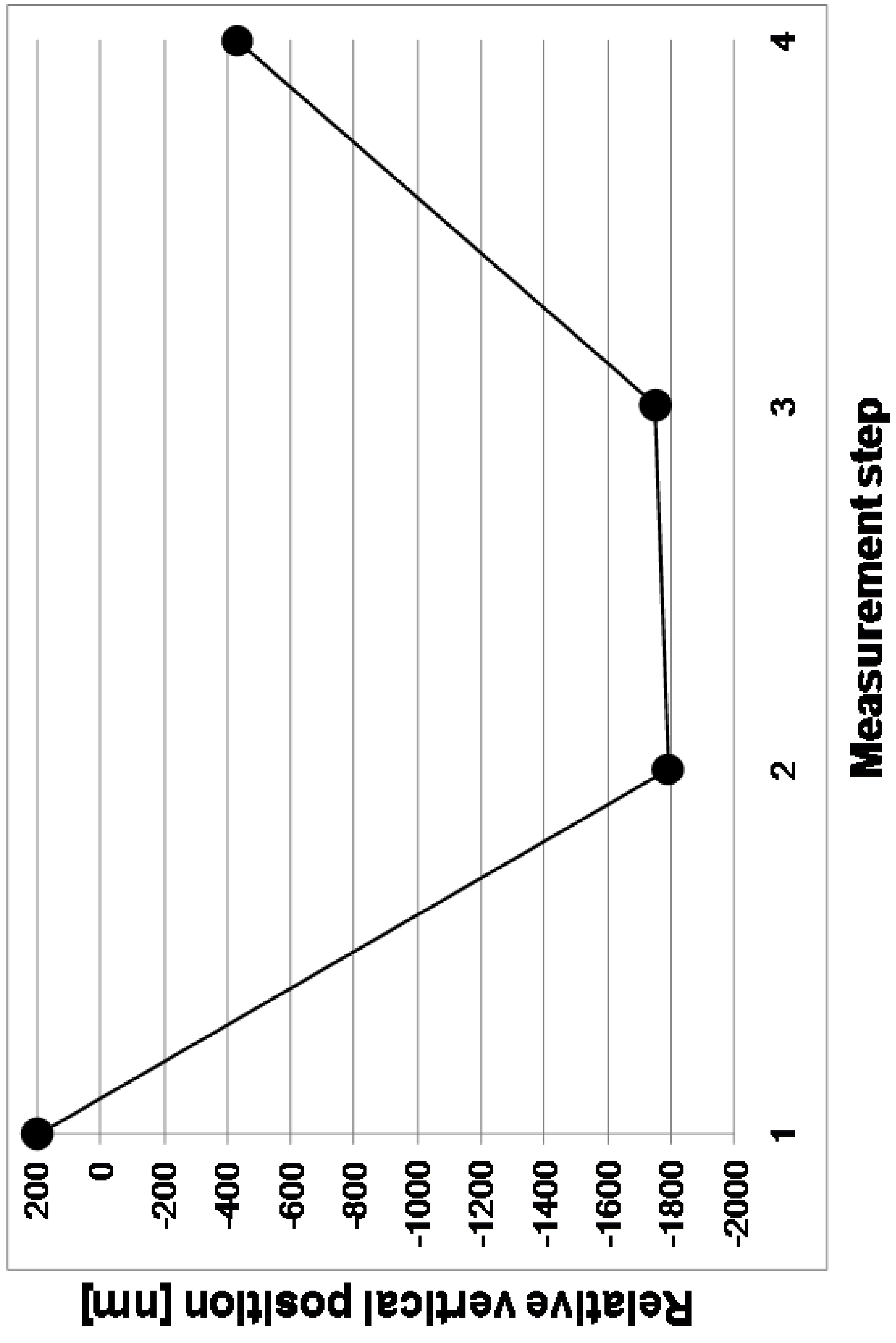

Figure 7.31: Averaged relative plate quote with respect to the reference shown in Figure 7.30. Step 1 refers to the rest position quote. Step 2 refers to the quote during stiction, Step 3 to the quote during heating and finally Step 4 to the quote after the release induced by the serpentine heating.

A few considerations concerning the just presented results are necessary. First of all, the fast release just discussed was not observed on all the tested devices. Few of them did not release after the serpentine heating but, instead, showed a further downward movement. The reason for this unexpected behaviour can be justified by considering that all the observed samples suffered from residual stress accumulated during the fabrication steps. Because of the gradient distribution of such stress, all the measured switches were not flat but a bit arched. Very likely, the heat induced by the serpentine released the stress within the gold, thus flattening the switch membranes and resulting in a further downward small displacement. On the other hand, the fact that for these samples the release induced by heating did not seem to work properly needs more discussion. Indeed, the measurements were performed manually and the voltage applied to drive the current through the serpentine was changed time after time without complying with any rigorous test plan. Because of this motivation, it is not possible to determine if the apparent malfunctioning of the heating mechanism is simply caused by a not proper heating stimulus. The same consideration poses another important issue. The heating mechanism, indeed, if overstressed with a too large current, would lead to an excessive heating of the suspended gold that might induce non-reversible deformations of the moveable structure and, consequently, to the alteration of the switch specifications (like pull-in voltage). This aspect could jeopardize the reliability of the MEMS switches and should be taken into account more carefully. In synthesis, the experimental data reported in this work have to be interpreted as the result of a preliminary investigation in order to prove the functionality of the active self-recovery mechanism. However, a more rigorous test plan is going to be setup, also relying on fully automated computer routines to perform batch measurements, in order to collect a larger amount of consistent experimental data on a wide range of MEMS switch specimens. Eventually, just to highlight how much the sticiton issue is critical for MEMS devices, we have to state that basically all the measured samples remained in the ON position after applying the bias for a time ranging from a few minutes up to 1 hour. When no heating is applied, the self-release takes place in a time ranging from several minutes up to a few hours. This explains how important the availability of an active self-release mechanism to be exploited in case of stiction is. To conclude this section on the experimental characterization of the RF-MEMS varactor discussed up to now, we report the measured RF behaviour (S-parameters). Figure 7.32 shows the reflection (S_{11}) and transmission (S_{21}) parameters of the switch in the not actuated state, while Figure 7.33 reports the reflection parameter (S_{11}) and isolation (S_{21}) of the same device in the actuated position.the OFF state capacitance is larger than expected and this causes the RF signal to encounter a lower impedance path to ground. On the other hand, the isolation in the MEMS switch ON state is rather good, being it better than 20 dB from 14 GHz up to 30 GHz (see Figure 7.33).

The attenuation introduced in the not actuated state is rather large, especially from 12 GHz and rising. This is partially caused by technology non-idealities in the through-oxide vias opening, as well as by a reduced vertical distance between the plate in rest position and the lower electrode, due to the residual stress within the gold of suspensions. As a consequence,the OFF state capacitance is larger than expected and this causes the RF signal to encounter a lower impedance path to ground. On the other hand, the isolation in the MEMS switch ON state is rather good, being it better than 20 dB from 14 GHz up to 30 GHz (see Figure 7.33).

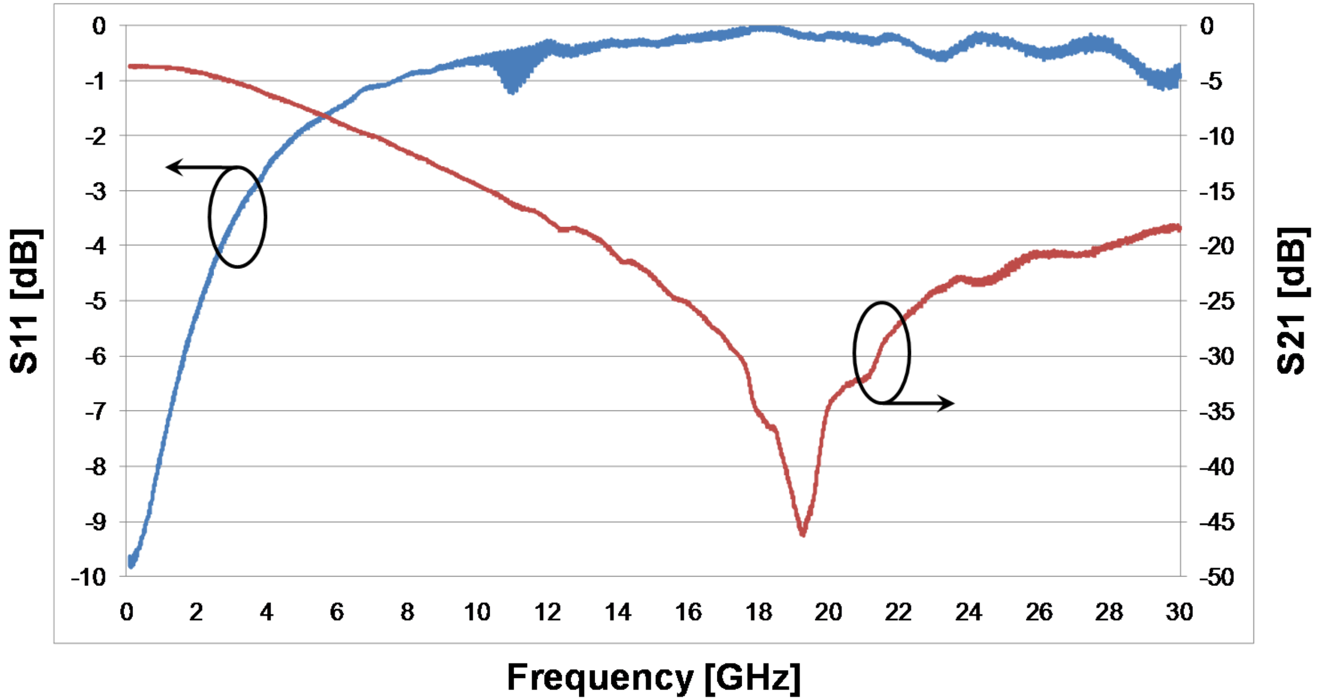

Figure 7.32: Measured reflection and transmission parameters (S_{11} and S_{21}, respectively) from 100 MHz up to 30 GHz for the RF-MEMS varactor in the not actuated position.

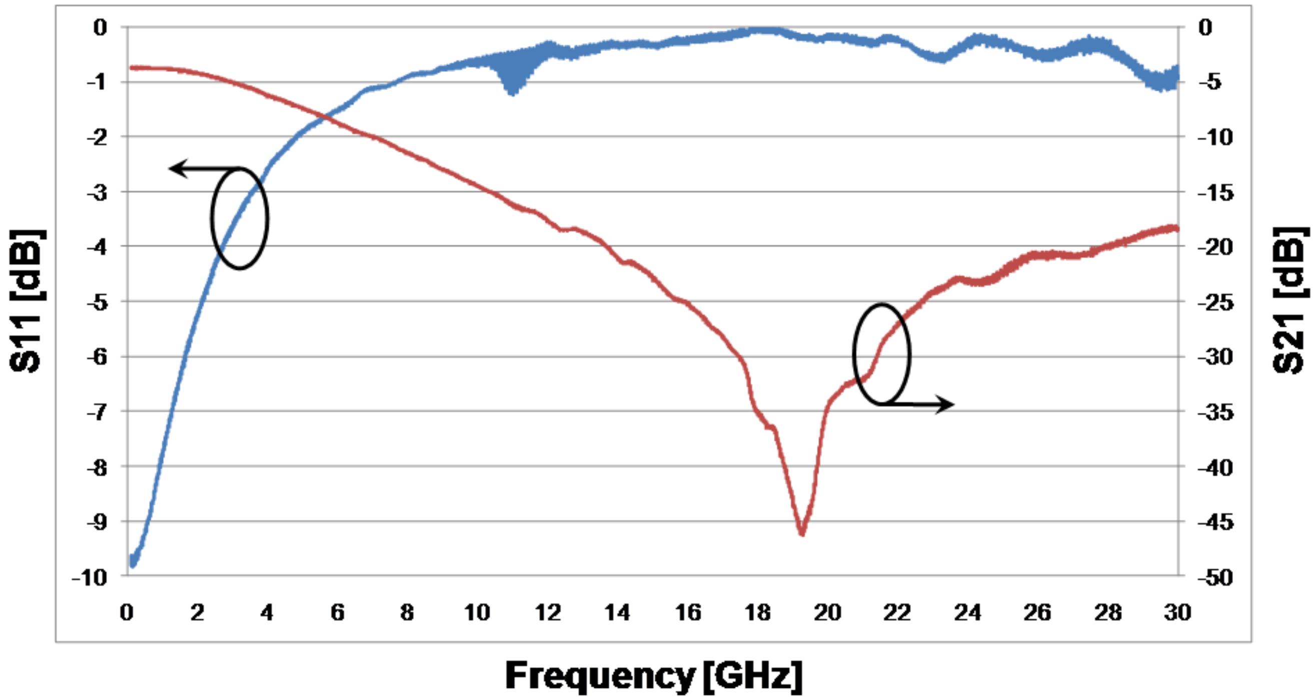

Figure 7.33: Measured reflection and isolation (S_{11} and S_{21}, respectively) from 100 MHz up to 30 GHz for the RF-MEMS varactor in the actuated position.

Chapter 8

Conclusions

This work is devoted to the implementation and characterization of a novel active self-recovery mechanism in order to retrieve the normal operation of RF-MEMS switches after a malfunctioning condition, due to stiction, occurs. The mechanism is based upon a high-resistivity polysilicon serpentine, deployed underneath the suspended bridge. When an electrical current is driven through it, the heat produced by the Joule effect increases the temperature of the entire structure, thus speeding up the entrapped charge dispersion. Besides that, the heat causes the thermal expansion of the stuck membrane, leading to the generation of restoring forces, which can counteract both the spurious bias due to the entrapped charge, and break micro-welding. Under the influence of both effects normal operation of the stuck RF-MEMS switch can be easily restored. In order to prove the effectiveness of proposed mechanism, the structural-thermo-electrical behavior of two different devices was studied via FEM-based simulations; the experimental results of a few fabricated samples from the different design group were reported as well. A few DUTs showed a rather fast release (from instantaneous up to a few seconds) thanks to the heating serpentine, after being intentionally brought to stiction because of accumulated charge. On the other hand, if the heater is not exploited, the self release of the switches takes a rather long time to occur (from several minutes up to a few hours) that, in any case, is incompatible with the requirements imposed by the most part of telecommunication standards. Moreover, the other effect of the novel mechanism has been observed. The data obtained during measurements clearly shows that the induced heat speed up the dispersion of charge accumulated in the dielectric layer, which is again contributing to the release of the stuck device and enables to restore its normal operation. An additional activity that is currently being set up is investigating if the developed mechanism is also effective against the micro-welding failure. At the same time the already established measurements are going on in order to collect more evidences of successful release as well as to determine the optimum operative condition of exploiting the mechanism within the RF-MEMS switches. Indeed, if the heating on one side speeds up the switch functionality recovery, an excessive heating would induce, on the other hand, a non-reversible structural alteration of its properties. MEMS ohmic devices with a topology similar to the one here reported will be tested for micro-welding stiction soon. In conclusion, the author believes that, despite the presence of significant contributions in literature concerning the anti-stiction measures that can be taken at technology level that have been mentioned in the Chapter 3, the employment of an active mechanism, like the one here discussed, that can be operated in case of malfunctioning, would make an RF-MEMS switch more robust versus the critical conditions previously discussed and, consequently, more reliable. And the main advantage of this approach is that it does not require a specific design and can be easily included in any already existing RF-MEMS ohmic/capacitive switch layout, without impairing its RF characteristics and performance.

Bibliography

[1] K. E. Petersen, "Silicon as a mechanical material," *Proceedings of the IEEE*, vol. 70, pp. 420–457, May 1982. 7, 8, 14

[2] A. V. Chavan and K. D. Wise, "Batch-processed vacuum-sealed capacitive pressure sensors," *IEEE Journal of Microelectromechanical Systems*, vol. 10, pp. 580–588, Dec. 2001. 8

[3] A. Choujaa, N. Tirole, C. Bonjour, G. Martin, D. Hauden, P. Blind, A. Cachard, and C. Pommier, "Ain/silicon lamb-wave microsensors for pressure and gravimetric measurements," *Sensors and Actuators A: Physical*, Jan.-Feb. 1995. 8

[4] M. A. Fonseca, J. M. English, M. von Arx, and M. G. Allen, "Wireless micromachined ceramic pressure sensor for high-temperature applications," *Journal of Microelectromechanical Systems*, vol. 11, pp. 337–343, Aug. 2002. 8

[5] N. A. Hall and F. L. Degertekin, "An integrated optical interferometric detection method for micromachined capacitive acoustic transducers," *Applied Physics Letters*, vol. 80, pp. 859–861, May 2002. 8

[6] A. K. Brown and Y. Lu, "Performance test results of an integrated gps/mems inertial navigation package," *Proceedings of the ION GNSS*, pp. 1–8, Sep. 2004. 8

[7] S. K. Nezhadian, G. Rezazadeh, and S. K. Arya, “Mems tunneling micro thermometer based ontip deflection of bimetallic cantilever beam,” *Sensors and Transducers Journal*, vol. 84, pp. 1660–1668, Oct. 2007. 8

[8] L. Lin, A. P. Pisano, and R. T. Howe, “A micro strain gauge with mechanical amplifier,” *IEEE/ASME Journal of Microelectromechanical Systems*, vol. 6, pp. 313–321, Dec. 1997. 8

[9] J. J. Neumann Jr. and K. J. Gabriel, “A fully-integrated cmos-mems audio microphone,” in *Proceeding of the 12th International Conference on Solid-State Sensors, Actuators and Microsystems (TRANSDUCERS)*, vol. 1, pp. 230–233, Jun. 2003. 8

[10] M. Niessner, W. Bedyk, G. Schrag, G. Wachutka, B. Margesin, and A. Faes, “Reduced-order modeling of capacitive mems microphones using mixed-level simulation,” in *Proceeding of the International Conference on Advanced Semiconductor Devices and Microsystems (ASDAM)*, pp. 283–286, Oct. 2006. 8

[11] H. Emmerich, M. Schofthaler, and U. Knauss, “A novel micromachined magnetic-field sensor,” in *Proceeding of the 12th International Conference on Micro Electro Mechanical Systems (MEMS)*, pp. 94 –99, Jan. 1999. 8

[12] J. M. Younse, “Mirrors on a chip,” *IEEE Spectrum*, vol. 30, pp. 27–31, Nov. 1993. 8

[13] S. Hirata, Y. Ishii, H. Matoba, and T. Inui, “An ink-jet head using diaphragm microactuator,” in *Proceeding of the 9th Annual International Workshop on Micro Electro Mechanical Systems (MEMS). An Investigation of Micro Structures, Sensors, Actuators, Machines and Systems.*, pp. 418–423, Feb. 1996. 8

[14] S. Kamisuki, M. Fujii, T. Takekoshi, C. Tezuka, and M. Atobe, "A high resolution, electrostatically-driven commercial inkjet head," in *Proceeding of the 13th Annual International Conference on Micro Electro Mechanical Systems (MEMS)*, pp. 793–798, Jan. 2000. 8

[15] O. Ohmichi, Y. Yamagata, and T. Higuchi, "Micro impact drive mechanisms using optically excited thermal expansion," *IEEE/ASME Journal of Microelectromechanical Systems*, vol. 6, pp. 200–207, Sep. 1997. 9

[16] F. C. M. Van de Pol, H. T. G. V. Lintel, M. Elwenspoek, and J. Fluitman, "A thermopneumatic micropump based on micro-engineering techniques," *Sensors and Actuators A: Physical*, vol. 21, pp. 198–202, Feb. 1990. 9

[17] C. A. Rich and K. D. Wise, "A high-flow thermopneumatic microvalve with improved efficiency and integrated state sensing," *IEEE/ASME Journal of Microelectromechanical Systems*, vol. 12, pp. 201–208, Apr. 2003. 9

[18] C. R. Neagu, J. G. E. Gardeniers, M. Elwenspoek, and J. J. Kelly, "An electrochemical microactuator: principle and first results," *Journal of Microelectromechanical Systems*, vol. 5, pp. 2–9, Mar. 1996. 9

[19] N. D. Mankame and G. K. Ananthasuresh, "Comprehensive thermal modelling and characterization of an electro-thermal-compliant microactuator," *Journal of Micromechanics and Microengineering*, vol. 11, pp. 452–462, Jul. 2001. 9

[20] R. d'Aparo, S. Orcioni, and M. Conti, "A digital controlled energy scavenger power converter," pp. 165–170, Jun. 2009. 10

[21] T. Kaya and H. Koser, “A new batteryless active rfid system: Smart rfid,” pp. 1–4, Sep. 2007. 10

[22] E. Dallago, D. Miatton, G. Venchi, G. Frattini, and G. Ricotti, “Self-supplied integrable active high-efficiency ac-dc converter for piezoelectric energy scavenging systems,” pp. 1633–1636, May 2007. 10

[23] P.-H. Wang, X.-H. Dai, X.-L. Zhao, and L.-J. Niu, “Electromagnetic self-powered low-level vibration energy scavenger with microelectroplated nickel resonator,” *Electronics Letters*, vol. 45, pp. 832–833, 30 2009. 10

[24] R. D’hulst, T. Sterken, P. Fiorini, R. Puers, and J. Driesen, “Energy scavengers : Modeling and behavior with different load circuits,” pp. 2169–2174, Nov. 2007. 10

[25] V. Leonov, P. Fiorini, S. Sedky, T. Torfs, and C. Van Hoof, “Thermoelectric mems generators as a power supply for a body area network,” vol. 1, pp. 291–294, Jun. 2005. 10

[26] T. Becker, M. Kluge, J. Schalk, T. Otterpohl, and U. Hilleringmann, “Power management for thermal energy harvesting in aircrafts,” pp. 681–684, Oct. 2008. 10

[27] V. Leonov, C. Van Hoof, and R. J. M. Vullers, “Thermoelectric and hybrid generators in wearable devices and clothes,” pp. 195–200, Jun. 2009. 10

[28] J. A. Potkay and K. Brooks, “An arterial cuff energy scavenger for implanted microsystems,” pp. 1580–1583, May 2008. 10

[29] J. J. Allen, *Micro Electro Mechanical System Design*. Taylor and Francis Group, LLC, 2005. 11

[30] R. C.Jaeger, *Introduction to Microelectronic Fabrication.* Addison-Wesley Publishing Company, Inc., 1988. 12, 13

[31] R. Jones and M. Chapman, “Rf mems in mobile phones,” *RF Design Magazine*, pp. 20–26, Sep. 2005. 21

[32] G. Bazin, J. P. Gilles, P. Crozat, and S. Megherbi, “Rf mems: Silicon micro-mechanical capacitive structures,” pp. 1–4, Oct. 2000. 23

[33] Y. Zhang, G. Ding, X. Shun, X. Li, and B. Cai, “Design and analysis of the micromechanical structure for an electromagnetic bistable rf mems switch,” vol. 1, pp. 1–4, Dec. 2005. 23

[34] Hee-Chul Lee, Jae-Yeong Park, and Jong-Uk Bu, “Piezoelectrically actuated rf mems dc contact switches with low voltage operation,” *Microwave and Wireless Components Letters, IEEE*, vol. 15, pp. 202–204, Apr. 2005. 23

[35] J. Gaspar, V. Chu, N. Louro, R. Cabeca, and J. P. Conde 23

[36] P. Robert, D. Saias, C. Billard, S. Boret, N. Sillon, C. Maeder-Pachurka, P. L. Charvet, G. Bouche, P. Ancey, and P. Berruyer, “Integrated rf-mems switch based on a combination of thermal and electrostatic actuation,” vol. 2, pp. 1714–1717, Jun. 2003. 23

[37] I. Cho, T. Song, S. Baek, and E. Yoon, “A low-voltage and low-power rf mems series and shunt switches actuated by combination of electromagnetic and electrostatic forces,” *IEEE Transactions on Microwave Theory and Techniques*, vol. 53, pp. 2450–2457, Jul. 2005. 23

[38] T. Ikehashi, T. Ohguro, E. Ogawa, H. Yamazaki, K. Kojima, M. Matsuo, K. Ishimaru, and H. Ishiuchi, “A robust rf mems variable capacitor with piezoelectric and electrostatic actuation,” pp. 39–42, Jun. 2006. 23

[39] J. Burghartz, A. Ruehli, K. Jenkins, M. Soyuer, and D. Nguyen-Ngoc, “Novel substrate contact structure for high-q silicon-integrated spiral inductors,” in *Electron Devices Meeting, 1997. IEDM ’97. Technical Digest., International*, pp. 55 – 58, 7-10 1997. 25

[40] J. Wang, J. Cai, X. Dou, and S. Wang, “Integrated inductors on silicon and planarized ceramic substrates,” in *Electronic Packaging Technology High Density Packaging, 2009. ICEPT-HDP ’09. International Conference on*, pp. 504 – 507, 2009. 26

[41] J. Iannacci and R. Gaddi, *Mixed-Domain Simulation and Wafer-Level Packaging of RF-MEMS Devices.* Lambert Academic Publishing - LAP. Currently in press (May 2010). 28, 32

[42] K. Topalli, M. Unlu, O. Civi, S. Demir, S. Koc, and T. Akin, “A monolithic phased array using 3-bit dmtl rf mems phase shifters,” in *Proceeding of the International Symposium of the Antennas and Propagation Society*, pp. 517–520, Jul. 2006. 28

[43] B. Pillans, S. Eshelman, A. Malczewski, J. Ehmke, and C. Goldsmith, “Ka-band rf mems phase shifters,” *Microwave and Guided Wave Letters, IEEE*, vol. 9, pp. 520–522, Dec. 1999. 28

[44] H. J. De Los Santos, *RF Mems Circuit Design for Wireless Communications.* Artech House, 2002. 28

[45] L. Larcher, R. Brama, M. Ganzerli, J. Iannacci, B. Margesin, M. Bedani, and A. Gnudi, “A mems reconfigurable quad-band class-e power amplifier for gsm standard,” in *Proceeding of the 22nd International Conference on Micro Electro Mechanical Systems (MEMS)*, pp. 864–867, Jan. 2009. 28

[46] M. Daneshmand and R. R. Mansour, “Redundancy rf mems multiport switches and switch matrices,” *IEEE ASME Journal of MEMS*, vol. 16, pp. 296–303, Apr. 2007. 28

[47] K. Gilleo, “Mems packaging solutions,” *EP and P*, pp. 49–56, Jun. 2000. 29

[48] V. Vijay, K. A. Jose, and U. Zoelzer, *RF-Mems and Their Applications*. John Wiley and Sons Inc., 2003. 29

[49] Y.-K. Park, H.-W. Park, D.-J. Lee, J.-H. Park, I.-S. Song, C.-W. Kim, C.-M. Song, Y.-H. Lee, C.-J. Kim, and B.-K. Ju, “A novel low-loss wafer-level packaging of the rf-mems devices,” pp. 681–684, Jan. 2002. 29

[50] H. A. C. Tilmans, H. Ziad, H. Jansen, O. Di Monaco, A. Jourdain, W. De Raedt, X. Rottenberg, E. De Backer, A. Decaussemaeker, and K. Baert, “Wafer-level packaged rf-mems switches fabricated in a cmos fab,” *Technical Digest of the International Electron Devices Meeting (IEDM)*, pp. 41.4.1–41.4.4, Dec. 2001. 30

[51] A. Margomenos, D. Peroulis, K. J. Herrick, and L. P. B. Katehi, “Silicon micromachined packages for rf mems switches,” pp. 1–4, Sep. 2001. 30

[52] F. Niklaus, P. Enoksson, P. Griss, E. Kalvesten, and G. Stemme, “Low-temperature wafer-level transfer bonding,” *IEEE/ASME Journal of Microelectromechanical Systems*, vol. 10, pp. 525–531, Dec. 2001. 30

[53] R. C. Jaeger, *Microelectronic Circuit Design*. Upper Saddle River, NJ, USA: McGraw-Hill, 2003. 30, 31

[54] J. Tian and M. Bartek, “Low temperature wafer-level packaging of rf-mems using su-8 printing,” pp. 56–59, Nov. 2005. 30

[55] F. W. Kear, *Hybrid Assemblies and Multichip Modules.* Marcel Dekker Editor, 1993. 31

[56] N. C. Tu-Cuong, *Micromechanical Signal Processors.* University of California at Berkeley, CA, USA: Ph. D. Dissertation in Engineering-Electrical Engineering and Computer Science, 1994. 31

[57] Y. Jin, Z. Wang, L. Zhao, P. C. Lim, J. Wei, and C. KhuenWong, “Zr/v/fe thick film for vacuum packaging of mems,” *Journal of Micromechanics and Microengineering*, vol. 14, pp. 687–692, May 2004. 32

[58] C. Benvenuti, “Non-evaporable getters: from pumping strips to thin film coatings,” Jun. 1998. 32

[59] D. Sparks, S. Massoud-Ansari, and N. Najafi, “Reliable vacuum packaging using nanogetterstm and glass frit bonding,” vol. 5343, Jan. 2004. 32

[60] O. Brand et al., *Reliability of MEMS.* John Wiley and Sons, 2007. 35

[61] C. L. Muhlstein, S. B. Brown, and R. O. Ritchie, “High-cycle fatigue of single-crystal silicon thin films,” *IEEE/ASME Journal of Microelectromechanical Systems*, vol. 10, pp. 593–600, Dec. 2001. 36

[62] W. N. Sharpe and J. Bagdahn, “Fatigue testing of polysilicon - a review,” *Mechanics and Materials*, vol. 38, pp. 3–11, Jan. 2004. 36

[63] R. Chan, R. Lesnick, D. Becher, and F. Milton, “Low-actuation voltage rf mems shunt switch with cold switching lifetime of seven billion cycles,” *IEEE/ASME Journal of Microelectromechanical Systems*, vol. 12, pp. 713–719, Oct. 2003. 36

[64] H. S. Newman, J. L. Ebel, D. Judy, and J. Maciel, “Lifetime measurements on a high-reliability rf-mems contact switch,” *IEEE Microwave and Wireless Components Letters*, vol. 18, pp. 100–102, Feb. 2008. 36

[65] M. Fernandez-Bolanos, D. Tsamados, P. Dainesi, and A. Ionescu, “Reliability of rf mems capacitive switches and distributed mems phase shifters using aln dielectric,” pp. 638–641, Jan. 2009. 36

[66] T. Harder, T.-J. Yao, Q. He, C.-Y. Shih, and Y.-C. Tai, “Residual stress in thin-film parylene-c,” pp. 435–438, Jan. 2002. 37

[67] J. B. Rizk, E. Chaiban, and G. Rebeiz, “Steady state thermal analysis and high-power reliability considerations of rf mems capacitive switches,” pp. 239–242, Jun. 2002. 37

[68] J. Ruan, N. Nolhier, M. Bafleur, L. Bary, F. Coccetti, T. Lisec, and R. Plana, “Electrostatic discharge failure analysis of capacitive rf mems switches,” *Elsevier Microelectronics Reliability*, vol. 47, pp. 1818–1822, Sep.-Nov. 2007. 37

[69] A. Tazzoli, V. Peretti, and G. Meneghesso, “Electrostatic discharge and cycling effects on ohmic and capacitive rf-mems switches,” *IEEE Transactions on Device and Materials Reliability*, vol. 7, pp. 429–437, Sep. 2007. 37

[70] D. Becher, R. Chan, M. Hattendorf, and M. Feng, “Reliability study of lowvoltage rfnems switches,” pp. 54–58, Apr. 2002. 37

[71] Y. Yee, K. Chun, J. D. Lee, and C. Kim, “Polysilicon surface-modification technique to reduce sticking of microstructures,” *Sensors and Actuators A: Physical*, vol. 52, pp. 145–150, Mar.-Apr. 1996. 38, 47

[72] P. F. Man, B. P. Gogoi, and C. H. Mastrangelo, "Elimination of post-release adhesion in microstructures using conformal fluorocarbon coatings," *IEEE/ASME Journal of Microelectromechanical Systems*, vol. 6, pp. 25–34, Mar. 1997. 38

[73] F. Solazzi, A. Tazzoli, P. Farinelli, A. Faes, V. Mulloni, G. Meneghesso, and B. Margesin, "Active recovering mechanism for high performance rf mems redundancy switches," in *Accepted to IEEE European Microwave Conference, Paris*, Sep. 2010. 38, 50

[74] V. Gupta, R. Snow, M. C. Wu, A. Jain, and J. che Tsai, "Recovery of stiction-failed mems structures using laser-induced stress waves," *IEEE/ASME Journal of Microelectromechanical Systems*, vol. 13, pp. 696–700, Aug. 2004. 38, 51

[75] W. R. Ashurst, C. Yau, C. Carraro, R. Maboudian, and M. T. Dugger, "Dichlorodimethylsilane as an anti-stiction monolayer for mems: a comparison to the octadecyltrichlorosilane self-assembled monolayer," *IEEE/ASME Journal of Microelectromechanical Systems*, vol. 10, pp. 41–49, Mar. 2001. 39

[76] S.-H. Lee, M.-J. Kwon, J.-G. Park, Y.-K. Kim, and H.-J. Shin, "The surface modification with fluorocarbon thin films for the prevention of stiction in mems," pp. 143–148, Apr. 1998. 39

[77] S. A. Smallwood, K. C. Eapen, S. T. Patton, and J. S. Zabinski, "Performance results of mems coated with a conformal dlc," *Elsevier Wear*, vol. 260, pp. 1179–1189, Jun. 2006. 39

[78] S. A. Henck, "Lubrication of digital micromirror devices," *Tribology Letters*, vol. 3, p. 239247, Sep. 1997. 39

[79] G. M. Rebeiz, *RF MEMS: Theory, Design, Technology*. Hoboken, NJ, USA: Wiley Interscience, 2002. 41, 42, 46, 55, 111

[80] G. J. Papaioannou and J. Papapolymerou, "Dielectric charging mechanisms in rf-mems capacitive switches," pp. 359–362, Oct. 2007. 42

[81] G. J. Papaioannou, M.-N. Exarchos, V. Theonas, W. Guoan, and J. Papapolymerou, "Temperature study of the dielectric polarization effects of capacitive rf mems switches," *IEEE Transactions on Microwave Theory and Techniques*, vol. 53, p. 34673473, Nov. 2005. 42

[82] G. Papaioannou, E. Papandreou, J. Papapolymerou, and R. Daigler, "Dielectric discharging processes in rf-mems capacitive switches," pp. 1–4, Dec. 2007. 42

[83] L. Sun, L. Wang, W. Rong, and L. Chen, "Considering van der waals forces in micromanipulation design," pp. 2507 –2512, Aug. 2007. 43

[84] H. C. Lee, J. H. Park, and Y. H. Park, "Development of shunt type ohmic rf mems switches actuated by piezoelectric cantilever," *Sensors and Actuators A: Physical*, vol. 136, pp. 282–290, May 2007. 45

[85] K. Grenier, D. Dubuc, B. Ducarouge, V. Conedera, D. Bourrier, E. Ongareau, P. Derderian, and R. Plana, "High power handling rf mems design and technology," pp. 155–158, Jan.-Feb. 2005. 45

[86] J. Schimkat, "Contact materials for microrelays," pp. 190–194, Jan. 1998. 48

[87] J. Park, E. S. Shim, W. Choi, Y. Kim, Y. Kwon, and D. Cho, "A non-contact-type rf mems switch for 24-ghz radar applications," *Journal of Microelectromechanical Systems*, vol. 18, pp. 163–173, Feb. 2009. 48

[88] H. Yamazaki, T. Ikehashi, T. Ohguro, E. Ogawa, K. Kojima, K. Ishimaru, and H. Ishiuchi, "An intelligent bipolar actuation method with high stiction immunity for rf mems capacitive switches and variable capacitors," *Sensors and Actuators A: Physical*, vol. 139, no. 1-2, pp. 233 – 236, 2007. Selected Papers From the Asia-Pacific Conference of Transducers and Micro-Nano Technology (APCOT 2006), Asia-Pacific Conference of Transducers and Micro-Nano technology. 51

[89] P. M. Varvak and A. F. Ryabov, *Reference book on the theory of elasticity*. Budivelnyk, Kiev, 1971. in russian. 58

[90] R. L. Courant, "Variational methods for the solution of problems of equilibrium and vibration," *Bulletin of the American Mathematical Society*, vol. 49, pp. 1–23, Jan. 1943. 75

[91] G. Pelosi, "Historical corner," *IEEE Antennas and Propagation Magazine*, vol. 51, pp. 202–202, Feb. 2009. 75

[92] *ANSYS Multiphysics Release 12.1 Documentation*. Ansys. 78

Appendices

Below there is an example of the ANSYS batch file used for one of simulations of the structure described in the thesis.

```
fini
/clear
/PREP7
/VIEW,1,1,1,1
/VUP,1,Z
/TITLE, TESTING SHAPE OF THE SWITCH WITH CONTACT



ET,     1,MESH200, 7
ET,     2,SOLID226,111
ET,     3,TARGE170
ET,     4,CONTA174

!* POLY
MP,DENS,1,2300
MP,KXX, 1,150           ! CONDUCTIVITY
MP,RSVX,1,400e-6        ! Electrical resistivity, Ohm-m
MP,EX,  1,175e+9        ! Young modulus, Pa
MP,PRXY,1,0.36          ! Poisson’s ratio
MP,ALPX,1,2.9e-6

!* SILI
MP,DENS,2,2330
MP,KXX, 2,153           ! CONDUCTIVITY
MP,RSVX,2,2.3e+3        ! Electrical resistivity, Ohm-m
MP,EX,  2,180e+9         ! Young modulus, Pa
MP,PRXY,2,0.28          ! Poisson’s ratio
```

```
MP,   C,2,700
MP,ALPX,2,2.6e-6

!* SiO2
MP,DENS,3,2650
MP,KXX, 3,1.4           ! CONDUCTIVITY
MP,RSVX,3,10e+10        ! Electrical resistivity, Ohm-m
MP,EX,  3,66e+9         ! Young modulus, Pa
MP,PRXY,3,0.17          ! Poisson’s ratio
MP,   C,3,705.5
MP,ALPX,3,0.55e-6

!* GOLD
MP,DENS,4,19300
MP,KXX, 4,315           ! CONDUCTIVITY
MP,RSVX,4,2.44e-8       ! Electrical resistivity, Ohm-m
MP,EX,  4,75e+9         ! Young modulus, Pa
MP,PRXY,4,0.42          ! Poisson’s ratio
MP,ALPX,4,14.2e-6
MP,   C,4,130.5

tol    = 1e-8
gapmin = 1e-7
Tblk   = 300
Vlt    = 200


!* MODEL
```

```
!*serpentine

rectng, 180e-06, 205e-06, 437.5e-06, 462.5e-06
rectng, 180e-06, 205e-06, 607.5e-06, 632.5e-06

rectng, 205e-06, 285e-06, 447.5e-06, 452.5e-06
rectng, 205e-06, 285e-06, 617.5e-06, 622.5e-06

rectng, 215e-06, 285e-06, 457.5e-06, 462.5e-06
agen,16,5,,,,10e-06

rectng, 280e-06, 285e-06, 452.5e-06, 457.5e-06
agen,9,21,,,,20e-06

rectng, 215e-06, 220e-06, 462.5e-06, 467.5e-06
agen,8,30,,,,20e-06

aglue,all

numcmp,all

arsym,x,all,,,,0,0
asel,u,loc,x,180e-06-tol,285e-06+tol
agen,2,all,,,1000e-06,,,,,1
allsel

numcmp,all

!* Contact area
```

```
rectng, 425e-06, 575e-06, 460e-06, 610e-06
rectng, 290e-06, 425e-06, 460e-06, 475e-06
rectng, 290e-06, 425e-06, 595e-06, 610e-06
rectng, 575e-06, 710e-06, 460e-06, 475e-06
rectng, 575e-06, 710e-06, 595e-06, 610e-06


!* The device boundary
rectng,      0,1000e-06,      0,1070e-06

boptn,keep,no
aovlap,all

numcmp,all

!*switch
rectng,      0,1000e-06,      0,1070e-06

rectng,215e-06, 285e-06,447.5e-06, 622.5e-06
rectng,715e-06, 785e-06,447.5e-06, 622.5e-06

!*squares
rectng,215e-06, 415e-06,215e-06, 415e-06
rectng,215e-06, 415e-06,655e-06, 855e-06
rectng,585e-06, 785e-06,215e-06, 415e-06
rectng,585e-06, 785e-06,655e-06, 855e-06

!* rf-lines
```

```
rectng,465e-06, 535e-06,215e-06, 385e-06
rectng,465e-06, 535e-06,685e-06, 855e-06

aovlap,all
numcmp,all

lsel,s,loc,y,437.5e-06-tol,632.5e-06+tol
lsel,u,loc,x,-tol,tol
lsel,u,loc,x,1000e-06-tol,1000e-06+tol
lsel,u,loc,x, 290e-06-tol, 710e-06+tol
lesize,all,5e-06
allsel

lsel,s,loc,x, 290e-06-tol, 710e-06+tol
lsel,r,loc,y, 460e-06-tol, 610e-06+tol
lesize,all,15e-06
allsel

lsel,s,loc,x,-tol,tol
lsel,a,loc,x,1000e-06-tol,1000e-06+tol
lsel,a,loc,y,-tol,tol
lsel,a,loc,y,1070e-06-tol,1070e-06+tol
lesize,all,50e-06
allsel

lsel,s,loc,y,215e-06-tol,215e-06+tol   !*golden squares element size
lsel,a,loc,y,415e-06-tol,415e-06+tol
lsel,a,loc,y,655e-06-tol,655e-06+tol
lsel,a,loc,y,855e-06-tol,855e-06+tol
```

```
lsel,a,loc,y,385e-06-tol,385e-06+tol   !*rf-lines element size
lsel,a,loc,y,685e-06-tol,685e-06+tol

lsel,a,loc,x,215e-06-tol,215e-06+tol   !*golden squares element size
lsel,a,loc,x,415e-06-tol,415e-06+tol
lsel,a,loc,x,585e-06-tol,585e-06+tol
lsel,a,loc,x,785e-06-tol,785e-06+tol

lsel,a,loc,x,465e-06-tol,465e-06+tol   !*rf-lines element size
lsel,a,loc,x,535e-06-tol,535e-06+tol

lesize,all,25e-06
allsel

type,1
mat,2
amesh,all

type,2
mat,2
esize,,3
vext,all,,,,,500e-06

asel,s,loc,z,500e-06-tol,500e-06+tol
esize,,1
mat,3
vext,all,,,,,1e-06
```

```
asel,s,loc,z,501e-06-tol,501e-06+tol
vext,all,,,,,0.63e-06

asel,s,loc,z,501.63e-06-tol,501.63e-06+tol
vext,all,,,,,0.3e-06

asel,s,loc,z,501.93e-06-tol,501.93e-06+tol
asel,r,loc,y,   215e-06-tol,   855e-06+tol
asel,u,loc,x,          -tol,   215e-06-tol
asel,u,loc,x,   785e-06+tol,  1000e-06-tol
asel,u,,,2192
asel,u,,,2037,2057,10
asel,u,,,2042,2052,10
mat,4
vext,all,,,,,3e-06



vsel,s,,,266,267,1
vsel,a,,,330,331,1
vsel,a,,,366,371,1
vsel,a,,,249,257,1
vsel,a,,,268,318,1
vsel,a,,,258,265,1
eslv,s
mat,1
emodif,all
allsel

nummrg,node,tol/2
```

```
block, 425e-06, 575e-06, 460e-06, 610e-06,
       501.93e-06+gapmin, 503.73e-06
*do,i,0,6,1
block, 435e-06+i*20e-06,445e-06+i*20e-06,470e-06,600e-06,
       501.93e-06+gapmin, 503.73e-06
*enddo

vsbv, 607, 608,,dele,dele
vsbv, 615, 609,,dele,dele
vsbv, 607, 610,,dele,dele
vsbv, 608, 611,,dele,dele
vsbv, 607, 612,,dele,dele
vsbv, 608, 613,,dele,dele
vsbv, 607, 614,,dele,dele

asel,s,loc,z,504.93e-06-tol,504.93e-06+tol
mat,4
vext,all,,,,,1.8e-06
allsel

numcmp,volu

k,2000,285e-06, 460e-06, 504.93e-06
k,2001,285e-06, 460e-06, 506.73e-06
k,2002,285e-06, 475e-06, 504.93e-06
k,2003,285e-06, 475e-06, 506.73e-06
k,2004,425e-06, 460e-06, 501.93e-06+gapmin
k,2005,425e-06, 460e-06, 503.73e-06
```

```
k,2006,425e-06, 475e-06, 501.93e-06+gapmin
k,2007,425e-06, 475e-06, 503.73e-06

v,2000,2001,2003,2002,2004,2005,2007,2006


k,2008,715e-06, 460e-06, 504.93e-06
k,2009,715e-06, 460e-06, 506.73e-06
k,2010,715e-06, 475e-06, 504.93e-06
k,2011,715e-06, 475e-06, 506.73e-06
k,2012,575e-06, 460e-06, 501.93e-06+gapmin
k,2013,575e-06, 460e-06, 503.73e-06
k,2014,575e-06, 475e-06, 501.93e-06+gapmin
k,2015,575e-06, 475e-06, 503.73e-06

v,2008,2009,2011,2010,2012,2013,2015,2014


k,2016,715e-06, 595e-06, 504.93e-06
k,2017,715e-06, 595e-06, 506.73e-06
k,2018,715e-06, 610e-06, 504.93e-06
k,2019,715e-06, 610e-06, 506.73e-06
k,2020,575e-06, 595e-06, 501.93e-06+gapmin
k,2021,575e-06, 595e-06, 503.73e-06
k,2022,575e-06, 610e-06, 501.93e-06+gapmin
k,2023,575e-06, 610e-06, 503.73e-06

v,2016,2017,2019,2018,2020,2021,2023,2022



k,2024,285e-06, 595e-06, 504.93e-06
```

```
k,2025,285e-06, 595e-06, 506.73e-06
k,2026,285e-06, 610e-06, 504.93e-06
k,2027,285e-06, 610e-06, 506.73e-06
k,2028,425e-06, 595e-06, 501.93e-06+gapmin
k,2029,425e-06, 595e-06, 503.73e-06
k,2030,425e-06, 610e-06, 501.93e-06+gapmin
k,2031,425e-06, 610e-06, 503.73e-06

v,2024,2025,2027,2026,2028,2029,2031,2030

vsel,s,,,718,721,1
vsel,a,,,608
vglue,all

allsel

numcmp,all

lsel,s,,,4356
lsel,a,,,4358,4360,1
lsel,a,,,4371
lsel,a,,,4372
lsel,a,,,4349
lsel,a,,,4351
lsel,a,,,4367
lsel,a,,,4368
lsel,a,,,4335
lsel,a,,,4337
lsel,a,,,4342
```

```
lsel,a,,,4344
lsel,a,,,4362
lsel,a,,,4364
lesize,all,15e-06
allsel

type,1
amesh,3124
amesh,3126
amesh,3128
amesh,3130

type,2
vsweep,717,3124,3131
vsweep,718,3126,3135
vsweep,719,3128,3139
vsweep,720,3130,3143

vsel,s,,,721
aslv,s
lsla,s
lesize,all,10e-06
type,1
amesh,3150
vsweep,721,3150,3149

allsel

nummrg,node,9*tol
```

```
nummrg,kp,9*tol

! *definition of contact elements

asel,s,,,3149
asel,a,,,3134
asel,a,,,3138
asel,a,,,3142
asel,a,,,3146
nsla,s,1
esln,s
type,4
r,1
esurf

asel,s,,,2037
asel,a,,,2042
asel,a,,,2047
asel,a,,,2052
asel,a,,,2057
nsla,s,1
esln,s
type,3
esurf

allsel

!* LOADING
```

```
asel,s,loc,z,0-tol,0+tol
da,all,UX,0
da,all,UY,0
da,all,UZ,0
allsel

/SOLU
tref,Tblk
ic,all,temp,300    ! Reference temperature
antype,trans
solc,on,on
nlgeom,on
outres,all,all
rescontrol,,none
trnopt,full        ! full transient dynamic analysis
time,1
deltim,0.1,0.2,0.1
!nsubst,10,30,15
!autots,on
esel,s,mat,,1
nsle,s,all
nsel,r,loc,x,180e-06-tol, 205e-06+tol
nsel,r,loc,y,437.5e-06-tol, 462.5e-06+tol
cp,1,VOLT,all
n_gr_1=ndnext(0)
d,n_gr_1,VOLT,0
esel,s,mat,,1
nsle,s,all
nsel,r,loc,x,180e-06-tol, 205e-06+tol
```

```
nsel,r,loc,y,607.5e-06-tol, 632.5e-06+tol
cp,2,VOLT,all
n_vlt_1=ndnext(0)
d,n_vlt_1,VOLT,Vlt

!esel,s,mat,,1
!nsle,s,all
!nsel,r,loc,x,795e-06-tol, 820e-06+tol
!nsel,r,loc,y,437.5e-06-tol, 462.5e-06+tol
!cp,3,VOLT,all
!n_gr_2=ndnext(0)
!d,n_gr_2,VOLT,0
!esel,s,mat,,1
!nsle,s,all
!nsel,r,loc,x,795e-06-tol, 820e-06+tol
!nsel,r,loc,y,607.5e-06-tol, 632.5e-06+tol
!cp,4,VOLT,all
!n_vlt_2=ndnext(0)
!d,n_vlt_2,VOLT,Vlt

nsel,all
kbc,1

allsel

/COM, === RADIOSITY BOUNDARY CONDITIONS
SF,ALL,RDSF,0.7,1 ! SURFACE-TO-SURFACE RADIATION LOAD
SPCTEMP,1,TBLK    ! AMBIENT TEMPERATURE
STEF,5.6704E-8    ! STEFAN-BOLTZMAN RADIATION CONSTANT,
```

```
                  ! J/(K)4(M)2(S)

MPTEMP,1,300,500,700,900,1100,1300
MPTEMP,7,1500

allsel

!* Face up

asel,s,,,3005,3020,5
sfa,all,,conv,-4,Tblk
mpdata,hf,4,1,11.87,40.38,44.14,46.07,47.27,48.20
mpdata,hf,4,7,48.96

asel,s,loc,z,506.73e-06-tol,506.73e-06+tol
asel,r,loc,y,447.5e-06-tol,622.5e-06+tol
asel,a,,,3025,3030,5
sfa,all,,conv,-6,Tblk
mpdata,hf,6,1,15.44,52.49,57.39,59.90,61.45,62.66
mpdata,hf,6,7,63.65

asel,s,,,3141
asel,a,,,3137
asel,a,,,3133
asel,a,,,3145
sfa,all,,conv,-9,Tblk
mpdata,hf,9,1,22.69,77.15,84.36,88.04,90.32,92.10
mpdata,hf,9,7,93.55
```

```
asel,s,,,3150
sfa,all,,conv,-12,Tblk
mpdata,hf,12,1,22.69,77.15,84.36,88.04,90.32,92.10
mpdata,hf,12,7,93.55

asel,s,,,2192
sfa,all,,conv,-13,Tblk
mpdata,hf,13,1,7.940,27,29.52,30.81,31.61,32.23
mpdata,hf,13,7,32.74

!* Face down
asel,s,loc,z,0+tol,0-tol
sfa,all,,conv,-2,Tblk
mpdata,hf,2,1,25.11,85.38,93.35,97.43,99.96,101.9
mpdata,hf,2,7,103.5

asel,s,,,3134
asel,a,,,3138
asel,a,,,3142
asel,a,,,3146
sfa,all,,conv,-10,Tblk
mpdata,hf,10,1,31.28,96.25,106,111.7,115.7,119
mpdata,hf,10,7,121.8

asel,s,,,3149
sfa,all,,conv,-11,Tblk
mpdata,hf,11,1,35.12,108,119,125.4,129.9,133.6
mpdata,hf,11,7,136.8
```

```
!* Side walls

asel,s,loc,x,         -tol,          tol
asel,a,loc,x, 1000e-06-tol, 1000e-06+tol
asel,a,loc,y,         -tol,          tol
asel,a,loc,y, 1070e-06-tol, 1070e-06+tol
sfa,all,,conv,-5,Tblk
mpdata,hf,5,1,45.17,75.20,85.99,95.30,103.8,112.1
mpdata,hf,5,7,120.4

asel,s,loc,y,460e-06-tol,475e-06+tol
asel,a,loc,y,595e-06-tol,610e-06+tol
asel,r,loc,x,285e-06-tol,285e-06+tol
asel,r,loc,z,504.93e-06-tol,506.73e-06+tol
cm,anchors1,area

asel,s,loc,y,460e-06-tol,475e-06+tol
asel,a,loc,y,595e-06-tol,610e-06+tol
asel,r,loc,x,715e-06-tol,715e-06+tol
asel,r,loc,z,504.93e-06-tol,506.73e-06+tol
cm,anchors2,area
allsel

asel,s,loc,x,465e-06-tol,465e-06+tol
asel,a,loc,x,535e-06-tol,535e-06+tol
asel,u,loc,y,415e-06+tol,655e-06-tol
asel,a,loc,x,215e-06-tol,215e-06+tol
asel,a,loc,x,285e-06-tol,285e-06+tol
asel,a,loc,x,415e-06-tol,415e-06+tol
```

```
asel,a,loc,x,585e-06-tol,585e-06+tol
asel,a,loc,x,715e-06-tol,715e-06+tol
asel,a,loc,x,785e-06-tol,785e-06+tol
asel,a,loc,y,215e-06-tol,215e-06+tol
asel,a,loc,y,385e-06-tol,385e-06+tol
asel,a,loc,y,415e-06-tol,415e-06+tol
asel,a,loc,y,447.5e-06-tol,447.5e-06+tol
asel,a,loc,y,622.5e-06-tol,622.5e-06+tol
asel,a,loc,y,655e-06-tol,655e-06+tol
asel,a,loc,y,685e-06-tol,685e-06+tol
asel,a,loc,y,855e-06-tol,855e-06+tol
asel,r,loc,z,501.93e-06-tol,506.73e-06+tol
cmsel,u,anchors1,area
cmsel,u,anchors2,area
sfa,all,,conv,-7,Tblk
mpdata,hf,7,1,3816,4787,5617,6444,7234,8036
mpdata,hf,7,7,8841
allsel

vsel,s,,,721
aslv,s
asel,r,loc,z,501.93e-06+gapmin+tol, 503.73e-06-tol
asel,u,,,3132
asel,u,,,3144
asel,u,,,3140
asel,u,,,3136
sfa,all,,conv,-8,Tblk
mpdata,hf,8,1,1.0136e+4,1.2629e+4,1.4832e+4,
              1.7029e+4,1.9132e+4,2.1267e+4
```

```
mpdata,hf,8,7,2.341e+4
allsel

vsel,s,,,717,720,1
eslv,s
sfe,all,1,conv,,-8
sfe,all,6,conv,,-8
sfe,all,1,conv,2,Tblk
sfe,all,6,conv,2,Tblk
mpdata,hf,8,1,1.0136e+4,1.2629e+4,1.4832e+4,
              1.7029e+4,1.9132e+4,2.1267e+4
mpdata,hf,8,7,2.341e+4
allsel

solve

/eof
```